AVALANCHES IN PLASTIC DEFORMATION: MAXIMUM VELOCITY STATISTICS, FINITE TEMPERATURE EFFECTS, AND ANALYSIS OF LOW TIME RESOLUTION DATA

BY

MICHAEL LEBLANC

DISSERTATION

Submitted in partial fulfillment of the requirements
for the degree of Doctor of Philosophy in Physics
in the Graduate College of the
University of Illinois at Urbana-Champaign, 2016

Urbana, Illinois

Doctoral Committee:

Professor Emeritus Richard L. Weaver, Chair
Professor Karin A. Dahmen, Director of Research
Professor Emeritus Michael B. Weissman
Professor S. Lance Cooper

Abstract

In both crystalline and amorphous solids, plastic deformation consists of intermittent jumps called avalanches, whose sizes are power-law-distributed over a scaling regime. In this thesis, we study the statistics of a simple mean-field avalanche model, with emphasis on both theoretical calculations and application to the analysis of experimental data on material deformation.

We establish a relationship between the simple mean-field model and a continuous time model called the ABBM model, originally proposed as a phenomenological model of Barkhausen noise in magnets. The relationship is formally valid for ductile materials without significant weakening, but the results of our calculations are expected to apply to the small avalanches even in materials with high weakening.

We then use the ABBM model to calculate several exact results concerning a system's maximum velocity during an avalanche. We find that the scaling of the maximum velocity distribution agrees with experiments on crystal plasticity. Left over from our calculations are several experimental predictions ready to be tested. The maximum velocity is a robust experimental observable and it has several distinct advantages over the more commonly-considered avalanche durations, so we expect our predictions to be useful in future tests of avalanche statistics in experimental systems.

Then, motivated by recent creep deformation experiments that find scale-invariant avalanches, we develop a scaling theory for thermally-activated avalanches in the simple avalanche model near the critical point and at low temperature. We highlight several generic predictions for how statistical observables scale with temperature.

Finally, we use the simple avalanche model to study how experimental avalanche measurements are influenced by the time resolution of the data. Using both experimental data and simulation data from the model, we determine how measured quantities change with resolution. From these relationships, we develop methods to diagnose when the time resolution low enough that it changes the measured avalanche statistics. We also propose a new analysis method that allows us to extract accurate size statistics from low-resolution data, and show that it is successful both on simulation data and downsampled high-resolution experimental data.

To my parents, Patty and Dennis LeBlanc, for their continual support.

Acknowledgments

First, I would like to thank my advisor Karin Dahmen, who was always generous with her time, full of great ideas, and supportive well beyond the call of duty for an advisor. This thesis would not have been possible without her. Her relentless enthusiasm has always been inspiring to me, and her emphasis on collaboration and communication, particular with experimenters, has served as a great counterbalance to my more insular tendencies.

I would also like to thank the other members of my committee, Richard Weaver, Mike Weissman, and Lance Cooper, for asking great questions and giving useful feedback on my prelim exam and also for agreeing to come back and listen to me again (for even longer this time!).

In my time here at UIUC, I've had the privilege of learning many things from many people, certainly too many to name. In particular, I'd like to thank Nigel Goldenfeld, who, along with Karin, advised me on my first paper. In addition, I was lucky to have the opportunity to take several excellent courses from him in my first couple of years here. I defy anyone to show me a more well-worn copy of his *Introduction to Phase Transitions and the Renormalization Group* than mine. I also owe a lot to Luiza Angheluta, who collaborated with me on that same first project. We worked well together and I wish we'd had the opportunity to write more papers.

I'd like to thank other members of the Dahmen group, for countless useful discussions as well as camaraderie. Coming into the group, I learned a lot from the more advanced grad students Georgios Tsekenis, Nir Friedman, Tyler Earnest, and Braden Brinkman. Over the last few years, the group has been lucky to have many excellent undergraduate researchers as members. I'd like to particularly thank Aya Nawano, who analyzed data that appears in the last chapter of this thesis. In addition, I've had the benefit of working with and learning from Li Shu, Xin Liu, Shivesh Pathak, Jordan Sickle, Jim Antonaglia, and Matt Wraith. I'd also like to thank the newer grad students Will McFaul and Mo Sheikh and wish them the best of luck going forward.

I should acknowledge Lance Cooper again, this time for all the support and advice he's given me in his capacity as the head of graduate programs. I agree with the broad consensus amongst the graduate

students that Lance is the best. The physics department at UIUC is also blessed with a great staff, and I'm particularly grateful to Wendy Wimmer, Mel Schweighart, Sal Belahi, Gianni Pezzarossi, Janice Benner, Becky McDuffee, Ted Robb, Dashawnique Long, Kate Shunk, and Darren Wright for lots of help over the years. Celia Elliot was a fount of excellent writing advice that I wish I'd had the discipline to follow more consistently.

I've had the benefit of collaborating with many great researchers. Again, there are too many to name, but I'd like to mention Wendy Wright, Robert Maass, and Peter Liaw, whose careful experiments have taught us a lot, as well as Yehuda Ben-Zion, Jonathan Uhl, and Lin Li.

The work presented in this thesis was partially supported by National Science Foundation through Grants No. DMS-1069224 and No. DMR- 1005209, NSF CBET 1336634, and DOE grant DE-FE0011194 with program manager Jessica Muellen.

Table of Contents

Chapter 1

Avalanches and crackling noise

1.1 Avalanches and crackling noise

An avalanche is a burst of activity caused by a chain reaction in a system with many coupled degrees of freedom. In certain systems, a small fluctuation has a chance of triggering additional activity, which can eventually build into a very large cascade. Many systems that exhibit avalanche behavior are near a non-equilibrium critical point [1]. A system in the critical state is highly susceptible to external perturbations, exhibits scale invariance over many orders of magnitude of distance, and has universal scaling properties independent of the details of the system's composition.

Avalanches are observed in a variety of dynamical systems, including magnetic materials [1, 2], charge density waves [3, 4], vortices in superconductors [5], fracture propagation [6], earthquakes [7, 8], crystal plasticity [9, 10, 11, 12, 8], amorphous plasticity [13, 14, 8, 9, 15, 16, 17, 18] . Although these processes involve systems with different microscopic details, on long length scales, the statistical scaling behavior of avalanches appears to have universal properties [7, 12, 4, 19, 20, 18].

1.2 Plastic deformation: theory and experiment

One extensively studied model that exhibits avalanche behavior is an elastic interface in a disordered medium. At zero temperature and for small values of external force, the interface is pinned by impurities and remains stationary, but as the stress is increased, the interface begins to slip forward in short, intermittent bursts (avalanches). When the stress Σ reaches a critical value Σ_c, the interface begins to move forward with a constant average velocity $v \sim (\Sigma - \Sigma_c)^\beta$. β is known as a *universal* exponent: its value depends only on the range of the interactions, the dimensionality of the system, symmetries, and broad characteristics of the disorder, but not on details like the stiffness of the material or the strength of the disorder. In addition to β, many quantities are known to be universal. The point in parameter space where $\Sigma = \Sigma_c$ is known as the depinning transition and is a non-equilibrium critical point. Systems that have the same values for universal quantities near the critical point, but are different in detail, are said to belong to the same *universality class*.

In the presence of long-ranged elasticity, it has been argued that the mean-field approximation (MFT) should give correct universal predictions for interfaces of spatial dimension greater than two [7, 2, 59]. Many real experimental systems should then be described correctly by mean-field theory in their universal properties. The MFT has the benefit that many quantities can be computed exactly.

We work with a simple mean-field avalanche model of material deformation that has a non-equilibrium critical point in the interface depinning universality class as well as a dynamical weakening parameter [20]. The model has a simple threshold dynamics and assumes mean-field interactions since they are expected to give correct universal predictions even near the critical point for slip planes in solid systems. The weakening parameter captures the fact that some materials become weaker as they slip. Weakening is particularly important for modeling amorphous material and earthquakes, as we will explain in greater detail below. In addition to tuning the system away from criticality, weakening can cause qualitative changes to the overall dynamics. The most notable effect is that if the weakening is significant, there are quasiperiodically recurring large events. In Chapter 2 we review the model in detail.

Recently there has been a lot of progress in determining the range of validity of the simple avalanche model, through theoretical arguments, simulations, and, most importantly, experiments. Likewise, there has been progress in using and extending avalanche models to address more specialized problems.

1.2.1 Crystal plasticity

A wide variety of crystalline systems have been shown to deform in power-law avalanches [9, 10, 21, 24, 25, 26] with a power law distribution $P(S) \sim S^{-\tau}$ and τ near or slightly above the mean field theory prediction $\tau = 3/2$. In [11], the tuned nature of the critical point was demonstrated via a stress-tuned data collapse of slip avalanche sizes in nanocrystals with exponents and scaling function that agreed with the mean field predictions. In [27], it was argued that creep-related stress relaxation during the quiet periods between avalanches in larger systems with hardening (such as microcrystals), at finite temperature, can cause the system to undergo oscillatory approaches to the critical point. This can explain quasi-periodicity of large avalanches, as well as faster-than-expected power law decay of avalanche sizes (essentially the same as the stress-integrated exponents that we discuss in Section C.3). Recently, the mean field model has been extended to explain dynamical pinning effects in high-entropy alloys, where the pinning occurs at much shorter timescales than the conventional Portevin-LeChatellier (PLC) effect [28]. As a result, PLC related slip avalanches are seen at temperatures as high as 300-600 degrees Celsius. Some two-dimensional dislocation dynamics simulations have given results that disagree strongly with mean field theory and the presence of a depinning-like critical point [29]. However, other simulations [23] have found good agreement with the simple model. In particular, three-dimensional dislocation dynamics simulations agree with the mean field theory [21]. Sorting out the differences between various simulation approaches is an ongoing project.

1.2.2 Amorphous plasticity

In amorphous systems the excitations that cause plastic deformation in amorphous materials are called shear transformation zones (STZs) [30, 31, 32] which are small configurations that rearrange plastically under stress. The STZs slipping along a shear band are coupled with long-ranged elastic forces, and thus we expect the simple mean-field avalanche model to apply to the deformation avalanches. Experiments on mm-size bulk metallic glasses (BMGs) have found remarkable agreement with the model across a range of quantities (about fifteen statistical measures), including exponents, scaling functions, and temporal avalanche shapes. [14]

Two-dimensional simulations of amorphous materials have shown power law exponents for the size distribution that are smaller than the MFT predictions [33] and also finite-size scaling behavior that differs significantly from MFT [34, 35]. It has been argued that an essential difference between the simple model and these simulations is that, in the simple model, stress transfer between different regions in the solid are always positive. However, in bulk elasticity, the stress transfer takes on positive and negative values, in a quadupolar pattern in the two-dimensional case [33]. One apparent consequence of this is that there is a pseudogap in the density of excitations as the stress increases [36] and this results in different behavior, even in a mean field description [37]. It has been argued that this leads to system-spanning events at all stresses, not just at the critical stress [38, 39]. However, arguments about the possibility of negative stress transfer do not take into account shear banding. Along a shear band, the stress transfer is positive. This explains the success of the simple model over more complicated approaches in BMG experiments [14].

The simple model can also be adapted to include a dynamic weakening effect. This weakening effect plays an important role, especially for BMGs. The result of dynamic weakening is that there are two regimes of slips: power-law-distributed small slips and periodically recurring large avalanches all of a characteristic size. Recently, the existence of two regimes with scaling relationships consistent with the mean field avalanche model was confirmed in BMG experiments [40].

Possible future practical applications include developing non-destructive tests of material properties, as well as hazard prediction based on avalanche statistics.

1.2.3 Earthquakes

It has long been known that the distribution of earthquake magnitudes follows a power law known as the Gutenberg-Richter distribution [41, 42]. An earthquake fault can be modeled as a two-dimensional slip plane, coupled to itself through the bulk by long-ranged elastic forces. Again, the mean field model avalanche should give correct predictions due to long-range elastic stress transfer through the bulk [7]. Indeed, measured values of the power law are consistent with MFT predictions [43]. However, the Gutenberg-Richter law holds for catalogs of earthquakes, summed over many faults with widely varying sizes and stresses. Some individual faults, notably the San-Andreas [44] instead display *characteristic* earthquake statistics, where large-magnitude events recur quasiperiodically in time. Characteristic statistics of this sort are predicted by the mean field model with dynamical weakening [43, 45]. More recent studies of earthquakes on individual fault zones have found scaling functions [8] and slip-avalanche shapes [46] consistent with the predictions of the mean-field avalanche model.

The simple model has also been used to inform and build more complicated models of earthquake phenomenology. For instance, a probabilistic model was developed to study a method of predicting large earthquakes by measure correlations of *small* earthquakes with tidal forces [47]. The same model was used for a study of avalanche wait time distributions [48].

1.3 Overview of contents

In this thesis, we will calculate avalanche probability distributions with attention to the extreme value properties, which have not been studied in detail until recently [49, 50]. We will derive exact predictions for universal scaling exponents and scaling functions for the statistics of the maximum interface velocity during an avalanche using the ABBM model, a domain wall model that is closely related to the mean field slip avalanche model at zero weakening..

The predicted probability distribution for the maximum velocity of an avalanche is described by a power law $P(v_m) \sim v_m^{-2}$. This basic result has been verified by acoustic emission and high-resolution extensometry experiments on crystal plasticity [51, 52, 9, 25, 26, 53]. We will argue that the maximum velocity is a robust and easily-measured quantity that is potentially useful in experimental tests of avalanche theories. In particular, we expect the maximum velocity will be useful in identifying candidate systems that may be described by mean field theory, but for which high-resolution time series are difficult to obtain experimentally.

Experiments have found power-law distributed event sizes and waiting times in metallic glasses undergoing creep motion [54]. We show that the simple plasticity theory can be adapted to give a scaling description of thermally activated motion near the critical point. We expect these predictions to be applicable to creep experiments on both crystalline and amorphous materials performed at relatively large loads.

Finally, as a complete change of pace, we consider data at low time resolution, an important problem in the analysis of experimental plasticity data. We compute the effects of low time resolution on avalanche size distributions and give quantitative criteria for diagnosing and circumventing problems associated with low time resolution. We show that traditional analysis of data obtained at low acquisition rates can lead to avalanche size distributions with incorrect power law exponents or no power law scaling at all. Furthermore, we demonstrate that it can lead to apparent data collapses with incorrect power law and cutoff exponents. We propose new methods to analyze low-resolution stress-time series that can recover the size distribution of the underlying avalanches even when the resolution is so low that naive analysis methods give incorrect results. We test these methods on both downsampled simulation data from a simple model and downsampled Bulk Metallic Glass (BMG) compression data and find that the methods recover the correct critical exponents.

In chapters 2 and 3, we review the mean field plasticity model and the closely related ABBM model respectively and show that they have equivalent predictions for avalanche statistics at slow driving, in ductile systems without significant weakening effects (such as crystals). In chapter 4 we outline the calculation techniques we developed for the ABBM model and demonstrate how to use them to derive velocity distributions for avalanches of given duration and size, as well as size and duration distributions. In chapter 5 we derive new exact results on the maximum velocity statistics for avalanches in the ABBM model. Then, in chapter 6 we develop a scaling theory for plastic deformation at finite temperature that makes predictions for creep experiments. Finally in chapter 7 we demonstrate some techniques we recently developed for analyzing low-resolution experimental data. We include three appendices (in addition to those containing supplementary material for Chapters 3, 4, and 5). The first gives some simulation results from the simple model with weakening on avalanche sizes and interevent times. The second consists of some brief calculations of avalanche distributions for the ABBM model at high rate. The third is a brief note on the effect of highly disordered pinning distributions on the model predictions.

Chapter 2

Simple avalanche model for plasticity

2.1 Model definition

We consider one-dimensional motion along a slip surface and let $u(x,t)$ be the local displacement discontinuity at a local patch at position x on the slip surface at time t. We can consider the general equation of motion [20]

$$\eta \frac{\partial u(x,t)}{\partial t} = \Sigma(x,t) + \sigma_{\text{int}}(x,t) - \sigma_p(x, u(x,t)). \tag{2.1}$$

We will explain each of the terms in Eq. (2.1): The fact that the left-hand side involves a first derivative in time amounts to the assumption of purely dissipative dynamics where force is proportional to velocity (i.e. strongly overdamped motion) and η is a dissipation coefficient. We will work in units so that $\eta = 1$. The term $\Sigma(x,t)$ is an external stress field applied to the system. We assume that patches of the slip plane are elastically coupled with one another and $\sigma_{\text{int}}(x,t)$ is the local stress due to these elastic interactions. Under linear elasticity, σ_{int} takes the form

$$\sigma_{\text{int}}(x,t) = \int d^d x' dt' J(x-x', t-t') \left[u(x',t') - u(x,t)\right] \tag{2.2}$$

where the spatial integral is over the d-dimensional slip plane and $J(x,t)$ is the stress transfer function, which we will assume to be positive. Finally, $\sigma_p(x, u(x,t))$ is a quenched random pinning stress due to disorder in the system. It is called a pinning stress because it causes patches of the slip plane become pinned locally until the local stress increases enough to cause them to slip. The random pinning stress can serve as a model for the pinning of dislocations by defects in crystalline solids [20, 24] or the frictional locking of fault-planes between tectonic plates [55, 56, 57, 43].

We can use a simple pinning model where the pinning stress at each patch x on the slip plane only becomes large at a discrete set of pinning sites $u_p^\alpha(x)$ for $\alpha \in \mathbb{Z}$. The sites are distributed independently for each point x, and the gaps in u between them $u^{\alpha+1}(x)_p - u_p^\alpha(x)$ are drawn independently from a distribution narrowly peaked about a characteristic value δu. The stress at a pinning point has a characteristic yield

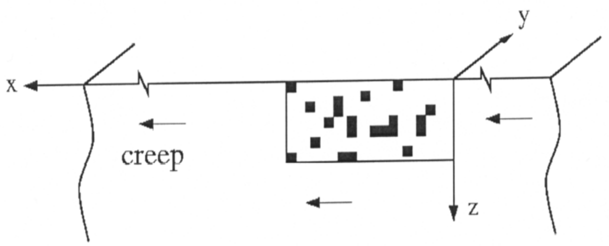

Figure 2.1: In the simple cellular model, a slip plane is modeled as an array of elastically coupled cells being driven at a constant velocity parallel to the plane.

strength τ_f.

If the external driving stress changes slowly and the pinning sites are sufficiently strong and close together, the dynamics of individual patches of the slip plane can be approximated as sticking at the pinning site until the local stress $\Sigma(x,t) + \sigma_{\text{int}}(x,t)$ exceeds τ_f and then slipping to the next pinning site [7]. When a patch slips forward, it pulls on neighboring patches and can cause them to slip as well. This chain reaction is called an *avalanche*.

It is useful for both analytic computations and simulations to consider a version of the model with a discrete set of N patches, henceforth known as cells. To model the long range elastic interactions along a shear band or earthquake fault, we will assume a mean-field interaction where each cell interacts equally with every other cell and a discrete time step δt over which the cells slip to their next pinning site. Thus, the stress transfer becomes $J(x,t) = \frac{J}{N}\delta(t - \delta t)$, where the delta function means that stress is redistributed on the subsequent time step. The local stress τ_i on cell i can be written

$$\tau_i = (J/N)\sum_{j=1}^{N}(u_j(t) - u_i(t)) + \Sigma_i(t). \tag{2.3}$$

2.1.1 Dynamical weakening

Inspired by earlier earthquake models [55, 56, 57], the mean field avalanche model includes dynamical weakening effects, captured by the addition of a single new parameter, a weakening coefficient ϵ [20]. Dynamical weakening is similar to the contrast between static and dynamic friction. While an avalanche is happening, cells that slip have their failure stress reduced to a dynamic value

$$\tau_d = \tau_f - \epsilon(\tau_f - \tau_a). \tag{2.4}$$

The addition of weakening can have a profound effect on the dynamics of the system. When the weakening is sufficiently large, the system has quasi-periodically recurring large events, whose size scale like $N^{3/2}$ where N is the number of cells in the system [45, 20]. In between these large events small events from the distribution $P(S) \sim S^{-\tau} \exp(-S/S_c)$ where S_c characterizes the size of the largest avalanches. S_c decreases with weakening like $S_c \sim \epsilon^{-2}$ for $\epsilon \ll 1$. Thus, for small (but non-negligible) weakening, the theory predicts quasi-periodic very large events with power law-distributed precursors.

In this thesis, we will generally assume that the material is ductile, so that the weakening is negligible, the exception being Appendix D, in which we will give some simulation results on the model with weakening. Even when the weakening is non-negligible, many of the analytical results are applicable to the small precursors in between large events (see, e.g. [14]).

2.2 Depinning transition

If the external stress is a constant $\Sigma(x,t) = \Sigma$ and it is small enough, the system will be stuck in a stable equilibrium, whereas at high stress the system will move continually. In between, there is a critical stress Σ_c at which the system first begins to move. As the critical stress is approached from below the system begins to slip intermittently in avalanches. At first the avalanches are small in size, but as the critical stress is approached, they can become unboundedly large. Thus the approach to the critical stress corresponds to a diverging length scale. The transition between a stationary system and a steadily moving system takes the form of a second-order phase transition, where the stress Σ is the tuning parameter and the average velocity v is the order parameter. This non-equilibrium phase transition is called a depinning transition.

On these general grounds, one expects that as the stress is increased above its critical value, the average velocity increases as

$$v \sim (\Sigma - \Sigma_c)^{\beta}. \tag{2.5}$$

where β is a universal critical exponent whose value depends only on broad features of the system such as symmetries, interaction ranges, and dimensionality. In mean field theory, for the threshold pinning dynamics we have assumed, it can be shown that $\beta = 1$ [58, 7]. Additionally, for long-ranged forces where the Fourier transform of the stress-transfer kernel follows

$$J(k) \sim |k| \tag{2.6}$$

for small k, the upper-critical dimension of the transition is $d_c = 2$ [7, 59] [1]. Above the upper critical dimension, mean field theory gives a quantitatively correct description of universal critical properties, such as scaling functions and critical exponents. For a two-dimensional slip surface with long ranged stress transfer ($J(r) \sim r^{-3}$), as in a slip-plane or slip-fault in solid system [7], the system is at its upper critical dimension, which means that MFT gives correct predictions up to small logarithmic corrections.

2.3 Dynamics at constant driving rate

Instead of a constant load, we can consider an external stress from a loading spring moving at a fixed driving rate v_d. In Eq. (2.3) becomes

$$\tau_i = (J/N)\sum_{j}^{N}(u_j - u_i) + K(v_d t - u_i), \tag{2.7}$$

where K is the stiffness of the loading spring.

The dynamics governed by a simple condition that a cell slips forward by an amount δu once its local stress goes above a certain failure threshold τ_f. For simplicity, we take both δu and τ_f to be the same for each cell and every slip event, though introducing a small amount of disorder in these quantities does not change the behavior. According to Eq. (2.7), when a given cell slips, its local stress decreases by an amount $(J + K)\delta u$ (assuming large N) while the local stress of each of the other cells increases by the amount $(J/N)\delta u$. We will call the small value of stress that the cell goes to after slipping the arrest stress τ_a. There is a relationship between the characteristic slip distance δu and the characteristic stress decrease $\tau_f - \tau_a$ in that

$$\delta u = (\tau_f - \tau_a)/(J + K). \tag{2.8}$$

The total amount of stress redistributed onto the rest of the system is

$$N(J/N)\delta u = \frac{J}{J + K}(\tau_f - \tau_a) \equiv c(\tau_f - \tau_a) \tag{2.9}$$

where we included a factor of N since all N cells see a stress increase of $(J/N)\delta u$. We defined a parameter $c \equiv \frac{J}{J+K}$. This is called the *stress conservation parameter* since it determines the fraction of stress that gets redistributed to the system. The remaining stress is lost as the loading spring relaxes during the avalanche.

Since when a cell slips, it increases the stress on every other cell, it can cause other cells to slip in turn. The chain reaction that ensues is called an avalanche and is characterized by a sequence $\{n_t\}$, where t is an

---

[1] As opposed to the situation where $J(k) \sim k^2$, indicative of short-ranged elastic forces with $\sigma_{\text{int}} \sim -\nabla^2 u.$, in which case the upper critical dimension $d_c = 4$ and mean field theory does not hold for systems in physical dimensions.

integer representing time and n_t is the number of cells that slip at time step t. An avalanche ends when no more cells slip, i.e. $n = 0$. Then, the loading spring will increase the stress until the next most unstable cell is triggered to slip.

The following simple algorithm illustrates the working of the model when the driving rate v_d is so small that its effect during avalanches is negligible:

1. If all of the cells are below the the failure stress, increase the stress until the most unstable cell is at the failure stress.
2. For each cell at or above the failure stress, lower its stress to the failure stress and increase the stress of every other cell by c/N.
3. Repeat step 2 until all cells are below their failure stress. Then the avalanche is over. Return to step 1.

Note that this is similar to the dynamics of a (mean-field) sandpile model.[60, 61]. The balance between slow driving and avalanche response is reminiscent of self-organized criticality (SOC) [62, 63]. However, our system clearly exhibits *tuned* criticality: it has a relevant tuning parameter c (as well as a driving rate and weakening parameter that also move the system away from criticality as they increase from zero). One of the common, sometimes argued prerequisite, features of SOC is a conservation law [64]. The system has conservation of stress as $c \to 1$, but it is broken for $c < 1$, and thus the parameter c tunes away from criticality. (See [65, 66] for more details on the relationship between interface depinning and sandpiles.)

There are several quantities that characterize an avalanche. If an avalanche starts at time step t_i and ends at time step $t_i + T$, T is called the avalanche duration. The avalanche size S has several commonly used, closely-related definitions. It may be defined as the total distance the system slips during the avalanche, or the total amount the stress on the driving spring drops. At very slow driving rates v_d, both of these quantities are proportional to the total number of cells that slip, so we can define

$$S = \sum_{t=t_i}^{t_i+T} n_t \tag{2.10}$$

with the understanding that the avalanche sizes measured in experiment will be approximately proportional to this and that more care may be needed when the driving rate is non-negligible (for instance, see Section 7.3).

2.3.1 Avalanche size statistics

Although the model is deterministic given a realization of the pinning sites, the exact profile $\{n_t\}$ of a particular avalanche is a complicated function of the initial stresses on each of the cells. As a result, it is more useful to characterize the avalanche stochastically.

Before an avalanche starts the cells will have local stresses τ_i between the failure stress τ_f and the arrest stress τ_a and they can be ordered by their relative stability, where the first cell is the most unstable (τ_1 is closest to τ_f), the second is second most unstable, and so on. When an avalanche is about to begin, the most unstable cell has $\tau_1 = \tau_f$.

An avalanche will stop once a cell that fails does not redistribute enough stress to cause the next most unstable cell to fail. If we let X_n be the amount of additional stress needed for the $n+1$-th most unstable cell to fail, i.e. $X_n \equiv \tau_f - \tau_{n+1}$ and we let Y_n be the total amount of stress redistributed by the failure of cells one through n, then the avalanche will end on the first cell n such that

$$Z_n \equiv Y_n - X_n < 0. \tag{2.11}$$

We will show, following [45] that Z_n can be statistically characterized as a random walk in n and that therefore the avalanche size is a first passage time to the original of a random walk.

We assume that the cell stresses are uniformly distributed between τ_a and τ_f. [2] Then, the gaps between the cell stresses $\Delta X_n = X_n - X_{n-1}$ will have mean value

$$\langle \Delta X_n \rangle \approx \frac{\tau_f - \tau_a}{N}. \tag{2.12}$$

Furthermore, the gaps will be approximately independent of one another as long as n is not very large compared to the total number of cells N and the X_n will resemble a Poisson process [67], The gap are thus exponentially distributed with mean $\frac{\tau_f - \tau_a}{N}$. Since the standard deviation of an exponential distribution is just its mean, the standard deviation of the gap will also be $\frac{\tau_f - \tau_a}{N}$.

If we let Y_n be the total amount of stress redistributed once cell n has failed, then we have

$$\Delta Y_n \equiv Y_n - Y_{n-1} \approx \frac{c}{N}(\tau_f - \tau_a) \tag{2.13}$$

with $c = \frac{J}{J+K.}$ The fluctuations in this quantity will be only due to the quenched randomness, and we will assume it to be negligible compared to the fluctuations in ΔX_n, although this assumption does not effect

---

[2] This is a reasonable assumption since if the cells start in a uniform configuration they will remain in one. Thus the system will converge to this stable steady state from any initial condition. Furthermore, it can be verified by simulation [45]

the universal properties of the solution.

Thus we have that $Z_n = Y_n - X_n$ is a random walk with mean increment

$$\langle \Delta Z_n \rangle = \langle \Delta Y_n \rangle - \langle \Delta X_n \rangle = \frac{(c-1)}{N}(\tau_f - \tau_a) \tag{2.14}$$

and standard deviation

$$\sigma \approx \frac{\tau_f - \tau_a}{N}. \tag{2.15}$$

For large avalanches, the size distribution will be the same as the first passage time to the origin for a random walk with drift toward the origin. For a random walk with mean step size $-\mu$ and variance σ^2, starting at position $x_0 > 0$, the distribution of first passage times to the origin is [68]

$$P(t) = \frac{x_0}{t} \frac{1}{\sqrt{2\pi\sigma^2 t}} e^{-\frac{(x_0 - \mu t)^2}{2\sigma^2 t}} \sim \frac{1}{t^{3/2}} e^{-\frac{\mu^2}{2\sigma^2} t} \tag{2.16}$$

for small x_0. Plugging in $\mu = \frac{1-c}{N}(\tau_f - \tau_a)$ and $\sigma = \frac{\tau_f - \tau_a}{N}$ gives

$$P(S) \sim \frac{1}{S^{3/2}} e^{-\frac{(1-c)^2}{2} S}. \tag{2.17}$$

Note that Eq. (2.17) takes the scaling form $P(S) \sim S^{-\tau}\mathcal{F}(S/S_c)$ where $\tau = 3/2$ is a mean field scaling exponent, $\mathcal{F}$ is a decaying scaling function (in this case an exponential decay) and S_c is a large size cutoff that determines the scale of the largest avalanche sizes. In this case we have

$$S_c \sim (1-c)^{-2}. \tag{2.18}$$

This scale diverges as $c \to 1$, which suggests that we may view $c = 1$ as a critical value. We will expand on this in the next section.

2.3.2 Statistical dynamics of an avalanche

The statistics of an avalanche's evolution in time follows is a simple Markov process [69, 7]. If, at time t during the course of an avalanche, n_t cells slip, the probability distribution $P(n_{t+\delta t})$ of the number of cells that will slip as a result at the next time step $t + \delta t$ is given by a Poisson distribution

$$P(n_{t+1}) = \frac{(cn_t)^{n_{t+1}}}{n_{t+1}!} e^{-cn_t} \tag{2.19}$$

where $c \equiv J/(J+K)$ and for simplicity we've assumed very slow driving compared to the timescale on which avalanches occur. The average of this distribution is $\langle n_{t+1} \rangle = cn_t$, so each cell triggers on average c others.

Therefore, the value of c determines whether or not avalanches are self-sustaining. For $c < 1$, they must eventually die down and for $c > 1$, they are able to grow without bound. The value $c = 1$ that separates these two behaviors is called the critical point. If c is tuned just below the critical point and the driving velocity v_d is slow, the interface exhibits jerky, steady-state motion under an average pulling stress $\langle \Sigma \rangle = c\Sigma_c$ [2]. As c approaches 1, the system approaches a steady state in which the stress stays near its critical value.

Eq. (2.17) shows that near criticality, the distribution of avalanche sizes has a scaling form with a characteristic size $S_c \sim (1-c)^{-2}$ that diverges as the transition is approached. In particular,

$$P(S) = S^{-3/2} \mathcal{F}\left(-Sk^2\right) \tag{2.20}$$

where $k \equiv 1 - c$ and $\mathcal{F}(x) \propto e^{-x/2}$ [7]. The renormalization group picture for the depinning transition [58] suggests that this scaling form should be universal. In other words, the exponents and scaling function $\mathcal{F}$ should only depend on the dimensionality of the system, symmetries and range of interactions. A full analysis reveals that mean-field theory makes correct predictions for the exponents and scaling function in dimensions less than or equal to 3 if the system has sufficiently long-ranged elastic forces [2, 7]. Therefore, despite its simplicity and unphysical interactions, the mean-field model should do just as well as a more realistic model at predicting universal quantities near the depinning transition.

Now, we will show that in the cellular plasticity model, the number of cells n_t that fail at time step t follows a discrete time Markov process with transition probability

$$P(n_{t+\delta t}|n_t) = \frac{\rho(n_t)^{n_{t+\delta t}}}{n_{t+\delta t}!} e^{-\rho(n_t)} \tag{2.21}$$

where $\rho(n_t) = \langle n_{t+\delta t} \rangle$ and we have

$$\langle n_{t+\delta t} \rangle = \frac{Jn_t + Kn_d}{J+K} \tag{2.22}$$

where $n_d \equiv v_d/\delta u$. This rule can be derived from the following picture, (see e.g. Refs. [7, 46]): We first divide the interface into N cells of equal volume that are coupled to one another with a mean-field coupling (infinite range) and also each coupled to a driving spring that pulls the interface at an average velocity v_d. This means that the total local stress on the i'th cell is given by

$$\tau_i = (J/N) \sum_{j \neq i}^{N} (u_j - u_i) + K(v_d t - u_i) \tag{2.23}$$

where J is the elastic coupling between the cells, K is the coupling to the driving point and the u_i are the positions of the cells along the direction of motion.

To capture the dynamics due to the pinning forces, a cell slips forward by an amount δu_i as soon as its local stress is above a threshold $\tau_{s,i}$. This raises the stress on every other cell by an amount $\delta\tau_j = (J/N)\delta u_i$ and decreases cell i's stress by an amount $|\delta\tau_i| = (J+K)\delta u_i$. Assuming that the stress drops, $\delta\tau_i$, and failure stresses, $\tau_{s,i}$, are distributed very narrowly around the values $\delta\tau$ and τ_s, respectively, each cell's stress will be approximately confined to the interval $[\tau_s - \delta\tau, \tau_s]$. Then, each cell that did not slip at a given time step will experience a stress increase of

$$\Delta\tau_t = n_t \frac{J\delta\tau}{N(J+K)} + K v_d \delta t \tag{2.24}$$

where n_t is the number of cells that slipped at time t and δt is the duration of a time step. If we further assume that the stresses of the cells that did not slip at time t are uniformly distributed within $[\tau_{s,i} - \delta\tau, \tau_{s,i}]$, the cells that fall at time $t + \delta t$ will be the ones with stresses greater than $\tau_{s,i} - \Delta\tau_t$. This means that each cell has a $\Delta\tau_t/\delta\tau$ chance of slipping at the next time step $t + \delta t$ and that the average number of cells that slip is

$$\langle n_{t+\delta t}\rangle = N\frac{\Delta\tau_t}{\delta\tau} = \frac{n_t J}{(J+K)} + \frac{NKv_d\delta t}{\delta\tau}. \tag{2.25}$$

Writing the average number of cells that slip per time step in terms of the pulling velocity as $n_d = v_d N\delta t/\delta u$ and rearranging gives

$$\rho(n_t) = \langle n_{t+\delta t}\rangle = \frac{Jn_t + Kn_d}{J+K} \tag{2.26}$$

which has $\langle n_{t+\delta t}\rangle = \langle n_t\rangle = n_d$ as a steady state average. Since we expect an average of $\rho(n_t)$ cells to slip in the next time period, $n_{t+\delta t}$ is Poisson distributed as in Eq. (2.21).

As also pointed out in Ref. [70], an update rule like Eq.(2.21) derived in the shell model of the random field Ising model [69] is equivalent to the ABBM model in the continuum limit. This follows from the Gaussian approximation to the Poisson update rule, which is valid for large $\rho(n_t)$ and is given by

$$n_{t+\delta t} = \rho(n_t) + \sqrt{\rho(n_t)}\eta_t, \tag{2.27}$$

where η_t is a univariate Gaussian random variable with zero mean. Assuming that K/J is small and that terms multiplied by it can be neglected in the fluctuation term when $\rho(n_t)$ is large, we have

$$n_{t+\delta t} - n_t \approx -\frac{K}{J}(n_t - n_d) + \sqrt{n_t}\eta_t. \tag{2.28}$$

In the next chapter, we will consider the ABBM model, which obeys an equation of motion similar to Eq. (2.28).

Chapter 3

ABBM model

3.1 Model definition

The ABBM model [71] was proposed by Alessandro et al. in 1990 as a phenomenological model for Barkhausen noise in magnets. However, it serves more generally as a mean-field theory for interface motion in the presence of pinning disorder and long-ranged forces [2, 72, 19, 70]. A wide variety of systems can be described on a mesoscopic level as interfaces moving through disordered media, including domain walls in magnets, fluid contact lines, vortex lines in superconductors, and strike-slip faults [7, 59].

A d-dimensional interface (or domain wall) propagating in a $d+1$-dimensional medium can be described by a function $u(x,t)$ that gives its position along the propagation direction. We make the assumption that the interface is sufficiently flat that regions with "overhangs" (such that $u(x,t)$ would become multivalued in x) can be ruled out. In the ABBM model, the interface is reduced to a single degree of freedom, the center-of-mass position

$$u(t) = \frac{1}{L^d} \int u(x,t) d^d x, \tag{3.1}$$

which obeys the equation of motion

$$\eta \frac{du}{dt} = k\left(v_d t - u\right) + F(u), \tag{3.2}$$

where v_d is the constant driving rate, k is an elastic coupling to the driving force, and $F(u)$ is a random effective pinning force. The first derivative on the left-hand side of Eq. 3.2 constitutes an assumption of over-damped motion. We will always work in units where the damping constant $\eta = 1$ and will drop it from equations from here on. We also define a new constant $c \equiv k v_d$. Thus Eq. 3.2 can be written as

$$\frac{du}{dt} = ct - ku + F(u). \tag{3.3}$$

The pinning force $F(u)$ is assumed to be a Brownian motion in u, i.e. it is Gaussian, has mean $\langle F(u)\rangle = 0$

and has correlations

$$\langle F(u)F(u')\rangle = 2D\min(u,u') \tag{3.4}$$

where D is a constant that characterizes the strength of the pinning disorder.

In contrast to the short-ranged (delta function) correlations typically seen in Langevin equations, $F(u)$ is correlated over a large distance. However, is important to note that this long-ranged correlation of the effective pinning force does not constitute the assumption of long-ranged correlations for the physical disorder[1]. Under certain assumptions, the Middleton no-passing theorem [73] guarantees that the interface motion obeys $v(t) > 0$ at all times. This means that $u(t)$ is monotonically increasing and we can choose to study the system's evolution in either u or t.

An equation of motion for v can be obtained by differentiating Eq. (3.2) with respect to u. This gives,

$$\frac{d\tilde{v}}{du} = -k + \frac{c}{\tilde{v}} + w(u), \tag{3.5}$$

where $\tilde{v}(u) \equiv v(t(u))$ and $w(u) = dF/du$. Since the derivative of Brownian motion is white noise, the correlations in $w(u)$ are given by

$$\langle w(u)w(u')\rangle = 2D\delta(u-u'). \tag{3.6}$$

Eq. (3.5) can be interpreted as the motion $\tilde{v}(u)$ of a Brownian particle in a logarithmic potential $\tilde{U}(u) = ku - c\log(u)$.

To get a time evolution equation, we multiply both sides of Eq. (3.5) by $v = du/dt$. This gives

$$\frac{dv}{dt} = -kv + c + vw(u). \tag{3.7}$$

We can make the noise an explicit function of t by observing that the correlator must obey

$$\langle w(u(t))w(u(t'))\rangle = 2D\delta(u(t)-u(t')) = 2D\frac{du}{dt}\delta(t-t'). \tag{3.8}$$

Thus it makes sense to define a noise $\eta(t) = w(u(t))/\sqrt{v(t)}$, giving

$$\frac{dv}{dt} = -kv + c + \sqrt{v}\eta(t), \tag{3.9}$$

---

[1] To see this, consider the pinning field $F(x,u)$ in the medium. In interface models, one typically assumes a short-ranged correlator $\langle F(x,u)F(x',u')\rangle \sim \delta(x-x')\Delta(u-u')$, where $\Delta(u)$ is sharply peaked at the origin [58]. However, the *effective* correlations in the total pinning force $F(u) = \int F(x,u(x))d^dx$ are actually long-ranged [2]. This is because different pieces of the interface move forward at different times. An incremental change in the center of mass position u comes from a small piece jumping forward and this will only cause an incremental random change to the total pinning force. Thus a Brownian motion in u is a physically sensible model for the effective disorder.

where the noise $\eta(t)$ is Gaussian, has zero mean, obeys

$$\langle \eta(t)\eta(t')\rangle = 2D\delta(t-t'), \tag{3.10}$$

and is interpreted in the Itô sense (see the appendix, section A.1). The interpretation can be verified by demanding that Eq. (3.9) predict the correct steady state distribution [71]

$$P(v, t \to \infty) \propto v^{-1+c/D} \exp(-kv/D), \tag{3.11}$$

which can also be derived from Eq. (3.5) [2]. It has been shown rigorously that the ABBM model gives the statistics of the mean field theory of interface depinning in the quasistatic limit [74].

Eq. (3.9) will be the most useful for understanding the avalanche statistics. Incidentally, we notice that Eq. (3.9) is identical to the equation satisfied by interest rates in the Cox-Ingersoll-Ross bond pricing model [75]. A similar $\sqrt{v}$-multiplicative noise process also appears in reaction-diffusion systems driven by internal noise [76]. The dynamics of this process is characterized by power-law statistics of avalanche sizes and durations, and long-range temporal correlations with power spectrum $S(f) \sim f^{-a}$, where f is the frequency and $a > 1$.

3.2 Avalanches in the ABBM model

The stochastic process defined by Eq. (3.9) is well-studied [77, 75, 78] The fact that $v'(t) \to c$ as $v \to 0$ guarantees that v never becomes negative, although, remarkably, v can become zero instantaneously, provided that $c/D < 1/2$[2].

Avalanches are periods of continuous forward motion. Thus, in the ABBM model we can define an avalanche of duration T to be an *excursion* in the velocity v(t), which is a path that starts and ends with $v(t_0) = v(t_0 + T) = 0$ with $v(t) > 0$ for $t_0 < t < t_0 + T$. The size of an avalanche is defined to be the total amount of motion during the avalanche:

$$S = \Delta u = \int_{t_0}^{t_0+T} v(t)dt. \tag{3.12}$$

Alternatively, since the velocity can also be viewed as a function of position $\tilde{v}(u)$, it can be more useful to characterize avalanche sizes with Eq. (3.5). In this parametrization, an avalanche of size S corresponds to an

---

[2] This contrasts with the more familiar process of geometric Brownian motion $\frac{dx}{dt} = \mu x + x\eta(t)$ which is strictly positive for any $\mu \in \mathbb{R}$.

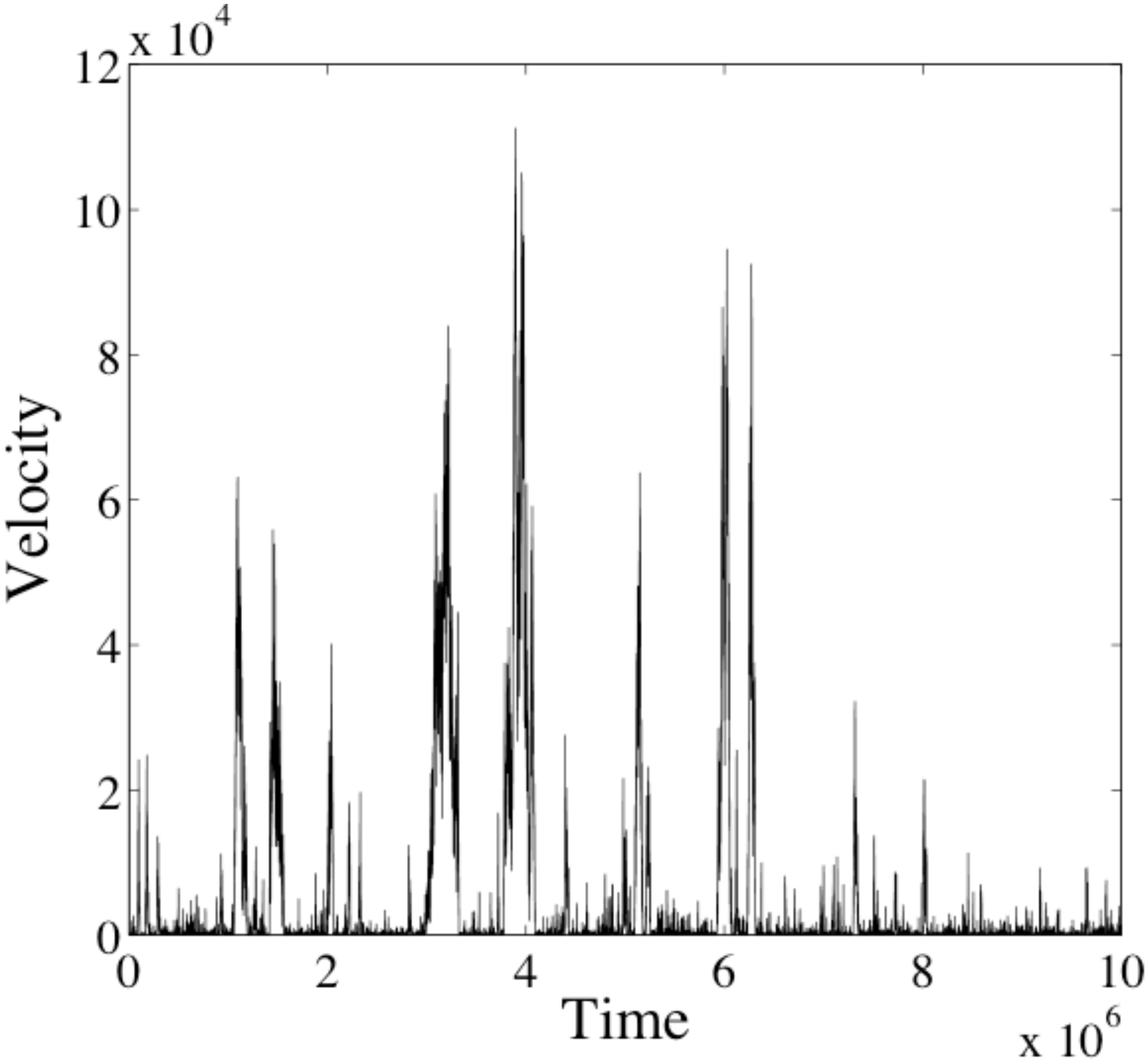

Figure 3.1: A numerical integration of the ABBM model (Eq. (3.9)) for $k = .001$ and $v_d = 1$.

excursion of $\tilde{v}(u)$: a path that starts and ends with $\tilde{v}(u_0) = \tilde{v}(u_0+S) = 0$ with $\tilde{v}(u) > 0$ for $u_0 < u < u_0+S$.

3.3 Equivalence of the ABBM model and the cellular model

We have showed (see Eq. (2.21)) that in the cellular plasticity model, the number of cells n_j that fail at time $t = j\delta t$ follows a discrete time Markov process where

$$P(n_{j+1}|n_j) = \frac{\rho(n_j)^{n_{j+1}}}{n_{j+1}!} e^{-\rho(n_j)} \tag{3.13}$$

As also pointed out in Ref. [70], an update rule like Eq.(2.21) derived in the shell model of the random field Ising model [69] is equivalent to the ABBM model in the continuum limit. This follows from the Gaussian approximation to the Poisson update rule, which is valid for large $\rho(n_t)$ and is given by

$$n_{t+\delta t} = \rho(n_t) + \sqrt{\rho(n_t)}\eta_t, \tag{3.14}$$

where η_t is a univariate Gaussian random variable with zero mean. Assuming that K/J is small and that terms multiplied by it can be neglected in the fluctuation term when $\rho(n_t)$ is large, we have

$$n_{t+\delta t} - n_t \approx -\frac{K}{J}(n_t - n_a) + \sqrt{n_t}\eta_t. \tag{3.15}$$

The number of cells that slip during a time step is related to the instantaneous center of mass velocity by $v_t = n_t \delta u/(N\delta t)$, so, multiplying through by the conversion factor and taking the continuum limit in time $\delta t \to 0$, we arrive at the ABBM equation

$$\dot{v}(t) = k\left(\frac{c}{k} - v(t)\right) + \sqrt{2Dv(t)}\eta(t). \tag{3.16}$$

where $k \equiv \frac{K}{J\delta t}$, $c \equiv kv_a$, $\eta(t) = \eta_t/\sqrt{\delta t}$, and $2D \equiv \frac{\delta u}{N\delta t^2}$. The form of the discrete time equation shows that the Itô interpretation is correct (see the appendix, Section A.1) . Therefore, this model is equivalent to the ABBM model at large velocities. Notice also that for $K = 0$, the continuum limit of the discrete model's steady state equation

$$P(n) = \sum_{n'} P(n|n')P(n') \approx \int dn' \frac{(n')^n e^{-n'}}{n!} P(n') \tag{3.17}$$

is satisfied by the ansatz $P(n) = n^{-1}$, which agrees with the $c, k \to 0$ limit of Eq. (3.11).

Chapter 4

Avalanche statistics in the ABBM model

4.1 Stationary distribution

With the change of variable $x = 2\sqrt{v}$ and Ito's lemma (see Section A.1), Eq. (3.9) can be transformed into an additive noise equation

$$\frac{dx}{dt} = -\frac{k}{2}x + \frac{2c - D}{x} + \xi(t). \tag{4.1}$$

The problem is thus mapped to an over-damped Brownian motion of a particle confined to the right half plane in a potential $V(x) = \frac{1}{4}kx^2 - (2c - D)\log(x)$. Near criticality, $k \to 0$ and the problem reduces to Brownian motion in a logarithmic trap. Einstein taught us that the noise $\xi(t)$ is equivalent to the particle being in a heat bath of temperature $kT = D$, so the steady state distribution for x should be proportional to a Boltzmann factor

$$P(x, t \to \infty) \propto e^{-V(x)/D} = x^{2c/D-1} e^{-\frac{1}{4D}kx^2}. \tag{4.2}$$

Changing variables back to $v = x^2/4$ and normalizing, we get

$$P(v, t \to \infty) = \left|\frac{dx}{dv}\right| P(x = 2\sqrt{v}, t \to \infty) = \frac{(k/D)^{c/D}}{\Gamma(c/D)} v^{c/D-1} e^{-kv/D} \tag{4.3}$$

where $\Gamma(x)$ is the Gamma function.

4.2 Path integral formalism

For an initial condition $x(0) = 0$, the particle may execute an excursion with $x(t) > 0$ for a duration T until its position returns to the origin for the first time. This excursion corresponds to an avalanche in the $v(t)$ during the interface propagation. In the following, we calculate the distribution of the instantaneous displacement during an excursion of size T, namely $P(x, t|T)$, and, by a corresponding transformation of variables, the conditional distribution of velocities in avalanches of fixed durations, $P(v, t|T)$. This allows us to determine the avalanche shape.

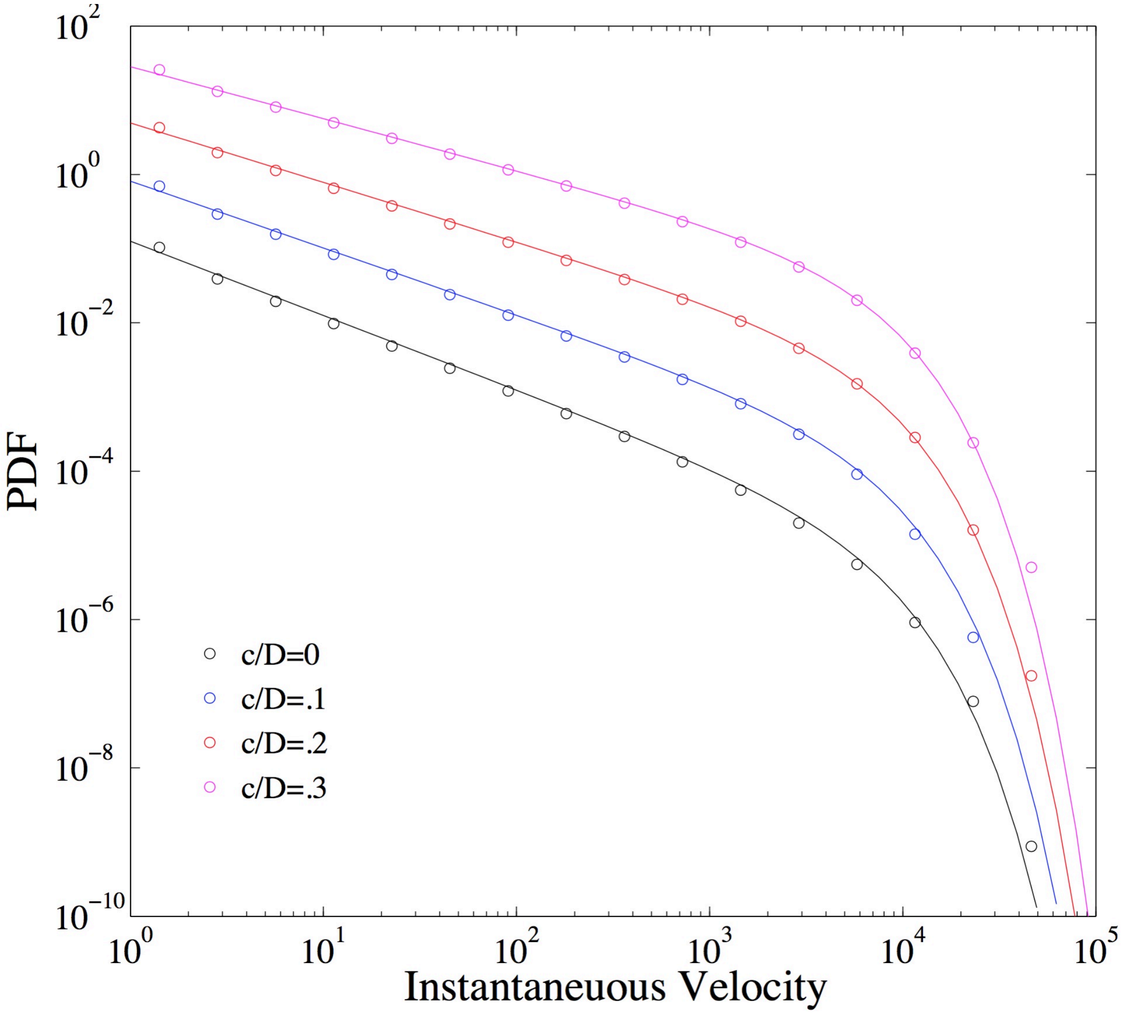

Figure 4.1: The instantaneous velocity PDF $P(v)$ for several values of $\tilde{c}$. The solid lines represent the functional form predicted by Eq. (4.3). For visibility, the PDFs are multiplied by different constants to offset from one another.

The probability distribution for the process defined by Eq. (4.1) can be written as a path integral

$$P(x,t) \quad \propto \quad \int \mathcal{D}y(\tau)\delta(x-y(t))\left\langle \delta\left(\frac{dy}{dt}+\frac{dV(y(t)}{dy}-\xi(t)\right)\right\rangle_{\xi} \tag{4.4}$$

where $V(x)$ is as above and the noise average is performed with respect to the Gaussian distribution $P_{\xi} \propto \exp\left(-\frac{1}{4D}\int \xi(t)^2 dt\right)$ that produces, e.g. Eq. (3.10). Following Ref. [82], we demand that the path is an excursion of duration T by fixing the endpoints $x(0)=x(T)=\epsilon$, where ϵ is some small value, later taken to zero. Also, by applying the positivity constraint that $x(t)>0$ for $0<t<T$, we have that

$$P(x,t|T) \quad = \quad \lim_{\epsilon\to 0}\frac{1}{Z_{\epsilon}(T)}\int_{y(0)=\epsilon}^{y(T)=\epsilon}\mathcal{D}y(\tau)e^{-\int_0^T d\tau L_E(y,\dot{y})}\delta(y(t)-x)\prod_{0\le\tau\le T}\Theta(y(\tau)). \tag{4.5}$$

The noise average has been performed, resulting in the Lagrangian

$$L_E\left(x, \frac{dx}{dt}\right) = \frac{1}{4D}\left(\frac{dx}{dt} + \frac{dV(x)}{dx}\right)^2 \tag{4.6}$$

and the product of theta functions enforces the positivity constraint. The normalization factor integrates over all excursions regardless if they go through x at time t and is therefore given by

$$Z_\epsilon(T) \quad = \quad \int_{x(0)=\epsilon}^{x(T)=\epsilon} \mathcal{D}x(\tau) e^{-\int_0^T d\tau L_E(x,\dot{x})} \prod_{0\leq\tau\leq T} \Theta(x(\tau)). \tag{4.7}$$

The equivalent real-time Lagrangian, obtained by transforming the imaginary time coordinate t to $\tau = -it$ and factoring out a -1 is

$$L(x, \dot{x}) = -\frac{1}{4D}\left(-i\dot{x} + V'(x)\right)^2, \tag{4.8}$$

where $\dot{x} = \frac{dx}{d\tau}$ and $V'(x) = \frac{dV}{dx}$. The canonical momentum corresponding to $L(x, \dot{x})$ is then $p = \frac{\partial L}{\partial \dot{x}} = \frac{i}{2D}(-i\dot{x} + V'(x))$, and the real time Hamiltonian

$$\hat{H} = p\dot{x} - L = Dp^2 - ipV'(x). \tag{4.9}$$

Therefore, the evolution of the Brownian particle in a potential $V(x)$ can be determined from its quantum analog that satisfies $i\partial_\tau \psi = \hat{H}\psi$. Replacing $p = -i\partial_x$ and $\tau = -it$, the probability $P(x,t)$ that the Brownian particle is at position x at time t satisfies the Fokker-Planck equation

$$\frac{\partial P}{\partial t} = \frac{\partial}{\partial x}\left(V'(x)P\right) + D\frac{\partial^2 P}{\partial x^2}, \tag{4.10}$$

which must be solved with an absorbing boundary condition at the origin $P(0,t) = 0$ in order to enforce the positivity constraint. For $k = 0$, Eq. (4.10) reduces to

$$\frac{\partial P}{\partial t} = \frac{\partial}{\partial x}\left(\frac{D - 2c}{x}P\right) + D\frac{\partial^2 P}{\partial x^2}, \tag{4.11}$$

which can be solved exactly.

4.3 Velocity statistics for avalanches of fixed duration

By a generic separation of variables $P(x,t) = e^{-Et} f(x)$, Eq. (4.11) is reduced to the eigenvalue problem

$$\frac{d^2 f}{dx^2} + \frac{1-2\tilde{c}}{x}\frac{df}{dx} + \left(\frac{E}{D} - \frac{1-2\tilde{c}}{x^2}\right) f = 0, \tag{4.12}$$

where $\tilde{c} = c/D$. This is a modified version of the Bessel equation and the particular solution that is well-behaved at the origin is

$$f(x) = x^{\tilde{c}} J_{1-\tilde{c}}\left(\sqrt{\frac{E}{D}}x\right) \tag{4.13}$$

where $J_{1-\tilde{c}}(x)$ is the Bessel function of the first kind [83]. We have assumed $0 \leq \tilde{c} < 1$ since this is the range in which the model exhibits avalanche behavior (otherwise the origin is inaccessible in the steady state, as can be seen in Eq. (3.11)). We can now proceed to calculate the $P(x,t)$. For this, we interpret the above path integrals as a matrix element between two functions defined on $[0,\infty)$ given by

$$\langle h | e^{-\hat{H}_1(t-t_0)} | g \rangle_w = \int_0^\infty h(x) e^{-\hat{H}_1(t-t_0)} g(x) dx. \tag{4.14}$$

where the Hamiltonian is

$$\hat{H}_1 = -D\partial_x^2 - \partial_x V'(x), \tag{4.15}$$

with the potential $V(x) = -(2c-D)\log(x)$ and an absorbing boundary condition at $x=0$. We write the eigenfunctions $f_k(x) = x^{\tilde{c}} J_{1-\tilde{c}}(kx)$ with the eigenvalues defined as $E_k = Dk^2$. Using the inverse Hankel transform of $g(x)x^{-\tilde{c}} = \int_0^\infty kdk J_{1-\tilde{c}}(kx)\tilde{g}_{1-\tilde{c}}(k)$, the above expression becomes equivalent to

$$\langle h | e^{-\hat{H}_1(t-t_0)} | g \rangle_w = \int_0^\infty dx h(x) \int_0^\infty kdk e^{-Dk^2(t-t_0)} x^{\tilde{c}} J_{1-\tilde{c}}(kx) \tilde{g}_{1-\tilde{c}}(k), \tag{4.16}$$

where

$$\tilde{g}_{1-\tilde{c}}(k) = \int_0^\infty J_{1-\tilde{c}}(kx) g(x) x^{1-\tilde{c}} dx. \tag{4.17}$$

Hence, the probability of being at position x and time t during an excursion of duration T, $P(x,t|T)$, can be defined using the matrix elements as

$$P(x,t|T) = \lim_{\epsilon\to 0} \frac{\langle \epsilon | e^{-\hat{H}_1(T-t)} | x \rangle_w \langle x | e^{-\hat{H}_1 t} | \epsilon \rangle_w}{\langle \epsilon | e^{-\hat{H}_1 T} | \epsilon \rangle_w}, \tag{4.18}$$

where $\langle\epsilon|e^{-\hat{H}_1 T}|\epsilon\rangle_w = Z_\epsilon(T)$. Thus, from Eq. (4.16) with $h(x) = \delta(x - z)$ and $g(x) = \delta(x - \epsilon)$, we have

$$\begin{aligned}\langle z|e^{-\hat{H}_1 t}|\epsilon\rangle_w &= \int_0^\infty dx\delta(x-z)\int_0^\infty kdkx^{\tilde{c}}J_{1-\tilde{c}}(kx)e^{-Dk^2t}\int_0^\infty y^{1-\tilde{c}}dyJ_{1-\tilde{c}}(ky)\delta(y-\epsilon) \\ &= \epsilon^{1-\tilde{c}}z^{\tilde{c}}\int_0^\infty kdke^{-Dk^2t}J_{1-\tilde{c}}(k\epsilon)J_{1-\tilde{c}}(kz),\end{aligned} \tag{4.19}$$

and, in the limit of $\epsilon \ll 1$, the above expression can be expanded to leading order

$$\begin{aligned}\langle z|e^{-\hat{H}_1 t}|\epsilon\rangle_w &\approx \frac{\epsilon^{2(1-\tilde{c})}z^{\tilde{c}}}{2^{1-\tilde{c}}\Gamma(2-\tilde{c})}\int_0^\infty e^{-Dk^2t}J_{1-\tilde{c}}(kz)k^{2-\tilde{c}}dk \\ &\approx \left(\frac{\epsilon}{2}\right)^{2(1-\tilde{c})}\frac{z(Dt)^{-2+\tilde{c}}}{2\Gamma(2-\tilde{c})}e^{-\frac{z^2}{4Dt}}\end{aligned} \tag{4.20}$$

where $\Gamma(z)$ is the gamma function.

In a similar way, we obtain the other transition amplitude, to the leading order in ϵ, as

$$\begin{aligned}&\langle\epsilon|e^{-\hat{H}_1(T-t)}|z\rangle_w \\ \approx\ &\frac{\epsilon z^{1-\tilde{c}}}{2^{1-\tilde{c}}\Gamma(2-\tilde{c})}\int_0^\infty e^{-Dk^2(T-t)}J_{1-\tilde{c}}(kz)k^{2-\tilde{c}}dk \\ \approx\ &\left(\frac{z}{2}\right)^{2(1-\tilde{c})}\frac{\epsilon[D(T-t)]^{-2+\tilde{c}}}{2\Gamma(2-\tilde{c})}e^{-\frac{z^2}{4D(T-t)}}.\end{aligned} \tag{4.21}$$

The normalization constant $Z_\epsilon(T)$ can also be determined with $h(x) = \delta(x - \epsilon)$ and $g(x) = \delta(x - \epsilon)$, and is given by

$$\begin{aligned}Z_\epsilon(T) &= \epsilon\int_0^\infty \left[J_{1-\tilde{c}}(k\epsilon)\right]^2 e^{-Dk^2T}kdk \\ &= \frac{\epsilon}{2DT}I_{1-\tilde{c}}\left(\frac{\epsilon^2}{2DT}\right)e^{-\frac{\epsilon^2}{2DT}} \\ &\approx \frac{(\epsilon/2)^{3-2\tilde{c}}}{(DT)^{2-\tilde{c}}\Gamma(2-\tilde{c})},\end{aligned} \tag{4.22}$$

where $I_{1-\tilde{c}}(x)$ is the modified Bessel function of the first kind and $\tilde{c} < 2$ [83]. Combining these final expressions with Eq. (4.18), we arrive at

$$\begin{aligned}P(x,t|T) &= \frac{(x/2)^{3-2\tilde{c}}}{\Gamma(2-\tilde{c})}\left(\frac{T}{Dt(T-t)}\right)^{2-\tilde{c}} \\ &\times\ \exp\left(-\frac{x^2T}{4Dt(T-t)}\right).\end{aligned} \tag{4.23}$$

Finally, the distribution of velocities at a given time t inside an avalanche of duration T follows by a change

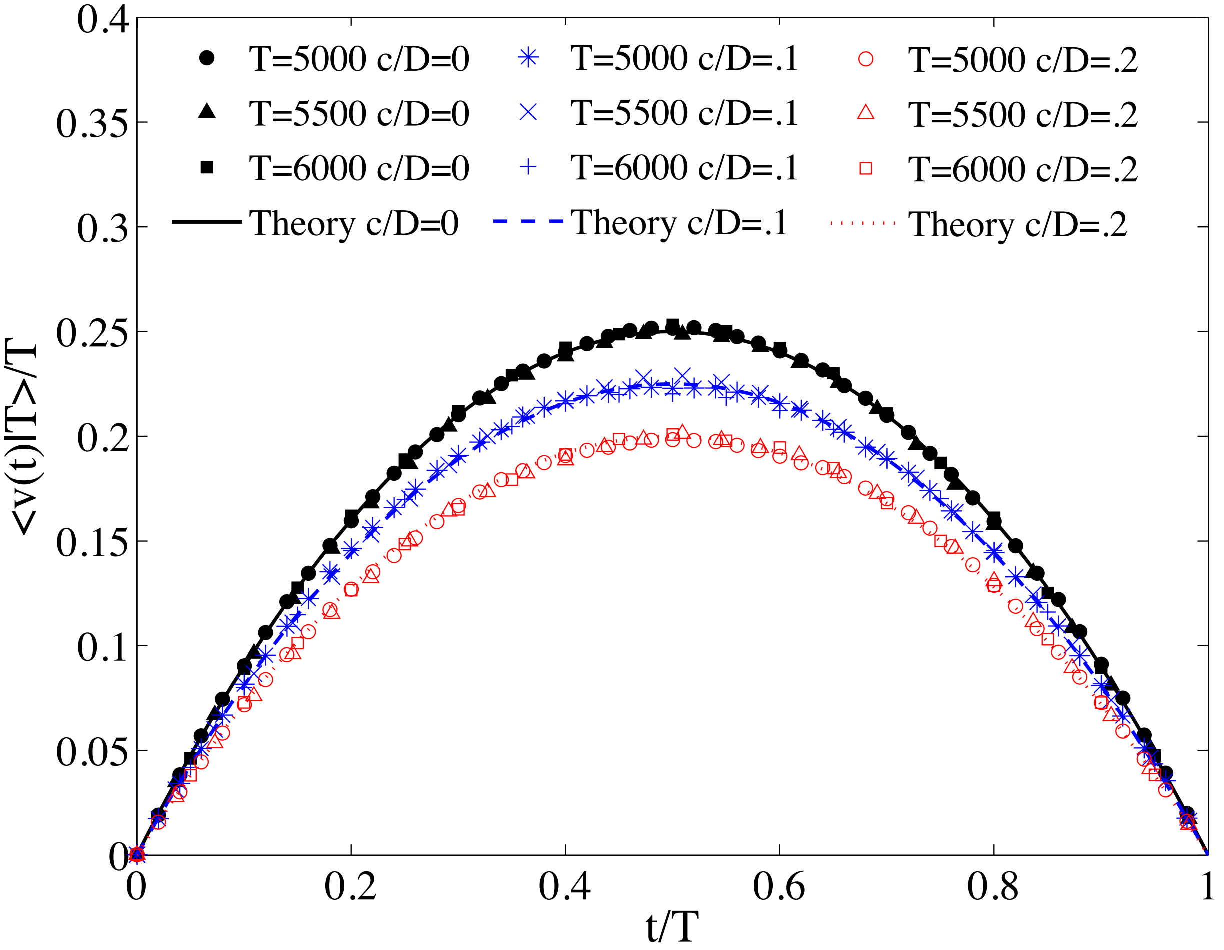

Figure 4.2: Numerical results for the instantaneous velocity $v(t)$ at time t averaged over many avalanches of duration T and rescaled to collapse to the form of Eq. (4.24) with $n = 1$. Results for three different values of the dimensionless driving rate $\tilde{c} = c/D$ are shown. (In the numerics, the driving rate c is varied while the fluctuation strength is fixed at $D = 1/2$.) The parabolic shapes with $\tilde{c}$-dependent height predicted by Eq. (4.25) for $n = 1$ match well with the numerics.

of variable $v = x^2/4$ and is given as

$$P(v,t|T) = \frac{v^{1-\tilde{c}}}{\Gamma(2-\tilde{c})} \left(\frac{T}{Dt(T-t)}\right)^{2-\tilde{c}} \exp\left(-\frac{vT}{Dt(T-t)}\right). \tag{4.24}$$

From Eq. (4.24), we determine the profile of the n-th moments to be

$$\langle v^n(t)|T\rangle = \frac{\Gamma(n+2-\tilde{c})}{\Gamma(2-\tilde{c})} \left(\frac{Dt(T-t)}{T}\right)^n, \tag{4.25}$$

with $n = 1$ corresponding to the avalanche shape $\langle v(t)|T\rangle$ (see Fig. 5.2). We notice that the avalanche shape and higher moment profiles are independent of the driving rate $\tilde{c}$ up to a nonuniversal prefactor. We have also verified this numerically as shown in Fig. (5.2).

This method of obtaining Eq. (4.24) has the advantage of being more intuitive thanks to the correspondence with excursions and we will find that this method continues to be very useful when we compute the statistics of avalanche maxima below. However, Eq. (4.24) can also be obtained from the exact solutions to the untransformed $k \neq 0$ Fokker-Planck equation [71]

$$\partial_t P = D\partial_v^2(vP) + \partial_v((kv-c)P), \tag{4.26}$$

which were obtained by Feller [77]. The exact propagator with an absorbing boundary condition at $v=0$ is given by

$$P(v,t,v_0,0) \quad = \quad \left(\frac{\frac{k}{D}\exp\left(-\frac{\frac{k}{D}(v+v_0e^{-kt})}{1-\exp(-kt)}\right)}{1-e^{-kt}} \right) \left(\frac{v}{v_0 e^{-kt}}\right)^{(\tilde{c}-1)/2} I_{1-\tilde{c}}\left(\frac{2k\sqrt{v_0 v e^{kt}}}{D(e^{kt}-1)}\right), \tag{4.27}$$

assuming that $0 < \tilde{c} < 1$. Repeating the steps above gives

$$P(v,t|T) \quad = \quad \frac{v^{1-\tilde{c}}}{\Gamma(2-\tilde{c})} \left(\frac{\frac{k}{D}\left(1-e^{-kT}\right)}{\left(1-e^{-kt}\right)\left(1-e^{-k(T-t)}\right)} \right)^{2-\tilde{c}} \exp\left(-\frac{\frac{k}{D}v\left(1-e^{-kT}\right)}{\left(1-e^{-kt}\right)\left(1-e^{-k(T-t)}\right)} \right) \tag{4.28}$$

and

$$\langle v^n(t)|T\rangle = \frac{\Gamma(n+2-\tilde{c})}{\Gamma(2-\tilde{c})} \left(\frac{D\left(1-e^{-kt}\right)\left(1-e^{-k(T-t)}\right)}{k\left(1-e^{-kT}\right)} \right)^n, \tag{4.29}$$

which reduce to Eqs. (4.24) and (4.25) when $k \to 0$.

Interestingly, the same avalanche shape is obtained when Eq. (3.9) is interpreted in the Stratonovich sense, as derived in Ref. [70]. In this interpretation, the $x = 2\sqrt{v}$ transformation of the equation of motion is

$$\frac{dx}{dt} = -\frac{k}{2}x + \frac{2c}{x} + \xi(t), \tag{4.30}$$

which is a free Brownian motion in the limit $k = c = 0$. Using the same method as above, the conditional distribution of velocities in avalanches of duration T is (assuming $k = 0$),

$$P_{\text{Strat.}}(v,t|T) = \frac{v^{1/2-\tilde{c}}}{\Gamma(3/2-\tilde{c})} \left(\frac{T}{Dt(T-t)}\right)^{3/2-\tilde{c}} e^{-\frac{vT}{Dt(T-t)}} \tag{4.31}$$

and the n-th moments are

$$\langle v^n(t)|T\rangle_{\text{Strat.}} = \frac{\Gamma(n+3/2-\tilde{c})}{\Gamma(3/2-\tilde{c})} \left(\frac{Dt(T-t)}{T}\right)^n, \tag{4.32}$$

which is indeed identical to the results from the Ito case up to a non-universal, constant pre-factor. In Ref. [70], it is conjectured that the Stratonovich interpretation would give the same results as the Ito interpretation for all universal quantities, but this is not the case. Notice that Eq. (4.30) can be transformed into Eq. (4.1) by a simple parameter shift $c \to c - D/2$. Therefore, any quantity that has c-dependence will be different in the two interpretations. This includes the avalanche size scaling exponent τ and the duration scaling exponent α which have the values $\tau = (3 - \tilde{c})/2$ and $\alpha = 2 - \tilde{c}$ (see Refs. [72, 2] and below). The Stratonovich interpretation predictions for these exponents are then $\tau_S = 5/4 - \tilde{c}/2$ and $\alpha_S = 3/2 - \tilde{c}$. The fact that the Stratonovich interpretation gives the same parabolic avalanche shapes and higher moment profiles is only a reflection of the fact that those quantities do not depend on the driving rate c (except in an overall prefactor).

4.4 Velocity statistics as a function of u for avalanches of fixed size

Velocity statistics for fixed avalanche size can also be easily calculated by these methods if we study velocity as a function of displacement u rather than as a function of time. If we take the u domain equation of motion Eq. (3.5) with $c = 0$ and nonzero k, we get

$$\frac{d\tilde{v}}{du} = -k + w(u), \tag{4.33}$$

where $\langle w(u)w(u')\rangle = 2D\delta(u - u')$. This is a biased Brownian motion.

We can derive $P(\tilde{v}, u|S)$ by the same procedure as we used to derive $P(v, t|T)$. Since the noise is already linear, we do not need to make a change of variables. Eq. (4.33) is the equation of motion of an overdamped particle in a linear potential $V(\tilde{v}) = k\tilde{v}$, evolving in u rather than time. At the end of the avalanche, the total change in u is

$$\Delta u = \int_0^T v(t)dt \equiv S, \tag{4.34}$$

so the avalanche size plays the same role as the duration did for $P(v, t|T)$.

The analogue of Eq. (4.5) is

$$P(\tilde{v}, u|S) \quad = \quad \lim_{\epsilon \to 0} \frac{1}{Z_\epsilon(S)} \int_{v(0)=\epsilon}^{v(S)=\epsilon} \mathcal{D}v(u') e^{-\frac{1}{4D}\int_0^S (\frac{dv}{du'}+k)^2 du'} \delta(v(u) - \tilde{v}) \prod_{0 \le x \le S} \Theta(v(u')). \tag{4.35}$$

where

$$Z_\epsilon(S) = \int_{v(0)=\epsilon}^{v(S)=\epsilon} \mathcal{D}v(u') e^{-\frac{1}{4D}\int_0^S (\frac{dv}{du'}+k)^2 du'} \prod_{0\leq u'\leq S} \Theta(v(u')). \tag{4.36}$$

$P(\tilde{v}, u|S)$ has a corresponding expression in matrix elements (cf. Eq. (4.18)) of

$$P(\tilde{v}, u|S) = \lim_{\epsilon\to 0} \frac{\langle\epsilon|e^{-\hat{H}_2(S-u)}|\tilde{v}\rangle_w \langle\tilde{v}|e^{-\hat{H}_2 u}|\epsilon\rangle_w}{\langle\epsilon|e^{-\hat{H}_2 S}|\epsilon\rangle_w}, \tag{4.37}$$

where the Hamiltonian is now given by

$$\hat{H}_2 = -D\frac{\partial^2}{\partial\tilde{v}^2} - \frac{\partial}{\partial\tilde{v}}V'(\tilde{v}) = -D\frac{\partial^2}{\partial\tilde{v}^2} - k\frac{\partial}{\partial\tilde{v}} \tag{4.38}$$

with a infinite wall boundary condition at $\tilde{v} = 0$. The eigenfunctions of this Hamiltonian satisfying the boundary condition are

$$f_q(\tilde{v}) = \sqrt{\frac{2}{\pi}}\sin(q\tilde{v})e^{-k\tilde{v}/2D}, \tag{4.39}$$

with eigenvalues

$$E_q = D\left(\left(\frac{k}{2D}\right)^2 + q^2\right) \tag{4.40}$$

for $0 < q < \infty$.

The matrix element can be written

$$\langle\tilde{v}|e^{-\hat{H}_2 u}|\epsilon\rangle_w = \int_0^\infty dx\delta(x-\tilde{v})e^{-\hat{H}_2 u}\delta(x-\epsilon). \tag{4.41}$$

We can expand the second δ-function in terms of the eigenfunctions as

$$\delta(x-\epsilon) = \sqrt{\frac{2}{\pi}}\int_0^\infty dq g(q)e^{-kx/2D}\sin(qx), \tag{4.42}$$

where

$$g(q) = \sqrt{\frac{2}{\pi}}\int_0^\infty dx e^{kx/2D}\delta(x-\epsilon)\sin(qx) = \sqrt{\frac{2}{\pi}}e^{k\epsilon/2D}\sin(q\epsilon). \tag{4.43}$$

so that

$$\begin{aligned}
\langle\tilde{v}|e^{-\hat{H}_2 u}|\epsilon\rangle_w &= \int_0^\infty dx\delta(x-\tilde{v})\int_0^\infty dq\sqrt{\frac{2}{\pi}}e^{-D\left(\left(\frac{k}{2D}\right)^2+q^2\right)u}g(q)e^{-kx/2D}\sin(qx) \\
&= \frac{2}{\pi}e^{k(\epsilon-\tilde{v})/2D}e^{-\frac{1}{4D}k^2 u}\int_0^\infty dq\sin(q\epsilon)\sin(q\tilde{v})e^{-Duq^2} \\
&\approx \frac{1}{2\sqrt{\pi}}e^{-k\tilde{v}/2D}e^{-\frac{1}{4D}k^2 u}\frac{\epsilon\tilde{v}}{(Du)^{3/2}}e^{-\frac{\tilde{v}^2}{4Du}}
\end{aligned} \tag{4.44}$$

where in the third line, we expanded the expression to first order in ϵ and used the identity $\int_0^\infty x\sin(ax)e^{-x^2}dx = \frac{\sqrt{\pi}}{4}ae^{-a^2/4}$.

Similar calculations give

$$\langle\epsilon|e^{-\hat{H}_2(S-u)}|\tilde{v}\rangle_w \approx \frac{1}{2\sqrt{\pi}}e^{k\tilde{v}/2D}e^{-\frac{1}{4D}k^2(S-u)}\frac{\epsilon\tilde{v}}{(D(S-u))^{3/2}}e^{-\frac{\tilde{v}^2}{4D(S-u)}} \tag{4.45}$$

and

$$\langle\epsilon|e^{-\hat{H}_2 S}|\epsilon\rangle_w \approx \frac{1}{2\sqrt{\pi}}e^{-\frac{1}{4D}k^2 S}\frac{\epsilon^2}{(DS)^{3/2}} \tag{4.46}$$

Putting it all together, the probability distribution for velocity as a function of u is then

$$\begin{aligned} P(\tilde{v},u|S) &= \lim_{\epsilon\to 0}\frac{\langle\epsilon|e^{-\hat{H}_2(S-u)}|\tilde{v}\rangle_w\langle\tilde{v}|e^{-\hat{H}_2 u}|\epsilon\rangle_w}{\langle\epsilon|e^{-\hat{H}_2 S}|\epsilon\rangle_w} \\ &= \frac{1}{2\sqrt{\pi}}\tilde{v}^2\left(\frac{S}{Du(S-u)}\right)^{3/2}\exp\left(-\frac{\tilde{v}^2 S}{4Du(S-u)}\right). \end{aligned} \tag{4.47}$$

From this distribution, we can get the moment profiles in u:

$$\langle v(u)^n|S\rangle = \int\tilde{v}^n P(\tilde{v},u|S)d\tilde{v} = \frac{2^{n+1}}{\sqrt{\pi}}\Gamma\left(\frac{n+3}{2}\right)\left(\frac{Du(S-u)}{S}\right)^{n/2}. \tag{4.48}$$

In particular, the average velocity as a function of u during an avalanche of size S has a semi-circular shape.

4.5 Overall duration and size distributions

The overall duration distribution is proportional to the probability that an avalanche returns to the origin at time T, assuming we use absorbing boundary conditions to guarantee that it will remain strictly positive in between. This means that, from Eq. (4.27), we have

$$\begin{aligned} P(T) &= \lim_{\epsilon\to 0}N(\epsilon)P(\epsilon;T,\epsilon,0) \\ &= \lim_{\epsilon\to 0}N(\epsilon)\left(\frac{2k}{1-e^{-kT}}\right)^{2-\tilde{c}}\frac{e^{(\tilde{c}-1)kT}\epsilon^{1-\tilde{c}}}{\Gamma(2-\tilde{c})}, \end{aligned} \tag{4.49}$$

where $N(\epsilon)$ is a proportionality constant that cannot simply be set by normalization since $P(\epsilon,T;\epsilon,0)\sim T^{-2+\tilde{c}}$ for $T\to 0$ and the normalization integral diverges at this limit. This divergence must occur because we expect that the return time to the origin gets shorter as the starting value ϵ gets closer to zero. To get rid of it, we need to set a cutoff $T^*\sim\epsilon$ defined as the minimum duration of an observable avalanche.

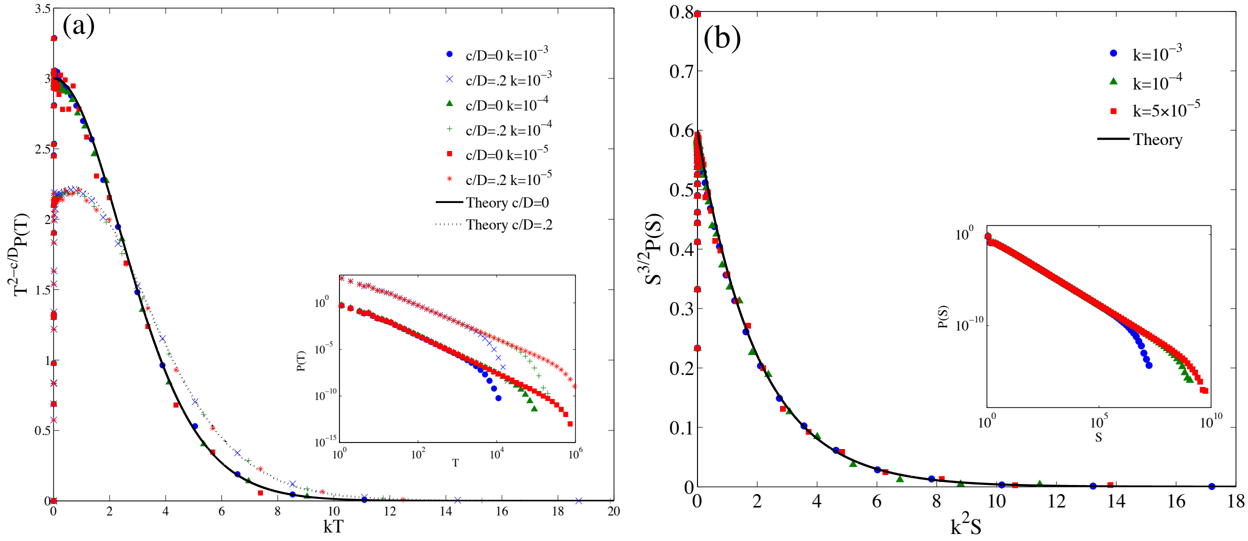

Figure 4.3: (a) Numerical scaling collapse of the avalanche duration distribution $P(T)$ for different values of k (see the caption to Table 5.1 for the definition) and the driving rate $c \equiv \langle v \rangle / k$ to the form of Eq. (4.50). The scaling functions plotted are $F_{\tilde{c}}(x) = C(\tilde{c}) e^x x^{2-\tilde{c}} (e^x - 1)^{\tilde{c}-2}$ which are proportional to the ones given in Eq. (4.50). The non-universal constants are fit by eye as $C(0) = 3.0$ and $C(.2) = 3.375$. The inset shows the same distributions before rescaling with the curves for $\tilde{c} = 0.2$ offset for visibility. (b) Collapse of the size distributions for different values of k to the form of Eq. (4.52). The theoretical curve plotted is $F(x) = C \exp(-x/2)$ where $C = 0.6$ which is, up to normalization, what is given in Eq. (4.52) with $D = 1/2$. The inset shows the size distributions before rescaling.

The natural long duration cutoff is set by $1/k$. Assuming that these cutoffs are well-separated, namely that $kT^* \ll 1$, we have

$$P(T) = k(1-\tilde{c})(kT^*)^{1-\tilde{c}} e^{kT} \left(\frac{1}{e^{kT} - 1} \right)^{2-\tilde{c}} \tag{4.50}$$

for $T > T^*$. This has power law behavior $P(T) \sim T^{-\alpha} \mathcal{G}(kT)$ with exponent $\alpha = 2 - \tilde{c}$ and $\mathcal{G}(x)$ a cutoff function, as can be seen by taking the limit $k \to 0$. The exponent agrees with the one reported in Refs. [72, 2]. In Fig. 4.3a we numerically verify Eq. (4.50) for different values of c and k.

For the avalanche size distribution, similar reasoning to Eq. (4.49) gives $P(S) \propto \langle \epsilon | e^{-\hat{H}_2 S} | \epsilon \rangle_w$. Plugging in Eq. (4.46),

$$P(S) \propto \frac{\epsilon^2}{(DS)^{3/2}} e^{-\frac{1}{4D} k^2 S}. \tag{4.51}$$

Normalizing with a minimum avalanche size S^* gives

$$P(S) = \frac{\sqrt{S^*}}{2S^{3/2}} e^{-\frac{1}{4D} k^2 S}. \tag{4.52}$$

A slightly different definition of an avalanche has the avalanche start at a (small) initial velocity v_0 and ending when the velocity goes below zero. In this case, referring to Eq. (4.45), we have

$$\begin{aligned} P(S) &\propto \langle\epsilon|e^{-\hat{H}_2 S}|v_0\rangle_w \\ &\propto e^{kv_0/2D}e^{-\frac{1}{4D}k^2 S}\frac{\epsilon v_0}{(DS)^{3/2}}e^{-\frac{v_0^2}{4DS}} \\ &= \epsilon\frac{v_0}{(DS)^{3/2}}e^{-\frac{1}{4DS}(kS-v_0)^2}. \end{aligned} \tag{4.53}$$

Normalizing the RHS of Eq. (4.53) does not require a small size cutoff unless $v_0 = 0$ since the distribution has a factor $\exp(-v_0^2/4DS)$ that cuts off the small avalanche sizes. The properly normalized result is

$$P(S) = \frac{v_0}{\sqrt{4\pi D}}\frac{1}{S^{3/2}}e^{-\frac{1}{4DS}(kS-v_0)^2}. \tag{4.54}$$

Note that it approaches the form of Eq. (4.52) as $v_0 \to 0$.

The distribution defined by Eq. (4.54) is the Brownian first passage time distribution for a random walk with drift, which can be derived by methods more rigorous than ours (see, for instance, [68]). Note the similarity to the argument leading to Eq. (2.17) for the size distribution in the context of the cellular model. We chose to use the same methods we used for avalanches of fixed duration on the fixed size avalanches rather than using more well-established methods for random walks with drift to show that (encouragingly) they get the same results. The duration and size distributions for ABBM avalanches Eqs. (4.54) and (4.50) have also been obtained independently, using different methods in [84, 74]. Here the ABBM path integral with an auxilliary field is solve through an exactly solvable saddle point equation. These methods can also been extended to solve the ABBM model for more general driving forces [85] and extend to analytically tractable models of spatial structure [86].

Chapter 5

Distributions of maximum velocities

5.1 Introduction

Several acoustic emission (AE) experiments on small-scale plastic deformations of single crystals, e.g. ice, Cd, Zn, and Cu, report robust power law scaling in the statistics of the maximum amplitude A_m of acoustic waves emitted during plastic slip avalanches. The probability distribution density of the maximum AE amplitude follows a power-law tail $P(A_m) \sim A_m^{-\mu}$, with an exponent $\mu \approx 2$ [51, 52, 9, 25, 26, 53]. Since many slip avalanches are required to obtain good statistics for $P(A_m)$, the deviations in the values of μ could depend on the experimental resolution. Nevertheless, the exponent is remarkably robust to variations such as loading mode, type of crystal, temperature, forest hardening effect, or plastic anisotropy [25, 26, 53]. Under certain conditions, it is argued that the maximum amplitude A_m is a measure of the area swept by the fast-moving dislocations [51, 52]. The same power law exponent for the maximum velocity distribution has been observed using high-resolution extensometry, a technique that directly measures the maximum avalanche velocity [26].

In this chapter, we[1] derive several statistical quantities related to the maximum velocity of an avalanche. We obtain the value $\mu = 2$ for the power-law exponent, in agreement with experiment and derive many other measurable quantities. We also argue that the maximum velocity can be a more robust observable than the avalanche duration.

Much of work done in this chapter was originally reported in [49, 50].

5.2 Maximum velocity statistics for avalanches of fixed duration

We now determine the extreme value distribution of the maximum velocity inside avalanches of fixed duration T, for $k = 0$ and nonzero c. Using the mapping to the random excursions, we first determine the statistics of the maximal displacements in excursions over a fixed interval. Let us consider an excursion $\{x(t)\}_t$ in the

---

[1] The work in this section was done in collaboration with Luiza Angheluta, Karin Dahmen and Nigel Goldenfeld

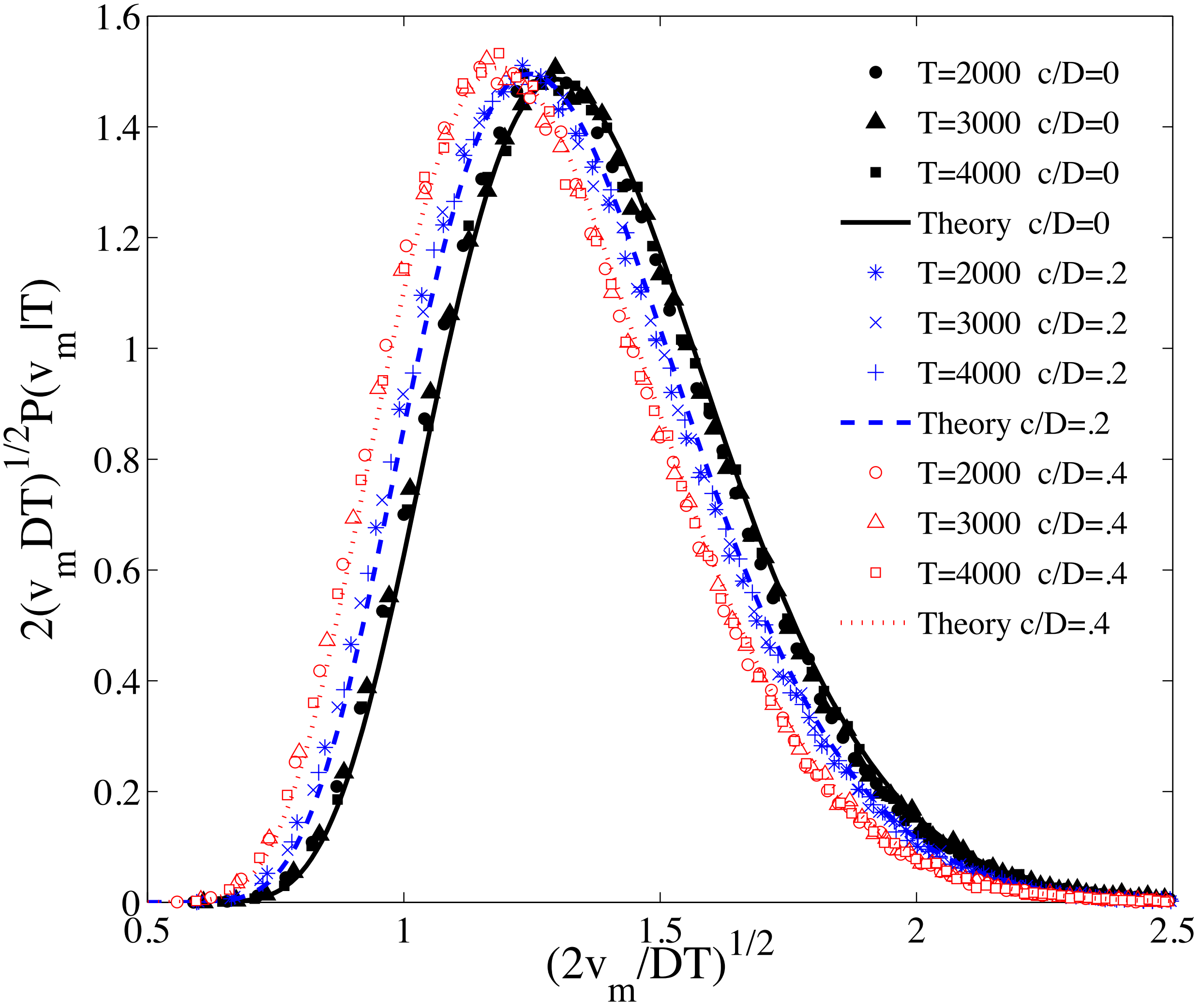

Figure 5.1: Scaling collapses of numerical results of $P(v_m|T)$, the distribution of maximum velocities for avalanches of duration T, onto the form given by Eq. (5.12) performed for several values of the dimensionless driving rate $\tilde{c} = c/D$. (In the numerics, the driving rate c is varied while the fluctuation strength is fixed at $D = 1/2$.) The corresponding scaling functions $F(x)$ given by Eq. (5.13) fit very well with the numerics.

time interval $0 \leq t \leq T$. The probability distribution at a fixed time t is given by $P(x,t|T)$ from Eq. (4.23), which can be written

$$P(x,t|T) = \frac{1}{\sigma_t} Q_{RE}\left(\frac{x}{2\sigma_t}\right), \tag{5.1}$$

with $Q_{RE}(y) = y^{3-2\tilde{c}} e^{-y^2}/\Gamma(2-\tilde{c})$ and $\sigma_t = \sqrt{Dt(T-t)/T}$. Notice that because σ_t is different for every point inside the excursion, it follows that the variables $x(t)$ are not identically distributed. Furthermore, the individual distributions are non-Gaussian for small x, but converge to a Gaussian right tail for large enough

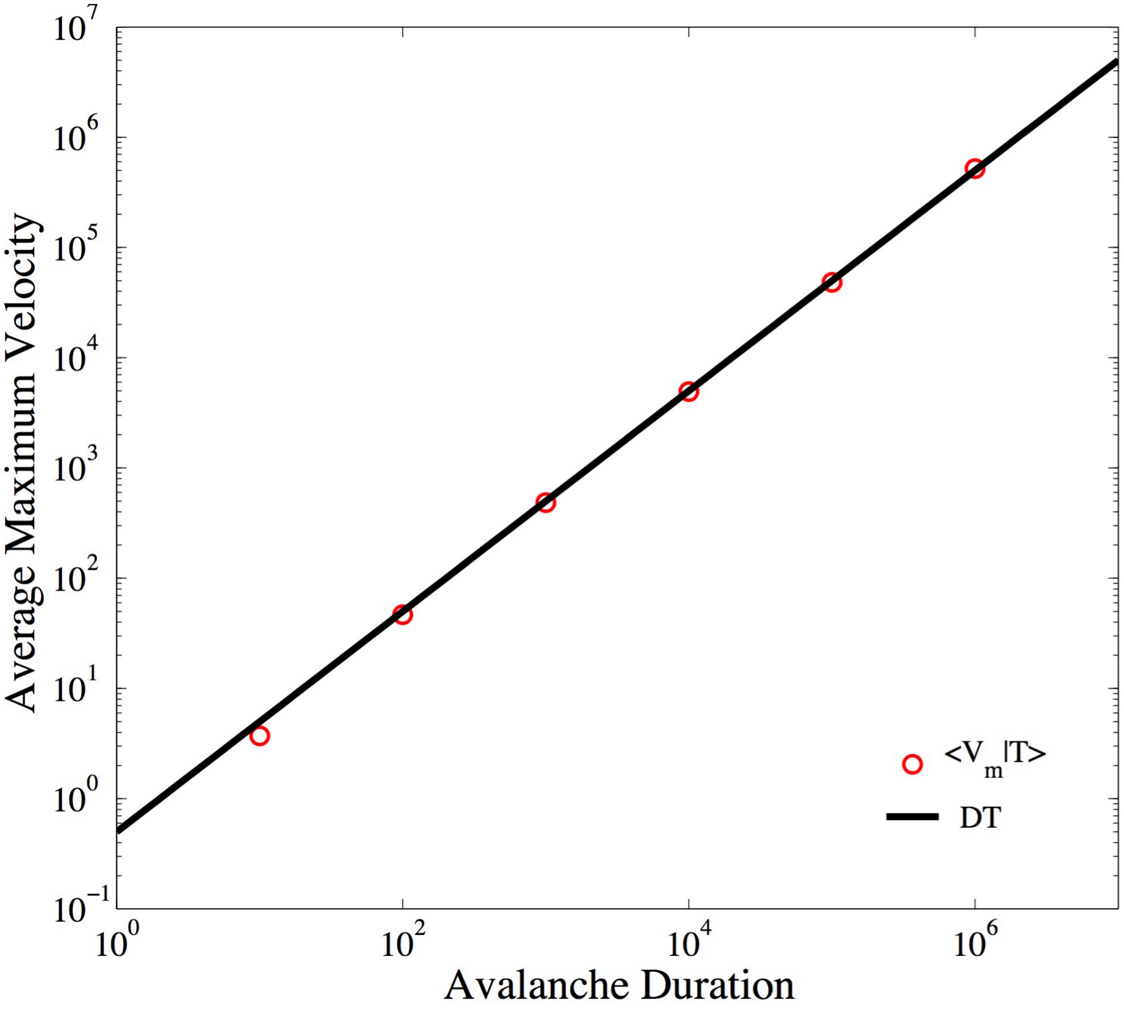

Figure 5.2: $\langle v_m|T\rangle$ as a function of T, with the solid line representing the analytical solution from Eq. (5.15) with $D = 1/2$.

x. The maximum displacement in an excursion is defined as

$$M = \max_{0 \leq t \leq T} x(t), \tag{5.2}$$

with a probability distribution determined from the properties of $P(x, t|T)$. This follows from the fact that the probability of the maximum being less than a certain value $M < x_m$ is the same as the probability that at every instant during the excursion the displacement $x(t)$ is less than x_m. The path integral representing this cumulative probability is

$$C_\epsilon(x_m|T) \quad = \quad \frac{1}{Z_\epsilon(T)} \int_{x(0)=\epsilon}^{x(T)=\epsilon} \mathcal{D}x(t) e^{-\int_0^T L_E(x,\dot{x})dt} \prod_{0 \leq t \leq T} \Theta(x(t))\Theta(x_m - x(t)), \tag{5.3}$$

where $L_E(x,\dot{x}) = \frac{1}{4D}\left(\dot{x} + \frac{D-2c}{x}\right)^2$ and the product over the Heaviside functions selects the excursion paths that satisfy the constraint that the position at any time is less than x_m. The normalization constant $Z_\epsilon(T)$, corresponding to the path integral over all excursions, was calculated previously in Eq. (4.22). At the end of the calculation, we take the limit as $\epsilon \to 0$, so that the path starts and ends at the origin, staying between 0 and x_m during an avalanche of duration T. On the other hand, $C_\epsilon(x_m|T)$ is also the probability that $M < x_m$, namely

$$C_\epsilon(x_m|T) = \int_{-\infty}^{x_m} dM P_\epsilon(M|T), \tag{5.4}$$

thus, the PDF $P_\epsilon(x_m|T)$ follows directly by a differentiation of $C_\epsilon(x_m|T)$ with respect to x_m.

Using the quantum analogue, the path integral in Eq. (5.3) is equal to a transition amplitude between the position eigenstate $|\epsilon\rangle$ and itself, and thus can be computed by an expansion in energy eigenfunctions:

$$C_\epsilon(x_m|T) \quad = \quad \frac{\langle\epsilon|e^{-\hat{H}_1 T}|\epsilon\rangle_b}{\langle\epsilon|e^{-\hat{H}_1 T}|\epsilon\rangle_w}, \tag{5.5}$$

with

$$\langle\epsilon|e^{-\hat{H}_1 T}|\epsilon\rangle_b = \int_0^{x_m} dx\delta(x-\epsilon)e^{-\hat{H}_1 T}\delta(x-\epsilon), \tag{5.6}$$

where the Hamiltonian $\hat{H}_1$ has square-well (box) boundary conditions at $x = 0$ and $x = x_m$. With these boundary conditions, the Hamiltonian has a discrete spectrum of eigenfunctions given by

$$f_n(x) = x^{\tilde{c}} J_{1-\tilde{c}}\left(\frac{\lambda_n x}{x_m}\right), \tag{5.7}$$

with eigenvalues $E_n = D\lambda_n^2/x_m^2$, where λ_n is the n'th zero of the Bessel function $J_{1-\tilde{c}}(x)$. The δ-function in Eq. (5.6) can be expanded in this basis as

$$\delta(x-\epsilon) = \frac{2\epsilon^{1-\tilde{c}}}{x_m^2}\sum_n \frac{J_{1-\tilde{c}}\left(\frac{\lambda_n \epsilon}{x_m}\right)}{\left(J_{2-\tilde{c}}(\lambda_n)\right)^2} f_n(x), \tag{5.8}$$

with $f_n(x)$'s defined in Eq. (5.7). Inserting this expansion into the definition of the matrix element from Eq. (5.6), we obtain

$$\langle\epsilon|e^{-\hat{H}_1 T}|\epsilon\rangle_b = 2\epsilon \sum_{n=1}^{\infty}\left[\frac{J_{1-\tilde{c}}\left(\frac{\lambda_n \epsilon}{x_m}\right)}{x_m J_{2-\tilde{c}}(\lambda_n)}\right]^2 e^{-\frac{D\lambda_n^2 T}{x_m^2}}. \tag{5.9}$$

Finally, inserting the solution of $Z_\epsilon(T)$ from Eq. (4.22) into Eq. (5.5), and taking the limit of $\epsilon \to 0$, we arrive at the expression for the extreme value statistics of the random displacements $C(x_m|T) = \lim_{\epsilon\to 0} C_\epsilon(x_m|T)$, namely

$$C(x_m|T) \quad = \quad \frac{2^{\tilde{c}}(DT)^{2-\tilde{c}}}{\Gamma(2-\tilde{c})x_m^{4-2\tilde{c}}} \sum_{n=1}^{\infty} \frac{\lambda_n^{2(1-\tilde{c})}}{[J_2(\lambda_n)]^2} e^{-\frac{\lambda_n^2 DT}{x_m^2}} . \tag{5.10}$$

The distribution $P(x_m|T)$ of the maximum displacements follows from the cumulative distribution as $P(x_m|T) = \partial_{x_m} C(x_m|T)$. The corresponding PDF of the maximal avalanche velocities is obtained by the change of variable $x_m = 2\sqrt{v_m}$ and the transformation

$$P(v_m|T) = P(x_m|T) \left| \frac{dv_m}{dx_m} \right|^{-1} . \tag{5.11}$$

It follows that the PDF $P(v_m|T)$ is given by

$$P(v_m|T) = \frac{1}{\sqrt{2Dv_mT}} F\left(\sqrt{\frac{2v_m}{DT}}\right) \tag{5.12}$$

with the scaling function given by

$$F(x) = \frac{2^{\tilde{c}}}{\Gamma(2-\tilde{c})} \frac{1}{x^{5-2\tilde{c}}} \sum_{n=1}^{\infty} \frac{\lambda_n^{2-2\tilde{c}}}{[J_{2-\tilde{c}}(\lambda_n)]^2} \left(\frac{\lambda_n^2}{x^2} - (4-2\tilde{c})\right) e^{-\frac{\lambda_n^2}{2x^2}} . \tag{5.13}$$

We have numerically verified Eq. (5.12) for different values of $\tilde{c}$ and $k = 0$. Our collapsed distributions, as shown in Fig. 5.1, are in excellent agreement with the analytically predicted scaling function from Eq. (5.13).

From the conditional distribution of Eq. (5.12), we can readily compute how the moments of $P(v_m|T)$ scale with T, which may be easier to compare with experiments with limited statistics. We get

$$\begin{aligned} \langle v_m^n|T\rangle \quad &= \quad \int v_m^n P(v_m|T) dv_m \\ &= \quad \int_0^\infty v_m^{n-1} \frac{1}{2}\sqrt{\frac{2v_m}{DT}} F\left(\sqrt{\frac{2v_m}{DT}}\right) dv_m \\ &= \quad \frac{1}{2}\left(\frac{DT}{2}\right)^n \int_0^\infty z^{n-1+1/2} F(z) dz \\ &\sim \quad (DT)^n. \end{aligned} \tag{5.14}$$

In particular, the mean maximum velocity for an avalanche of duration T, we have

$$\langle v_m|T\rangle = DT \tag{5.15}$$

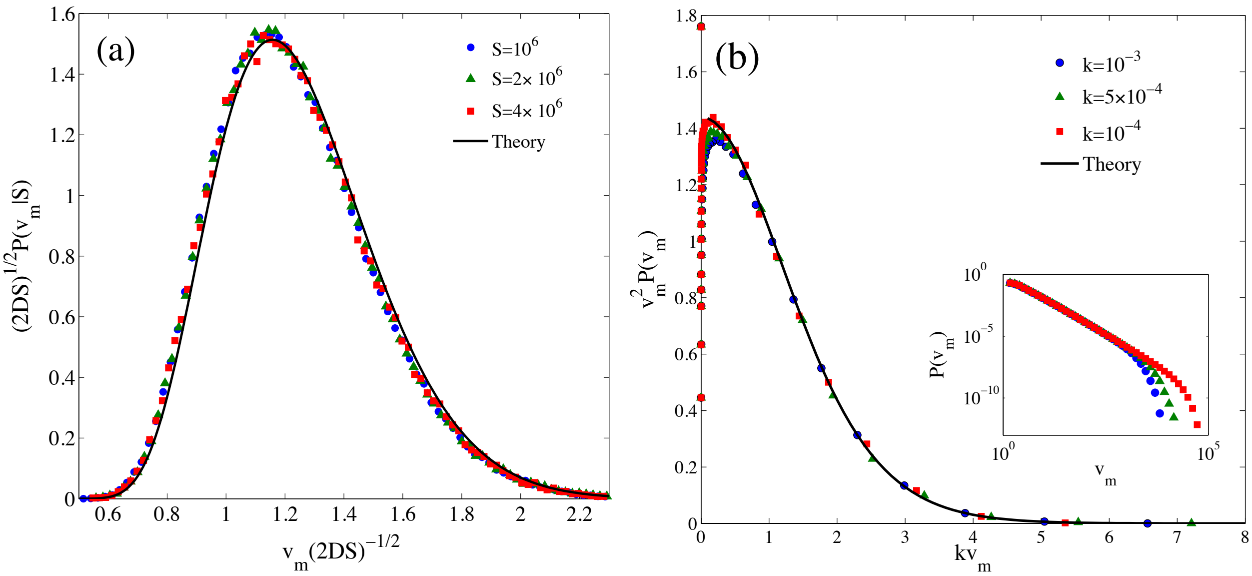

Figure 5.3: (a) Scaling collapse of $P(v_m|S)$, the distribution of maximum velocities for avalanches of size S, onto the form of Eq. (5.31). The rescaled distributions approach the analytical scaling function from Eq. (5.32) for sufficiently large avalanche sizes. (b) Scaling collapse for the overall maximum velocity distribution, $P(v_m)$ for quasistatic driving ($c = 0$) and several different values of k (see the caption of Table 5.1 for the physical definition) to the form of Eq. (5.40). The scaling function plotted is $F(x) = Cx^2 \sinh^{-2}(x)$ where the constant $C = 1.44$ is adjusted to fit near the tail and is proportional to that given in Eq. (5.40) with $D = 1/2$. Adjustment of this non-universal constant factor is required since the part of the distribution near the origin that deviates from scaling alters the overall normalization. The inset shows the same maximum velocity distributions before rescaling.

(the unimportant overall constant turns out to be exactly one). We plot Eq. (5.15) in Fig. 5.2.

5.3 Maximum velocity statistics for fixed avalanche size

Using the same technique as in the previous section, we determine the distribution of maximum events in avalanches of a given size. Here, we consider Eq. (3.5) with $c = 0$ and nonzero k

$$\frac{d\tilde{v}}{du} = -k + w(u), \tag{5.16}$$

where $\langle w(u)w(u')\rangle = 2D\delta(u-u')$. This is a Brownian motion in a linear potential $V(\tilde{v}) = k\tilde{v}$.

The cumulative distribution $C(v_m|S)$ conditioned on fixed avalanche sizes is defined by the path integral

$$C_\epsilon(v_m|S) = \frac{1}{Z_\epsilon(S)} \int_{\tilde{v}(0)=\epsilon}^{\tilde{v}(S)=\epsilon} \mathcal{D}\tilde{v}(u) e^{-\frac{1}{4D}\int_0^S (\dot{\tilde{v}}(u)+k)^2 du} \prod_{0\le u\le S} \Theta(\tilde{v}(u))\Theta(v_m - \tilde{v}(u)), \tag{5.17}$$

where the normalization factor is the path integral over the unconstrained excursions,

$$Z_\epsilon(S) \quad = \quad \int_{\tilde{v}(0)=\epsilon}^{\tilde{v}(S)=\epsilon} \mathcal{D}\tilde{v}(u) e^{-\frac{1}{4D}\int_0^S (\dot{\tilde{v}}(u)+k)^2 du} \prod_{0 \le u \le S} \Theta(\tilde{v}(u)). \tag{5.18}$$

Instead of duration T as in the previous calculation, the value of u at the end of an avalanche is the slip size of the avalanche

$$S \equiv \int_0^T v(t) dt. \tag{5.19}$$

The path integral in Eq. (5.18) is equivalent to the transition amplitude between the position eigenstate $|\epsilon\rangle$ and itself, and thus can be computed by an expansion in energy eigenfunctions:

$$Z_\epsilon(S) \quad = \quad \langle \epsilon | e^{-\hat{H}_2 S} | \epsilon \rangle_w, \tag{5.20}$$

where

$$\hat{H}_2 = -D\partial_{\tilde{v}}^2 - k\partial_{\tilde{v}} \tag{5.21}$$

with an absorbing boundary condition at $\tilde{v} = 0$. The eigenfunctions for this Hamiltonian are

$$f_q(\tilde{v}) = \sqrt{\frac{2}{\pi}} \sin(q\tilde{v}) e^{-k\tilde{v}/2D}, \tag{5.22}$$

with eigenvalues satisfying

$$E_q = D\left(\left(\frac{k}{2D}\right)^2 + q^2\right) \tag{5.23}$$

for $0 < q < \infty$. Therefore, the $Z_\epsilon(S)$ from Eq. (5.20) becomes

$$Z_\epsilon(S) = \int_0^\infty d\tilde{v} \delta(\tilde{v} - \epsilon) e^{-\hat{H}_2 S} \delta(\tilde{v} - \epsilon). \tag{5.24}$$

We expand the δ-function in terms of the eigenfunctions as

$$\delta(\tilde{v} - \epsilon) = \sqrt{\frac{2}{\pi}} \int_0^\infty dq g(q) e^{-k\tilde{v}/2D} \sin(q\tilde{v}), \tag{5.25}$$

where

$$g(q) = \sqrt{\frac{2}{\pi}} \int_0^\infty d\tilde{v} e^{k\tilde{v}/2D} \delta(\tilde{v} - \epsilon) \sin(q\tilde{v}). \tag{5.26}$$

Applying this to the second delta function and Taylor expanding in the lowest order of ϵ, we arrive at

$$\begin{aligned} Z_\epsilon(S) &= \frac{2}{\pi}\int_0^\infty dq \sin^2(q\epsilon) e^{-D\left(\left(\frac{k}{2D}\right)^2+q^2\right)S} \\ &\approx \sqrt{\frac{2}{\pi}}\frac{\epsilon^2}{(2DS)^{3/2}} e^{-\frac{1}{4D}k^2 S}. \end{aligned} \tag{5.27}$$

Similarly, the numerator path integral in Eq. (5.17) is determined by expanding in the discrete set of eigenfunction of the Hamiltonian $\hat{H}_2$ with square-well boundary conditions at $\tilde{v} = 0$ and $\tilde{v} = v_m$. The eigenfunctions are

$$f_n(\tilde{v}) = \sqrt{\frac{2}{v_m}} \sin^2\left(\frac{n\pi\tilde{v}}{v_m}\right) e^{-k\tilde{v}/2D}, \tag{5.28}$$

with the eigenvalues $E_n = D\left(\frac{n^2\pi^2}{v_m^2} + \left(\frac{k}{2D}\right)^2\right)$. Therefore, we obtain that

$$C_\epsilon(v_m|S) = \frac{1}{Z_\epsilon(S)}\frac{2}{v_m}\sum_{i=1}^{\infty}\sin^2\left(\frac{n\pi\epsilon}{v_m}\right)\exp\left(-DS\left(\frac{n^2\pi^2}{v_m^2}+\left(\frac{k}{2D}\right)^2\right)\right), \tag{5.29}$$

which, in the limit of $\epsilon \to 0$, leads to

$$C(v_m|S) = \frac{\sqrt{2\pi}(2DS)^{3/2}}{v_m}\sum_{n=1}^{\infty}\left(\frac{n\pi}{v_m}\right)^2\exp\left(-\frac{\pi^2 n^2 DS}{v_m^2}\right). \tag{5.30}$$

Interestingly, k has canceled completely out of the final answer.

Differentiating with respect to v_m in Eq. (5.30), we obtain the PDF for v_m given by the scaling form

$$P(v_m|S) = \frac{1}{\sqrt{2DS}} F_S\left(\frac{v_m}{\sqrt{2DS}}\right), \tag{5.31}$$

where $F_S(x)$ is the Brownian excursion scaling function

$$F_S(x) = \frac{\sqrt{2\pi}}{x^4}\sum_{n=0}^{\infty} n^2\pi^2\left(\frac{n^2\pi^2}{x^2} - 3\right)e^{-\frac{n^2\pi^2}{2x^2}}. \tag{5.32}$$

Using the Poisson summation formula [87]

$$\sum_{n=\infty}^{\infty} e^{-ny^2} = \sqrt{\frac{\pi}{y}}\sum_{n=\infty}^{\infty} e^{-n^2\pi^2/y^2}, \tag{5.33}$$

the scaling function can be written

$$F_S(x) = \sum_{n=1}^{\infty}(32n^4x^3 - 24n^2x)e^{-2n^2x^2}, \tag{5.34}$$

and we can see it has the asymptotic form

$$F_S(x) = \begin{cases} \sqrt{2\pi^5}\left(\frac{\pi^2}{x^6} - \frac{3}{x^4}\right) e^{-\frac{\pi^2}{2x^2}} & , x \to 0 \\ \\ (32x^3 - 24x)e^{-2x^2} & , x \to \infty, \end{cases} \tag{5.35}$$

which guarantees that all of its moments are finite. In Fig. 5.3, we present the numerically computed distribution of maximal velocities for different avalanche sizes which agrees very well with the analytical result. The rescaled PDF $P(v_m|S)$ collapses onto a scaling form as predicted by Eq. (5.32)

5.4 Overall max velocity distribution

The tail behavior of the overall distribution $P(v_m)$ of avalanche maxima can then be derived in the adiabatic limit by integrating Eq. (5.32) against the overall size distribution Eq. (4.52),

$$\begin{aligned} P(v_m) &= \int_{S^*}^{\infty} P(v_m|S)P(S)dS \\ &= \frac{\sqrt{2DS^*}}{2v_m^2} \int_0^{\frac{v_m}{\sqrt{2DS^*}}} xF_S(x)e^{-\frac{1}{2}\left(\frac{kv_m}{2Dx}\right)^2} dx. \end{aligned} \tag{5.36}$$

The asymptotic behavior of the integrand allows us to take the upper limit of the integral to infinity provided $v_m \gg \sqrt{2DS^*}$. The infinite sum can then be integrated term by term using the formula

$$\int_0^{\infty} x^n e^{-Ax^2 - B/x^2} dx = A^{-\frac{n+1}{4}} B^{\frac{n+1}{4}} K_{\frac{n+1}{2}}\left(2\sqrt{AB}\right), \tag{5.37}$$

where $K_\nu(x)$ is the modified Bessel function of the second kind. In this way, the correction factor to v_m^{-2}-scaling becomes

$$\int_0^{\infty} xF_S(x)e^{-\frac{1}{2}\left(\frac{kv_m}{2Dx}\right)^2} dx = \sqrt{\frac{\pi}{2}}\left(\frac{kv_m}{D}\right)^2 \sum_{n=1}^{\infty} ne^{-\frac{nkv_m}{D}}. \tag{5.38}$$

The infinite series can be summed using the formula $\sum_n n\exp(-nx) = 4/\sinh^2(x/2)$, giving

$$\int_0^{\infty} xF_S(x)e^{-\frac{1}{2}\left(\frac{kv_m}{2Dx}\right)^2} dx = \sqrt{8\pi}\left(\frac{\frac{kv_m}{D}}{\sinh\left(\frac{kv_m}{2D}\right)}\right)^2. \tag{5.39}$$

Quantity	Form	MFT values
Avalanche size distribution	$P(S) \sim S^{-\tau}\mathcal{F}(k^{1/\sigma}S)$	$\tau = \frac{3}{2}, \quad \sigma = \frac{1}{2}$
Duration distribution	$P(T) \sim T^{-\alpha}\mathcal{G}(k^{\nu z}T)$	$\alpha = 2, \quad \nu z = 1$
Maximum velocity distribution	$P(v_m) \sim v_m^{-\mu}\mathcal{H}(k^{\rho}v_m)$	$\mu = 2, \quad \rho = 1$
Maximum energy ($E_m \equiv v_m^2$) distribution	$P(E_m) \sim E_m^{-(\mu/2+1/2)}\mathcal{H}(k^{\rho}E_m^{1/2})$	$\frac{\mu}{2} + \frac{1}{2} = \frac{3}{2}, \quad 2\rho = 2$
Stress-integrated size distribution	$P_{\text{int}}(S) \sim S^{-(\tau+\sigma)}$	$\tau + \sigma = 2$
Stress-integrated duration distribution	$P_{\text{int}}(T) \sim T^{-(\alpha+\frac{1}{\nu z})}$	$\alpha + \frac{1}{\nu z} = 3$
Stress-integrated maximum velocity distribution	$P_{\text{int}}(v_m) \sim v_m^{-(\mu+\frac{1}{\rho})}$	$\mu + \frac{1}{\rho} = 3$
Stress-integrated max energy ($E_m \equiv v_m^2$) dist.	$P_{\text{int}}(E_m) \sim E_m^{-\left(\frac{1}{2}(\mu+\frac{1}{\rho})+1/2\right)}$	$\frac{1}{2}\left(\mu + \frac{1}{\rho}\right) + \frac{1}{2} = 2$
Average size vs. duration	$\langle S\|T\rangle \sim T^{\frac{1}{\sigma\nu z}}$	$\sigma\nu z = \frac{1}{2}$
Average max velocity vs. duration	$\langle v_m\|T\rangle \sim T^{\frac{\rho}{\nu z}}$	$\frac{\rho}{\nu z} = \frac{\alpha-1}{\mu-1} = 1$
Average max energy ($E_m \equiv v_m^2$) vs. duration	$\langle E_m\|T\rangle \sim T^{\frac{2\rho}{\nu z}}$	$2\frac{\rho}{\nu z} = 2\frac{\alpha-1}{\mu-1} = 2$
Average max velocity vs. size	$\langle v_m\|S\rangle \sim S^{\sigma\rho}$	$\sigma\rho = \frac{\tau-1}{\mu-1} = \frac{1}{2}$
Average max energy ($E_m \equiv v_m^2$) vs. size	$\langle E_m\|S\rangle \sim S^{2\sigma\rho}$	$2\sigma\rho = 2\frac{\tau-1}{\mu-1} = 1$

Table 5.1: Summary table of the mean-field theory (MFT) exponents and scaling relationships for avalanches statistics in slowly-driven (the driving rate $\tilde{c} \to 0$) interfaces near depinning. The first four lines give the power law and cutoff exponents for for the size S, duration T, maximum velocity v_m and maximum energy $E_m \equiv v_m^2$ observables. The script letters denote universal scaling functions. The first three distributions are shown exactly in Eqs. (4.52), (4.50), and (5.40) and the fourth follows from a simple change of variables. The parameter k gives the distance to criticality for the system; in Barkhausen noise experiments, it represents the demagnetizing field while in steady-state plasticity scenarios (including earthquakes) it is proportional to the stiffness of the coupling between the system and the driving. In the stress-controlled situation, k can be replaced by $\Sigma_c - \Sigma$, where Σ is the external stress and Σ_c is the critical stress, and the exponent predictions will remain the same. The second four lines give stress-integrated exponents and the exponents are the expected outcome of plasticity experiments where the external force or stress is increased gradually until failure and avalanches occur along the way. (See Section C.3 for notes on stress-integrated distributions and derivations). The last five lines give how the size, maximum velocity and maximum energy of an avalanche scale with its duration, and then how the maximum velocity and energy scale with the size. The first is well-known [2, 88, 72, 89] and the last four can be obtained by taking the averages of Eqs. (5.12) and (5.31).

Normalizing with a small velocity cutoff $v_m^* \sim \sqrt{2DS^*}$, the distribution is

$$P(v_m) = \frac{v_m^*}{v_m^2}\left(\frac{\left(\frac{kv_m}{2D}\right)}{\sinh\left(\frac{kv_m}{2D}\right)}\right)^2, \tag{5.40}$$

which is valid for $v_m \gg v_m^*$. In Fig. 5.3b, we confirm Eq. (5.40) numerically.

5.5 Conclusions

We have calculated exact scaling functions and exponents for the maximum avalanche velocity statistics in a mean field approximation of interface depinning. The distribution of maximum events in avalanches of fixed duration has a robust scaling form with a scaling function that depends on the driving rate, while the distribution for fixed avalanche sizes is independent of the elastic coupling constant in the adiabatic limit. The statistics of maximum velocities in arbitrary avalanches follows by integrating the maximum value distribution for fixed avalanche size or duration against the size or duration distribution. We find that the distribution of peak velocities in a train of non-overlapping avalanches has a scaling regime with power-law exponent $\mu = 2 - \tilde{c}$ followed by cut-off regime for $v_m > D/k$. Although the mean field theory captures very well the universal statistical properties of avalanches, i.e., the size, duration, and maximum value of plastic slip avalanches, it still remains an open problem as to what extent it can also describe other statistical quantities, such as velocity fluctuations during plastic deformations. For instance, discrete dislocation simulations report that the individual dislocation velocity probability distribution follows a power law with exponent ~ -2.5 [9], whereas Eq. (3.11) from mean field theory predicts an exponent of -1 for the collective velocity distribution.

Based on our calculations, we expect the $v_m^{-\mu}$ power law scaling of the maximum velocity distribution to be a very robust experimental observable, even in the case of poor time resolution where the true maximum might be missed. In fact, even if all an experiment could accomplish was to measure a random velocity within each avalanche, the inverse squared power law prediction does not change. This can be seen by a simple scaling argument. Namely, Eq. (5.12) predicts that the average value of the maximum velocity scales linearly with the avalanche duration as $\langle v_m|T\rangle \sim T$, thus, in the same way as the average velocity $\langle v|T\rangle = \langle S|T\rangle/T \sim T$. Since the maximum does not outpace the average as the avalanches get larger, we expect the same power-law behavior for the distribution regardless of whether we sample the maximum or a random point in the avalanche signal. This implies that even if the maxima are taken from a low-resolution time series, one should see an inverse squared power law distribution in the limit of slow driving, and this may make the maximum velocity easier to work with than the duration in low-resolution experiments. The scaling $\langle v_m|S\rangle \sim S^{1/2}$ should show similar independence from how well v_m is able to be measured.

However, one thing that can affect the exponent substantially is the driving rate, which must be slow in order to see $\mu = 2$. In fact the variability in the acoustic emission experiments [51, 52, 9, 25, 26, 53] on the value of μ might be related to the fact that the experiments are performed at nonzero driving rate. If that is the case, we find that the deviation from the adiabatic driving rate enters in the mean field exponents as $\mu = 2 - \tilde{c}$, in a way similar to that for the driving-rate dependent scaling exponents α and τ in the power-law distributions of avalanche durations and sizes. Experiments where the power law exponent is studied as a function of applied shear rate could test this.

In Table 5.1, we summarize the quasistatic mean field theory results for the scaling functions and exponents, incorporating the new results for the maximum avalanche velocity. However, it should be stressed that these cutoff exponents have not been observed in all cases in experiments and simulations with long-ranged forces, even when the power law scaling exponents are mean field. In Ref. [88], it is argued that in the case when the cutoff is caused by a demagnetizing field coupled *globally*, with $\partial_t u = -k \int u(t,x) d^2x$, instead of the local coupling $\partial_t u = -ku(x,t)$, the cutoff exponents are different from the mean field predictions in a way that follows from dimensional analysis and is consistent with Barkhausen noise experiments and long-range simulations. In our case it would change the maximum velocity cutoff exponent from $\rho = 1$ to $\rho_k = \frac{1}{3}$. The effects cancel out and do not alter the exponent products that appear in the last three rows of Table 5.1. In other cases [12], deviation of the cutoff exponents from the mean field values may be caused by hardening, an effect not accounted for by our considerations.

Chapter 6

Avalanche statistics of thermally activated motion near the critical stress

6.1 Creep and thermal rounding

The simple model of Chapter 2 can be straightforwardly modified to include finite temperature effects. At zero temperature, a cell is triggered to fail when its local stress exceeds a threshold. Temperature will cause local fluctuations that cause cells to trigger early with some probability. Phenomenologically, we expect that for a system at temperature Θ[1], this probability will take a form like

$$p \sim \exp\left(-C\frac{(\tau_f - \tau)^\gamma}{\Theta}\right) \tag{6.1}$$

where τ_f is the failure stress of the cell, τ is the local stress, γ is an exponent that characterizes how the energy barrier the cell faces scales with the local stress, and C is a positive constant.

The addition of temperature complicates the depinning transition. Recall that at zero temperature the average velocity v of the system is zero for s Σ below the critical stress Σ_c, and just above the critical stress, $v \sim (\Sigma - \Sigma_c)^\beta$ where $\beta = 1$ in mean field theory. In the presence of temperature, there will be a nonzero average velocity for arbitrarily low external stresses, since the system will move forward via thermal activation. For external stresses much smaller than the critical stress, the motion will become very slow. This is called the *creep* regime. In this regime, the velocity follows the form expected from a barrier scaling argument [101, 102],

$$v(\Sigma, \Theta) \sim \exp\left(-C'\frac{\Sigma^{-\mu'}}{\Theta}\right) \tag{6.2}$$

where C' and μ' are constants related to the scaling of the energy barriers at low temperatures.

Since there is nonzero velocity for all external stresses, the depinning transition is no longer sharp (see Fig, 6.1). The regime where the stress is close to the critical stress is called the *thermal rounding*, or *creep*

---

[1] We use Θ instead of T to denote temperature to avoid confusion with the avalanche duration.

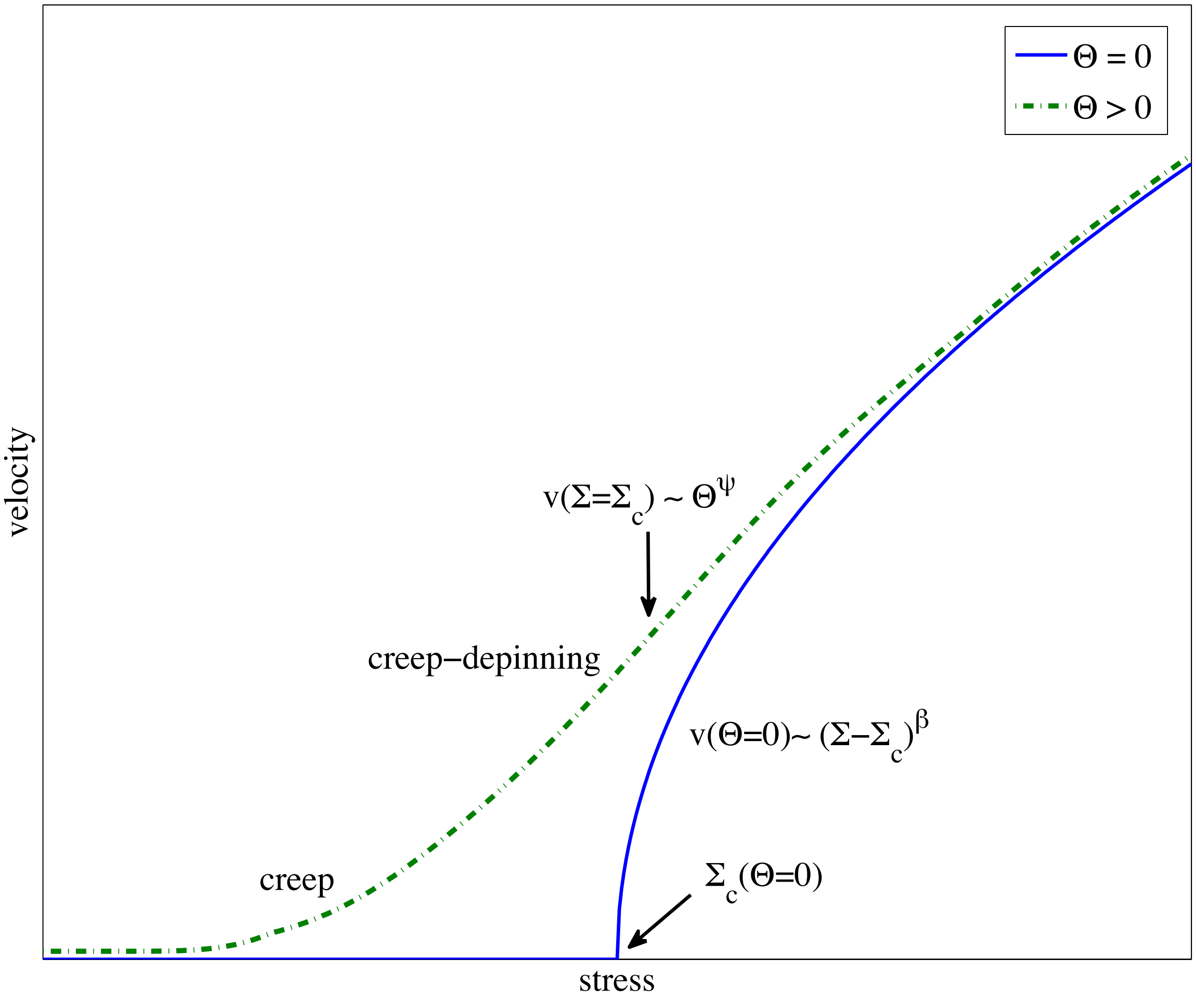

Figure 6.1: Schematic plot of the average velocity vs stress. When the temperature Θ is zero, the velocity becomes nonzero when the stress Σ reaches the zero-temperature critical value Σ_c. When Θ is small, but nonzero, the transition is rounded and the velocity is nonzero for all values of Σ, although there is a precipitous increase to a value $v \sim T^\psi$ near the zero-temperature critical stress.

depinning regime. When the stress is exactly critical, the velocity increases as a power law in temperature:

$$v(\Sigma = \Sigma_c, \Theta) \sim \Theta^\psi \tag{6.3}$$

where ψ is a critical exponent called the thermal rounding exponent. This is a new exponent and it fully characterizes the statistical behavior of the system near the critical stress and at low temperature.

6.2 Scaling theory near the critical stress

At the critical stress Σ_c and at zero temperature, the system will be at rest in a metastable configuration. If we increase the stress slightly, or increase the temperature, it will transition to a moving state. We from zero-temperature depinning that the velocity v has power law behavior $v \sim (\Sigma - \Sigma_c)^\beta$ as the stress is increased; we expect similar power law behavior $v \sim \Theta^\psi$ as the temperature is increased. The question is how β and ψ are related. We adapt an argument originally used by Middleton to describe the dynamics of charge density waves [103].

The effect of adding a small amount of extra stress will be to fail all of the cells that had distance to failure $\tau_f - \tau < \Sigma - \Sigma_c$ in the stable configuration at Σ_c. The effect of adding temperature will also be to (probably) fail the cells within a certain distance to failure. For a cell to be likely to fail, the energy barrier to failure must be on the order of the temperature. We expect that the energy barrier ΔE scales with the distance to failure as

$$\Delta E = (\tau_f - \tau)^\gamma \tag{6.4}$$

for some exponent γ. This γ^2 will depend on the character of the pinning stress [103]. In Section 6.4, we calculate the exponent in the next section and show that in our case of interest, $\gamma = 2$.

The cells whose energy barriers are less than order Θ are likely to fail, and these are the cells with local stresses $(\tau_f - \tau) \lesssim \Delta E^{1/\gamma} \sim \Theta^{1/\gamma}$. Since the stress causes those with $\tau_f - \tau < \Sigma - \Sigma_c$ to fail, we can see that a nonzero temperature is like having a stress above criticality with $(\Sigma - \Sigma_c) \sim \Theta^{1/\gamma}$. Thus we expect that when the stress is critical, the velocity scales with temperature like

$$v \sim \left(\Theta^{1/\gamma}\right)^\beta = \Theta^{\beta/\gamma} \tag{6.5}$$

so that the thermal rounding exponent is $\psi = \beta/\gamma$. Likewise, for $\Sigma = \Sigma_c$, as Θ is decreased to zero, we expect the correlation length to scale like $\xi \sim \Theta^{-\nu/\gamma}$, where ν is the correlation length exponent defined by $\xi \sim |\Sigma - \Sigma_c|^{-\nu}$ at zero temperature. This suggests a scaling ansatz for the correlation length for stresses near Σ_c and low temperatures:

$$\xi(\Sigma, \Theta) = \Theta^{-\nu/\gamma} \mathcal{F}\left(\frac{\Theta}{(\Sigma - \Sigma_c)^\gamma}\right) \tag{6.6}$$

where the scaling function $\mathcal{F}(x)$ goes to a nonzero constant as $x \to \infty$ and goes like $x^{\nu/\gamma}$ as $x \to 0$.

---

[2] The barrier scaling exponent that we call γ in this chapter has nothing to do with the susceptibility critical exponent commonly called γ.

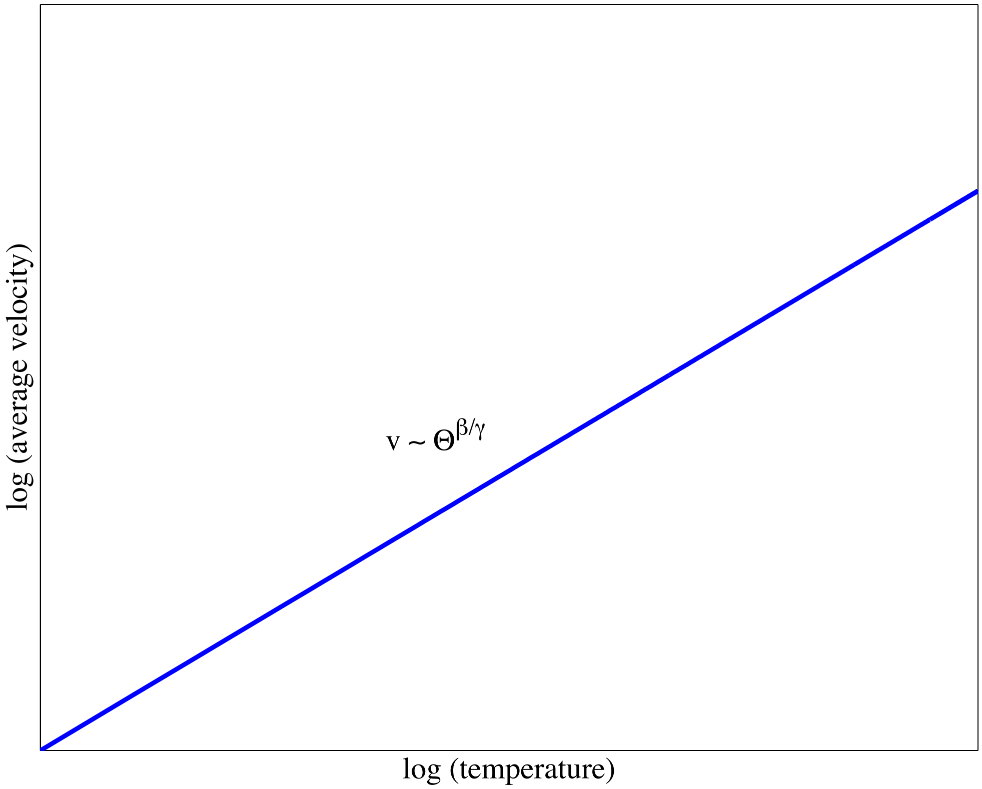

Figure 6.2: Schematic log-log plot of the average velocity v as a function of temperature Θ at the zero temperature critical stress $\Sigma = \Sigma_c$, in the scaling regime near $T = 0$. The velocity increases as a power law $v \sim \Theta^{\psi}$, where $\psi = \beta/\gamma$ is the thermal rounding exponent. In MFT, $\psi = 1/2$.

6.3 Predictions for scaling of average velocity and avalanche distributions

6.3.1 Average velocity

Above depinning at zero temperature, the average velocity scales like $v \sim (\Sigma - \Sigma_c)^{\beta} \sim \xi^{-\beta/\nu}$. Assuming the scaling dimension of the velocity remains unchanged when there is a small temperature, Eq. (6.6) implies

$$v \sim \Theta^{\beta/\gamma} \mathcal{F}\left(\frac{\Theta}{(\Sigma - \Sigma_c)^{\gamma}}\right). \tag{6.7}$$

where $\mathcal{F}(x)$ goes to a constant as $x \to 0$ and goes as $x^{-\beta/\gamma}$ as $x \to \infty$.[3] Eq. (6.7) encapsulates both the relationship $v \sim \Theta^{\beta/\nu}$ for $\Sigma = \Sigma_c$ and $v \sim (\Sigma - \Sigma_c)^{\beta}$ at $\Theta = 0$.

---

[3] For notational efficiency, in this chapter, we will use $\mathcal{F}$ (or sometimes $\overline{\mathcal{F}}$) as a generic symbol for a scaling function, with the understanding that scaling functions in different quantities refer to different (possibly related) mathematical functions, even though all are denoted by the symbol $\mathcal{F}$.

6.3.2 Avalanche size distributions

For the avalanche size distributions, we recall from Eq. (C.18) that at zero temperature, the distribution (PDF) for the size distribution is $P(S) \sim S^{-\tau}\mathcal{F}(S/S_c)$ where the avalanche size cutoff S_c diverges at the critical stress like $S_c \sim (\Sigma - \Sigma_c)^{-1/\sigma} \sim \xi^{\frac{1}{\sigma\nu}}$. Since $\xi \sim \Theta^{-\nu/\gamma}$, we therefore expect that at $\Sigma = \Sigma_c$, the avalanche cutoff will scale with temperature like $S_c \sim \Theta^{-\frac{1}{\sigma\gamma}}$. Thus, for Σ near Σ_c and Θ near zero, the size distribution $P(S; \Sigma, \Theta)$ has the scaling form

$$P(S; \Sigma, \Theta) \sim S^{-\tau}\mathcal{F}\left(S(\Sigma - \Sigma_c)^{\frac{1}{\sigma}}, S\Theta^{\frac{1}{\sigma\gamma}}\right) \tag{6.8}$$

where both arguments of the scaling function are constant at the origin and decay exponentially at infinity.

At the critical stress $\Sigma = \Sigma_c$, the size distribution scaling form reduces to $P(S; \Theta) \sim S^{-\tau}\mathcal{F}\left(S\Theta^{\frac{1}{\sigma\gamma}}\right)$. From this form we can compute the dependence of the avalanche size moments $\langle S^n\rangle$ on temperature for $\Sigma = \Sigma_c$:

$$\begin{aligned}
\langle S^n\rangle = \int S^n P(S; T)dS &= \int S^{n-\tau}\mathcal{F}\left(S\Theta^{\frac{1}{\sigma\gamma}}\right)dS \\
&= \Theta^{-\frac{n+1-\tau}{\sigma\nu}} \int z^{n-\tau}\mathcal{F}(z)dz \\
&\sim \Theta^{-\frac{n+1-\tau}{\sigma\nu}}.
\end{aligned} \tag{6.9}$$

We will also compute stress-integrated quantities (see Section C.3 for definitions and discussion). For the size, we can integrate over $f \propto \Sigma_f - \Sigma$ and get

$$\begin{aligned}
P_{\text{int}}(S; \Theta) &= S^{-\tau}\int df\mathcal{F}\left(Sf^{\frac{1}{\sigma}}, S\Theta^{\frac{1}{\sigma\gamma}}\right) \\
&= S^{-(\tau+\sigma)}\int dz\mathcal{F}\left(z^{1/\sigma}, S\Theta^{\frac{1}{\sigma\gamma}}\right) \\
&= S^{-(\tau+\sigma)}\overline{\mathcal{F}}\left(S\Theta^{\frac{1}{\sigma\gamma}}\right)
\end{aligned} \tag{6.10}$$

where we substituted $z = fS^{\sigma}$. The scaling function for the stress integrated distribution decays like e^{-S/S_c} with cutoff size that diverges at zero temperature like $S_c \sim \Theta^{-\frac{1}{\sigma\gamma}}$.

The same computation as in Eq. (6.9) gives

$$\langle S^n\rangle_{\text{int}} \sim \Theta^{-\frac{1+n-(\tau+\sigma)}{\sigma\nu}} \tag{6.11}$$

for the mean avalanche size in the stress-integrated case. Note that in MFT, $\tau + \sigma = 2$, so the exponent

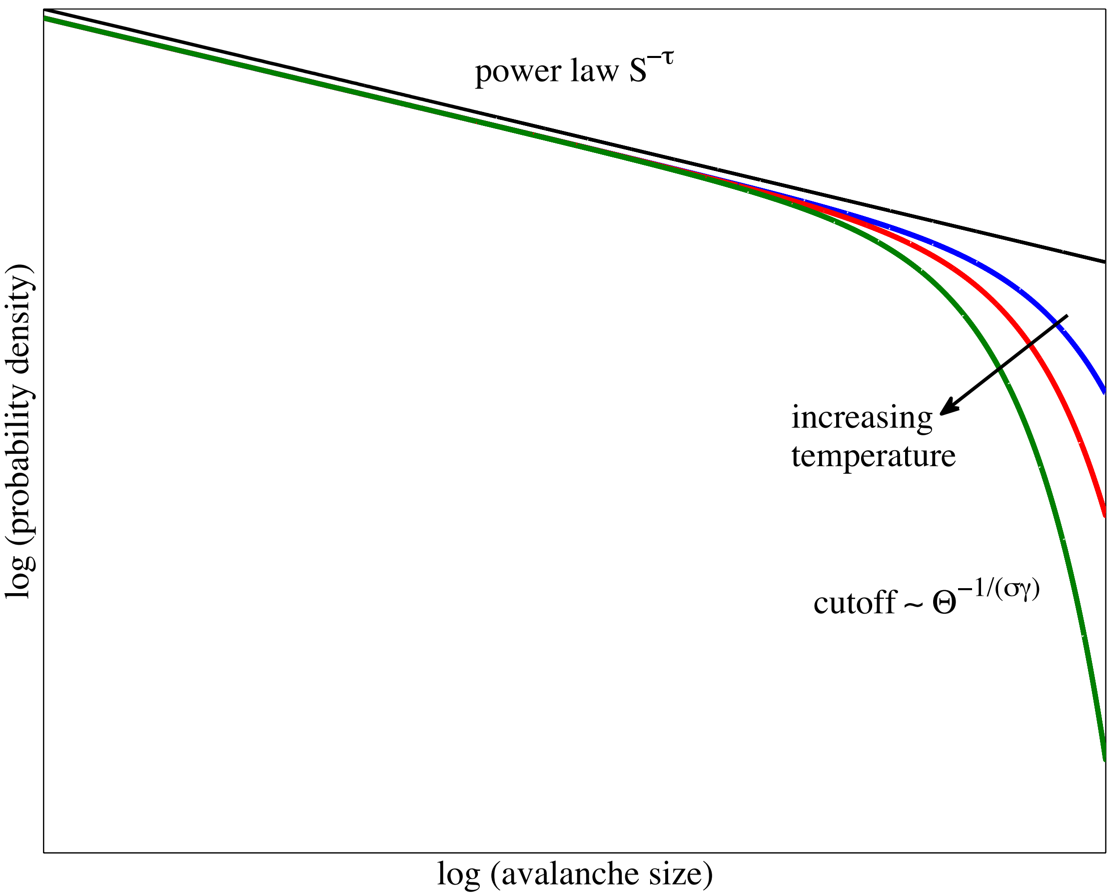

Figure 6.3: A schematic log-log plot of the avalanche size distribution PDF at different temperatures at the zero temperature critical stress $\Sigma = \Sigma_c$. The distributions scale for large avalanche size S as power laws, with a temperature-dependent cutoff $S_c \sim \Theta^{-\frac{1}{\sigma\gamma}}$ that diverges as the temperature $\Theta \to 0$. In MFT, $\sigma\gamma = 1$.

goes to zero for the first moment $n = 0$. In this case the mean avalanche size still diverges as $\Theta \to 0$, but the divergence is logarithmic.

6.3.3 Duration distributions

For the avalanche duration T, the zero temperature scaling form for the probability distribution is $P(T) \sim T^{-\alpha}\mathcal{F}(T/T_c)$ where $T_c \sim \xi^z$. The same considerations that we applied to the size distribution yield the scaling form

$$P(T;\Sigma,\Theta) \sim T^{-\alpha}\mathcal{F}\left(T(\Sigma-\Sigma_c)^{\nu z}, T\Theta^{\frac{\nu z}{\gamma}}\right) \tag{6.12}$$

for the duration distribution at nonzero temperature. The corresponding stress-integrated distribution is

$$P_{\text{int}}(T;\Theta) \sim T^{-(\alpha+\frac{1}{\nu z})}\overline{\mathcal{F}}(T\Theta^{\frac{\nu z}{\gamma}}). \tag{6.13}$$

For the average avalanche sizes, the same formal manipulations as in Eq. (6.9) give the average avalanche duration

$$\langle T \rangle \sim \Theta^{-\nu z(1+n-\alpha)} \tag{6.14}$$

at $\Sigma = \Sigma_c$ and

$$\langle T^n \rangle_{\text{int}} \sim \Theta^{-\nu z(1+n-(\alpha+\frac{1}{\nu z}))} \tag{6.15}$$

for the stress-integrated case. In MFT $\alpha = 2$, and $\nu z = 1$ so the duration moments diverge like $\Theta^{-(n-1)}$ for $\Sigma = \Sigma_c$ and $\Theta^{-(n-2)}$ in the stress-integrated case. Note that the exponents can be zero or negative for small values of n. In general, a zero exponent indicates a logarithmic divergence with Θ. If the exponent is negative, this does *not* mean that the average duration goes to zero as $\Theta \to 0$. Instead, it simply means that the average duration saturates to a non-universal constant value. For instance, we have, as $\Theta \to 0$,

$$\langle T \rangle_{\text{int}} = \int T^{-2} \mathcal{F}(T\Theta^{1/2}) dT \approx \mathcal{F}(0) \int T^{-2} dT \tag{6.16}$$

where we were allowed to make the final manipulation because the integral converges at its upper limit (the lower limit is understood to be regulated by the minimum avalanche duration). So, as the power law exponent of the distribution becomes steep, more of the lower moments of the distribution will not diverge as $\Theta \to 0$. However, higher moments of the duration distributions will exhibit divergences that could be compared with experiment.

6.3.4 Maximum velocity distributions

Based on our results established for mean field theory from Chapter 5 (see Table 5.1) we expect at zero temperature, the scaling dimension of the maximum velocity distribution is $P(v_m) \sim v_m^{-\mu} \mathcal{F}(-v_m/v_{mc})$ where $v_{mc} \sim \xi^{\rho/\nu}$. So at nonzero temperatures we have scaling forms

$$P(v_m; \Sigma, \Theta) \sim v_m^{-\mu} \mathcal{F}\left(v_m(\Sigma - \Sigma_c)^{\rho}, v_m \Theta^{\rho/\gamma}\right) \tag{6.17}$$

and

$$P_{\text{int}}(v_m; \Theta) \sim v_m^{-(\mu+\frac{1}{\rho})} \overline{\mathcal{F}}\left(v_m \Theta^{\rho/\gamma}\right). \tag{6.18}$$

The average value of the maximum velocity diverges as $\Theta \to 0$ like

$$\langle v_m^n \rangle \sim \Theta^{-\frac{\rho(1+n-\mu)}{\gamma}} \tag{6.19}$$

Quantity	Definition	MFT values
velocity vs temperature (at $\Sigma = \Sigma_c$)	$v \sim \Theta^{\psi}$	$\psi = \beta/\gamma = 1/2$
avalanche size distribution (at $\Sigma = \Sigma_c$)	$P(S) \sim S^{-\tau} \mathcal{F}\left(S\Theta^{\frac{1}{\sigma\gamma}}\right)$	$\tau = 3/2,\ \frac{1}{\sigma\gamma} = 1$
avalanche size distribution (stress-integrated)	$P(S) \sim S^{-(\tau+\sigma)} \mathcal{F}\left(S\Theta^{\frac{1}{\sigma\gamma}}\right)$	$\tau + \sigma = 2,\ \frac{1}{\sigma\gamma} = 1$
size moment vs temperature (at $\Sigma = \Sigma_c$)	$\langle S^n \rangle \sim \Theta^{-\frac{1+n-\tau}{\sigma\gamma}}$	$\frac{1+n-\tau}{\sigma\gamma} = n - \frac{1}{2}$
size moment vs temperature (stress-integrated)	$\langle S^n \rangle_{\text{int}} \sim \Theta^{-\frac{1+n-(\tau+\sigma)}{\sigma\gamma}}$	$\frac{1+n-(\tau+\sigma)}{\sigma\gamma} = n - 1$
avalanche duration distribution (at $\Sigma = \Sigma_c$)	$P(T) \sim T^{-\alpha} \mathcal{F}\left(T\Theta^{\frac{\nu z}{\gamma}}\right)$	$\alpha = 2,\ \frac{\nu z}{\gamma} = 1/2$
avalanche duration distribution (stress-integrated)	$P(T) \sim T^{-(\alpha+\frac{1}{\nu z})} \mathcal{F}\left(T\Theta^{\frac{\nu z}{\gamma}}\right)$	$\alpha + \frac{1}{\nu z} = 3,\ \frac{\nu z}{\gamma} = 1/2$
duration moment vs temperature (at $\Sigma = \Sigma_c$)	$\langle T^n \rangle \sim \Theta^{-\frac{(1+n-\alpha)\nu z}{\gamma}}$	$\frac{(1+n-\alpha)\nu z}{\gamma} = \frac{n-1}{2}$
duration moment vs temperature (stress-integrated)	$\langle T^n \rangle \sim \Theta^{-\frac{\left(1+n-(\alpha+\frac{1}{\nu z})\right)\nu z}{\gamma}}$	$\frac{\left(1+n-(\alpha+\frac{1}{\nu z})\right)\nu z}{\gamma} = \frac{n-2}{2}$
avalanche max velocity distribution (at $\Sigma = \Sigma_c$)	$P(v_m) \sim v_m^{-\mu} \mathcal{F}\left(T\Theta^{\frac{\rho}{\gamma}}\right)$	$\mu = 2,\ \frac{\rho}{\gamma} = 1/2$
avalanche max velocity distribution (stress-integrated)	$P(T) \sim v_m^{-(\mu+\frac{1}{\rho})} \mathcal{F}\left(T\Theta^{\frac{\rho}{\gamma}}\right)$	$\mu + \frac{1}{\rho} = 3,\ \frac{\rho}{\gamma} = 1/2$
max vel moment vs temperature (at $\Sigma = \Sigma_c$)	$\langle v_m^n \rangle \sim \Theta^{-\frac{\rho(1+n-\mu)}{\gamma}}$	$\frac{\rho(1+n-\mu)}{\gamma} = \frac{n-1}{2}$
max vel moment vs temperature (stress-integrated)	$\langle v_m^n \rangle \sim \Theta^{-\frac{\rho\left(1+n-(\mu+\frac{1}{\rho})\right)}{\gamma}}$	$\frac{\rho\left(1+n-(\mu+\frac{1}{\rho})\right)}{\gamma} = \frac{n-2}{2}$

Table 6.1: Table of observables for creep experiments near the critical point stress $\Sigma = \Sigma_c$ and temperature $\Theta = 0$.. Values for the exponents describing how the moments diverge when $\Theta \to 0$ are only valid when they are positive. A negative value indicates a moment that does not diverge as $\Theta \to 0$ while a zero moment indicates a logarithmic divergence.

and in the stress-integrated case

$$\langle v_m^m \rangle_{\text{int}} \sim \Theta^{-\frac{\rho(1+n-(\mu+\frac{1}{\rho}))}{\gamma}} \tag{6.20}$$

Also, like the duration, in MFT the average maximum velocity in the stress-integrated case does not diverge as $\Theta \to 0$, so we omit it from Table 6.1 with the understanding that the higher moments have interesting divergences that can be easily computed.

6.4 Derivation of the barrier scaling exponent

The thermal exponents depend on how the cell energy barriers scale with the stresses. This in turn depends on the shape of the pinning potential. In our model, the cells immediately move to the next pinning site once the local stress exceeds the threshold. This can be modeled by a pinning potential with a linear cusp. We will also assume that the potential is convex near the cusp and that the second derivative from the left-hand side of the cusp is nonzero.

If x is the cell's position along its direction of motion, we can write the pinning potential for the particle as $U(x) = U_p(x) - \tau x$ where U_p is the pinning potential and τ is the stress on the cell. . At the moment the cell is ejected from the pinning site, the potential is flat on the left-hand side of the cusp. This means the

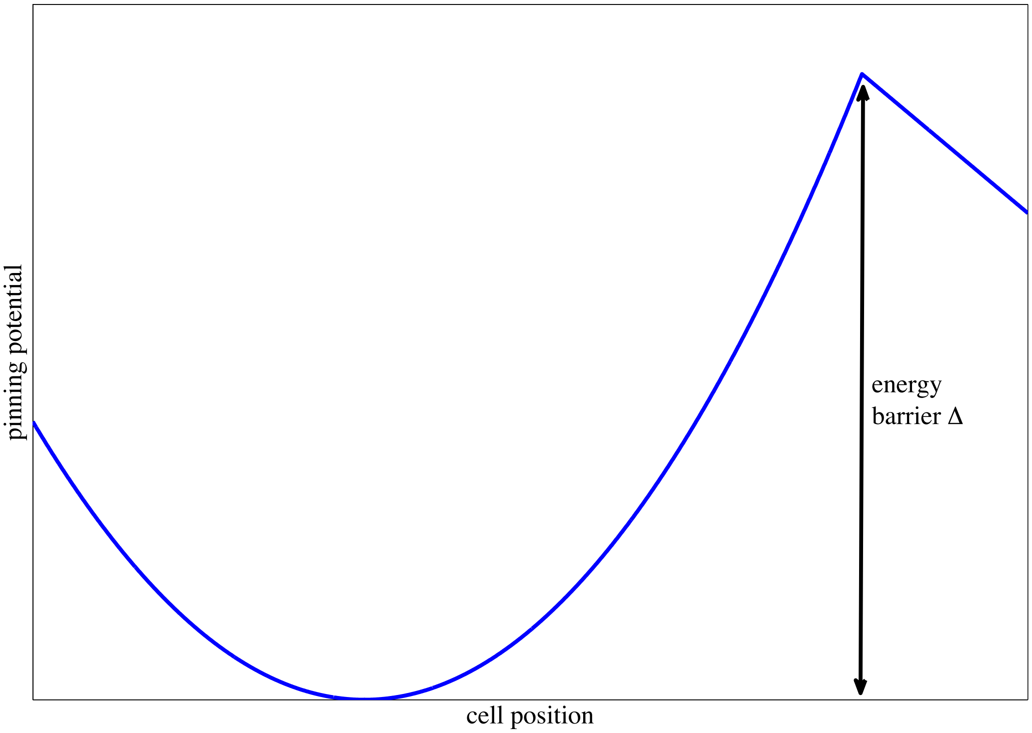

Figure 6.4: A picture of the cusped pinning potential. The cusp ensures that motion starts immediately once the cell is over the barrier [58] and thus resembles our assumption of dynamics where the cell slips once $\tau \geq \tau_f$. The height of the energy barrier scales like $\Delta \sim (\tau_f - \tau)^2$, as shown in Eq. (6.22)

failure stress is given by $\tau_f = U_p'(a^-)$ where a is the location of the cusp. If expand near the failure stress $\tau = \tau_f - \delta\tau$, we have $U(x) = U_p(x) - U_p'(a^-)x + \delta\tau x$. If the pinning potential is convex near the cusp, the location of the minimum of U will approach the cusp as $\tau \to \tau_c$. Then we can expand the pinning potential $U_p(x) \approx U_p(0) - U_p'(a^-)(a-x) + \frac{1}{2}U_p''(a^-)(a-x)^2$ so that

$$U(x) \approx U_p(a) - U_p'(a^-)a + \delta\tau x + \frac{1}{2}U_p''(a^-)(a-x)^2 \tag{6.21}$$

which has a minimum at $x_m = a - \delta\tau / U_p''(a^-)$. The the energy barrier can be calculated to be

$$\Delta = U(a) - U(x_m) = \frac{\delta\tau^2}{2U_p''(a^-)} \sim (\tau_f - \tau)^2. \tag{6.22}$$

This result depends on our assumptions about the shape of the potential well, both the strong assumptions of a linear cusp and convexity and the more generic assumption of a non-vanishing second derivative. If the pinning potential is smooth with a rounded barrier instead, then we can expand the pinning potential about x_i, the inflection point separating the minimum the particle rests in from the top of the barrier. As $\tau \to \tau_f$, the minimum and maximum will come close together, so the expansion

$$U(x) \approx \frac{1}{6}U_p'''(x_i)x^3 + \delta\tau x + U_p(x_i) \tag{6.23}$$

where again $\delta\tau = \tau_f - \tau$ is accurate near τ_f (note that $U_p'''(x_i)$ is negative). The minimum/maximum are at $x_m = \mp(-2\delta\tau/U_p'''(x_i))^{1/2}$ and the barrier is

$$\Delta = U_p(x_m) - U_p(-x_m) = 2\left(\frac{2}{-U_p'''(x_i)}\right)^{1/2} \delta\tau^{3/2} \sim (\tau_f - \tau)^{3/2} \tag{6.24}$$

which leads to different scaling of avalanche size with temperature.

Chapter 7

Analyzing low-resolution data

7.1 Introduction

The avalanches that comprise plastic deformation take place on short timescales (on the order of milliseconds in BMGs and microseconds in single crystals), so experimental time resolution is important. In this chapter we demonstrate the effect of insufficient resolution on typical avalanche observables and propose methods to diagnose and mitigate problems due to resolution. We use a simple model for demonstration and to make certain calculations explicit, but many of the results are generic. We find that naive analysis of low-resolution data can lead to avalanche size distributions with incorrect power law exponents and even no power-law regime at all. We also show that, with the traditional methods, an apparent data collapse with incorrect exponents can be obtained. More importantly, we introduce improved analysis methods that circumvent these problems. We then apply these analysis methods to downsampled high-resolution experimental data on compressed bulk metallic glasses (BMGs) and find good agreement with results previously obtained at high resolution [14] and with the predictions of a simple mean field model. The results of this study resolve an apparent discrepancy between the results from experiments at different time resolutions reported in the literature.

While it is difficult to extract reliable avalanche duration statistics when the sampling rate is lower than the inverse duration of typical avalanches, we show that avalanche size statistics can be measured for much lower resolutions than is possible for durations. The timescale that determines the required sampling rate for measuring the size statistics is given by the avalanche nucleation rate, which is the number of avalanches triggered per second during the deformation. We find that in the experimental data from [14], the size distribution changes from a broad power law (at a data acquisition rate of 100 kHz) to a peaked distribution once the resolution is lowered to around 50 Hz, a minimum required resolution for this experiment (see bottom of Fig. 7.10). Since the nucleation rate is proportional to the experimental displacement rate and proportional to the system size (see section 7.3 below), the required time resolution will be less for slower driving and smaller systems. *Therefore, if an experiment's resolution is too low and increasing the resolution* *is not feasible, then reducing the displacement rate or the system size can compensate equally well.*

In this chapter, we focus on stress drop avalanches that occur in experiment at fixed displacement rates. We propose the following:

1. When the sampling rate is higher than the nucleation rate, but lower than the rate of stress increase between avalanches (in units of the size of a typical stress drop), small stress drops can be missed (see Fig. 7.3). If the rate r of stress increase between avalanches can be estimated, then instead of defining avalanches as continuous stress drops, one should define them whenever the measured rate of stress increase decreases below r. This can be implemented by defining a *tilted* stress-time curve and measuring stress drops relative to that. The tilted curve is given by $F(t) - rt$ where r is the rate of elastic stress increase (see Eq. (7.11) and Fig. 7.5). Under ideal circumstances, avalanche sizes can be recovered with good accuracy using this method (details are given in section 7.6.2). In section 7.6.1, we give a method for determining when a stress-time signal is in this regime. The analysis also reveals a novel way to extract the avalanche size power law scaling exponent τ by downsampling data without actually measuring avalanche sizes (see Eq. (7.9)).

2. When the data acquisition rate is slightly lower than the nucleation rate, several avalanches can occur per sampling time. Furthermore, when distinct avalanches happen during successive samples, they will be part of one continuous drop in the low-resolution stress-time signal (see the inset of Fig. 7.6). For this reason, the stress drops that occur between successive samples will be more representative of the underlying avalanche sizes than the (potentially much larger) consecutive stress drops of the traditional avalanche definition, which potentially involves many time steps (see Fig. 7.6). Therefore at these very low resolutions, one should again tilt the signal by subtracting rt and take the stress drops between two successive stress measurements as the best approximation of the avalanche sizes. This will not recover the true size distribution exactly, but the result will be similar to it as long as the data acquisition rate is on the order of the nucleation rate. In section 7.6.3, we give details and show the expected corrections to the size distribution.

In section 7.7.1, we show that these procedures can be used to obtain a scaling collapse from the low-resolution data with the same critical exponents as one would find at high resolution. We also show that traditional analysis of low resolution simulation data from the simple mean field model (of Ref. [20]) at different spring stiffnesses can give a collapse with incorrect exponents (see Fig. 7.9). In section 7.8, we[1] compare the results to downsampled experimental BMG compression data and find good agreement with model predictions.

---

[1] The experimental data presented in this chapter was provided by Wendy Wright and analyzed by Aya Nawano

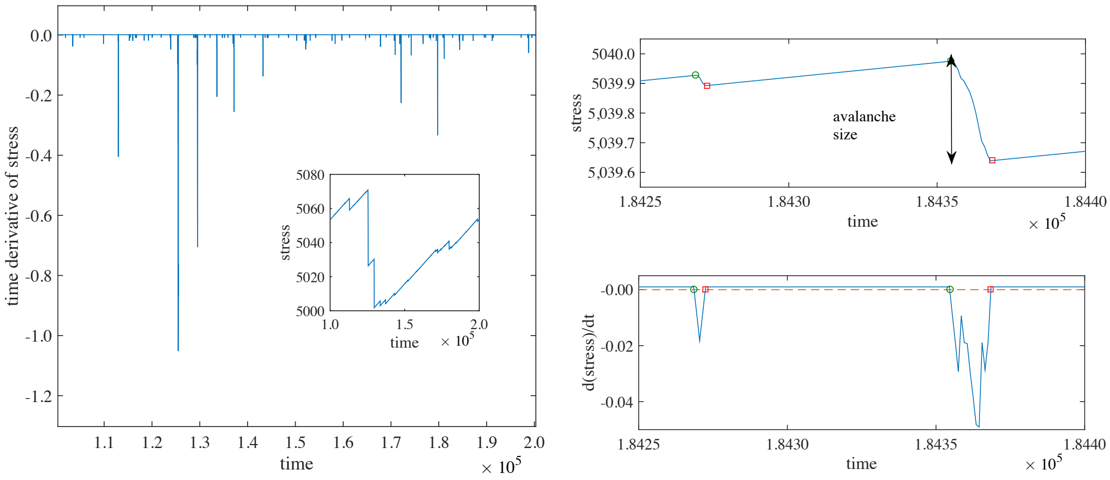

Figure 7.1: (left) The time derivative stress vs time series for a typical section of simulation signal from the simple mean field model (from Ref. [20]). The inset shows the stress vs time curve. (right) A demonstration of what we call the "traditional" avalanche detection procedure. The top figure is a stress-time curve with two avalanches and the bottom is its time derivative. The avalanches are detected when the time derivative drops below a threshold (the dashed line in the bottom figure). The circles and squares indicate the starts and ends of the avalanches, respectively. The avalanche size is the total decrease in stress, as indicated on the top figure.

7.2 Extracting avalanche statistics from experimental signals

Experimental data on plasticity generally comes in one of two flavors: stress versus time (at constant displacement rate) or displacement versus time (at a constant rate of stress increase). In the first case, an avalanche manifests as a sudden drop in stress and in between the avalanches are "quiet periods" during which the stress increases at a constant rate due to elastic loading. In the second case the avalanches are jumps in the displacement and there is little change in displacement during the quiet periods. As mentioned above, in this chapter, we focus on analyzing stress versus time data at a fixed imposed displacement rate, although the results can be adapted straightforwardly to displacement versus time data.

Traditionally, avalanches are detected by taking a derivative of the signal and observing when it drops below a negative threshold. For instance, a stress drop avalanche begins when the derivative of the stress becomes negative and ends when it returns to being positive (shown in Fig. 7.1). We call this the *traditional (or naive/conventional) method*, in contrast to methods we develop in Sections 7.6.2 and 7.6.3 that are more appropriate for low-resolution data.

In practice, experimental noise has a large effect on the numerical derivative of a signal, so naive application of this method can be unreliable, especially at high sampling rates. This problem can be addressed by optimally filtering the input data [14], by demanding that the stress derivative drops below some negative threshold (rather than a threshold of zero), or by dismissing avalanches below a certain size as indistinguishable from noise. Deciding on the appropriate method requires care because noise can not only cause spurious avalanches to be detected, but can also cause avalanches to be incorrectly broken into pieces.

Once the avalanche sizes and durations have been measured, estimates of the statistical distributions of these quantities can be constructed. The traditional way to present a distribution estimate is using a normalized histogram of the sizes and durations as an approximate probability density function (PDF). Histograms can be very effective when data takes integer values or when many avalanches have been collected. When the data values span several orders of magnitude (as avalanche sizes and durations often do), logarithmic binning can be effective for reducing noise in the tail of the distribution. However any histogramming procedure introduces a new parameter (binning scale) and also, more crucially, averages out information from the data.

For this reason, we prefer to use complementary cumulative distributions (CCDFs), even though their visual interpretation is not always as straightforward as it is for PDFs. The CCDF for a random variable X is defined as $C(x) = P(X > x)$. It can be estimated from the data straightforwardly as $\hat{C}(x) = \{\text{fraction of samples with value greater than x}\}$. Furthermore, for independent samples, none of the information is lost from the data: each "step" in the CCDF estimate is at the location of a data point, so the entire data set can be recovered (up to an ordering of the samples).

Key predictions of avalanche models about scaling forms of size and duration PDFs can be cast equally well in terms of the CCDF [11, 14].

7.3 Model

We use the simple mean field model described in Section 2 with an array of N cells that are elastically coupled to one another as well as to a driving spring that moves at a constant rate. The stress τ_i on cell i is given by

$$\tau_i = \frac{J}{N-1}\sum_{j=1}^{N}(u_j - u_i) + K(v_d t - u_i) \tag{7.1}$$

where u_i is the position of the i-th cell, J is the mean-field coupling between the cells and K is the spring constant of the loading spring connecting a site to the sample boundary that moves at speed v_d. For a system with linear size L, the system's boundary is a distance$\sim L$ away from the cells, which leads to a loading spring stiffness $K \sim 1/L$ [20]. This means that for a planar shear band with N cells, we have $K \sim 1/\sqrt{N}$ and therefore large systems have a naturally small value of K.

Summing Eq. (7.1), the total stress on the system is $F = NK(v_d t - \bar{u})$ where $\bar{u}$ is the average displacement of the cells. The instantaneous stress drop rate is

$$-\frac{\delta F}{\delta t} = -NKv_d + Kn\frac{\delta u}{\delta t} = NK(v - v_d) \tag{7.2}$$

where n is the number of cells that failed, δu is the characteristic distance a cell slips when it fails, δt is the time step, and $v = \frac{n}{N}\frac{\delta u}{\delta t}$ is the instantaneous center of mass velocity of the system. Thus the stress drop rate is proportional to the difference between the instantaneous velocity and the speed of the sample boundary. So if we measure the size of an avalanche as the total stress drop, it is proportional to $\Delta u - v_d T$ where $\Delta u = n\delta u$ is the displacement jump and T is the avalanche duration. The disproportionality $v_d T$ between stress drops and displacement jumps becomes unimportant in the quasistatic limit $v_d \to 0$ for any finite avalanche duration T.

7.4 Timescales

The two most important timescales in the problem are the maximum avalanche duration T_a and the average interevent time T_i. The smallest relevant physical timescale is the microscopic scale δt set by the speed of slip activations in the material. It is the reference timescale for the problem and serves as the simulation time step in the model.

In the limit of quasistatic driving, the maximum avalanche duration T_a scales with distance to criticality $k \equiv K/J$ as $T_a \sim \delta t k^{-\nu z}$ where $\nu = 1$ and $z = 1$ for mean field depinning with long-ranged forces [2]. The other timescales pertaining to the avalanche durations also diverge as $k \to 0$, but not necessarily with the same exponent. For instance the average avalanche duration scales like $\langle T \rangle \sim k^{-\nu z(2-\alpha)}$ where α is the power law exponent for the duration distribution. In mean field theory, $\alpha = 2$ and $\langle T \rangle \sim \log(k^{-1})$ [20, 50].

The interevent times are controlled by the displacement rate. The average interevent time is $T_i = \delta f/(Kv_d)$ where δf is the average amount of added stress required to nucleate an avalanche after the previous one ends. In the cellular model, we have $\delta f \sim \delta\tau/N$, where $\delta\tau$ is the amount a cell's stress is reduced when it slips (as defined in Section 7.3), so $T_i = \delta\tau/(NKv_d)$.

The ratio of the average interevent time and the maximum avalanche duration is an important quantity. If the interevent times are much larger than the avalanche durations, then there are no temporal overlaps between avalanches and the analysis simplifies. This condition can be obtained by driving the system at a sufficiently slow rate. Demanding that the average interevent time T_i is much longer than the maximum avalanche duration $T_a = \delta t/k^{\nu z} = \delta t(J/K)^{\nu z}$ (with $\nu z = 1$ in MFT) gives the condition

$$v_d \ll \frac{\delta\tau}{JN\delta t} \approx \frac{\delta u}{N\delta t} \tag{7.3}$$

where $\delta u \approx \delta\tau/J$ is the amount a cell slips when it is triggered, as defined in Section 7.3. We will assume that this condition holds throughout this chapter, so that avalanches are well-separated in time.

7.5 Avalanche duration distributions

If an avalanche has shorter duration than the sampling time t_s, it is impossible to measure its duration. Therefore, we can only expect our measured duration distributions to accord with theory when the sampling time is much less than the maximum avalanche duration T_a. Even avalanche durations that are on the order of the sampling time will be measured incorrectly due to quantization, so only durations that are much longer than the sampling time will be measured accurately.

Furthermore, duration distributions generally scale over fewer orders of magnitude than the size distribution since $T \sim S^{\sigma\nu z}$ where $\sigma\nu z = 1/2$ in MFT and is generically less than one. Therefore, it is unlikely that one will obtain a reliable picture of the scaling regime for the duration distribution except at sufficiently high time resolution. In our simulations we set the duration cutoff to $T_a \approx 100$ time steps and this corresponds to an average duration of around $\langle T\rangle \approx 10$. Even when we use $t_s = 5$ or even $t_s = 2$, we see an apparent deviation in the duration distribution from the power law observed at full resolution. See Fig. 7.2

7.6 Avalanche size distributions

Fortunately, avalanche sizes are much more robust to low time resolution than durations. This is not because they exhibit more decades of scaling, but rather because stress drops are measurable even if the sampling time is longer than the avalanche duration. Still, there are difficulties with the measurement process as the resolution is decreased, but fortunately some of the most common problems can be mitigated.

We will begin by studying the regime where the sampling time t_s is much less than the average interevent time T_i. The relationship between the sampling time and the maximum avalanche duration T_a is of secondary importance when studying avalanche sizes as long as $T_a \ll T_i$.

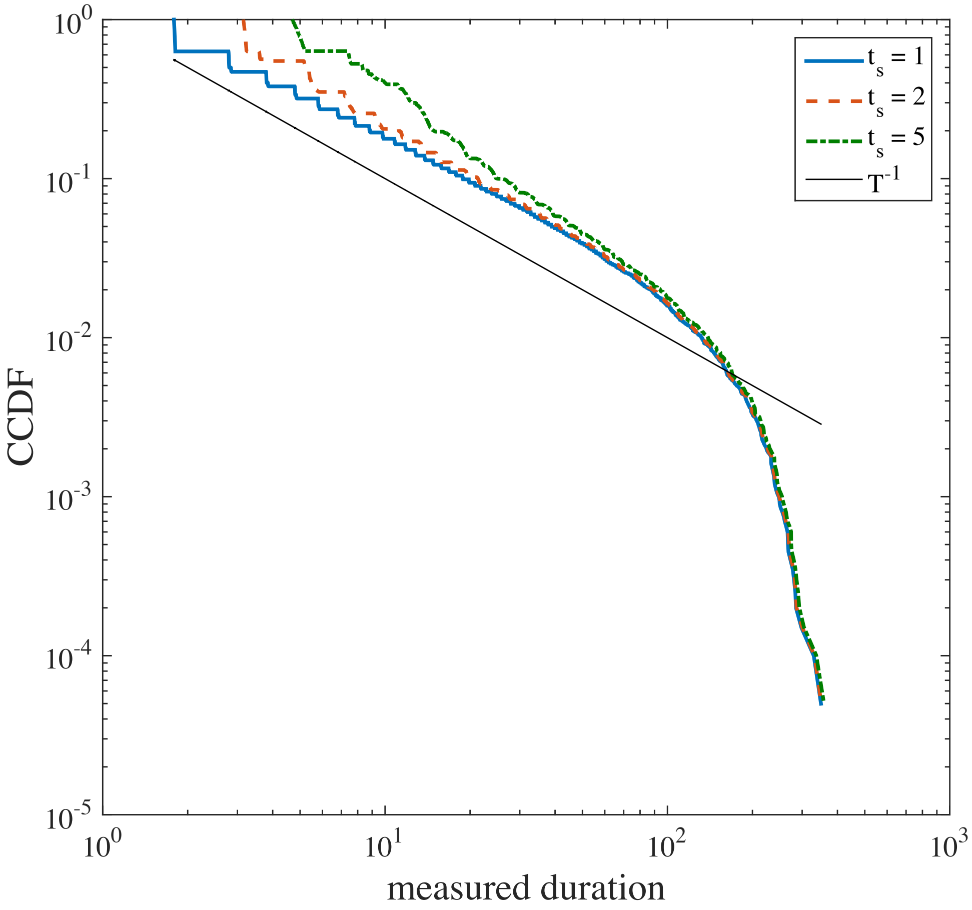

Figure 7.2: Duration distributions for several values of the sampling time t_s. The line represents the MFT prediction $C(T) \sim T^{-1}$ [20]. The apparent power law changes with sampling time t_s, even for values of t_s much less than the maximum avalanche duration $T_a \approx 100$. The simulation parameters used were number of cells $N = 10^4$, coupling between cells $J = 1$, loading spring stiffness $K = 10^{-2}$, and displacement rate $v_d = 10^{-5}$.

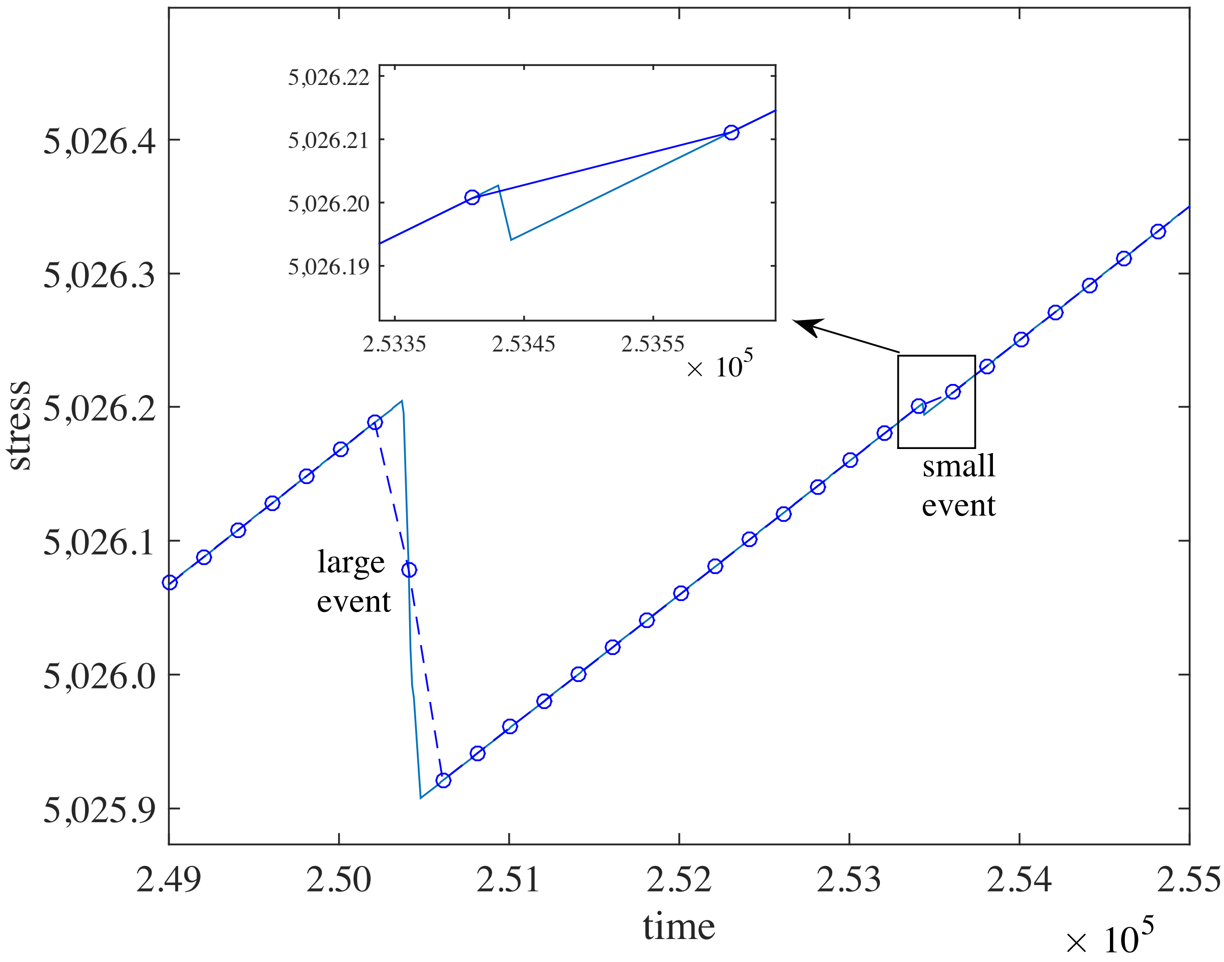

Figure 7.3: A piece of a stress-time series from a simulation of the mean field model (from Ref. [20]). The circles mark every twentieth data point and thus corresponds to a lower-resolution signal with sampling time $t_s = 20$ (in units of the simulation time step $\delta t = 1$). The size of the large event on the left side of the plot is measured fairly accurately by the size of the stress drop in the low-resolution signal. However, as the inset shows, a small stress drop does not have a corresponding drop in the low resolution signal.

7.6.1 One avalanche per timestep ($t_s \ll T_i$)

If we have sampling time $t_s \ll T_i$, then there will almost always be at most one avalanche per time sample. In this case, the size distribution of *measured* avalanches can be computed exactly. The effect of the low resolution will be that some small stress drops will be overcome by the background elastic increase in stress (see Fig. 7.3). The elastic stress increase will be $Kv_d t_s$ where t_s is the sampling time. The measured stress drop will be $S_{t_s} = \min(S - Kv_d t_s, 0)$ and the avalanches that have size less than

$$S^* = Kv_d t_s \tag{7.4}$$

go undetected by the standard methods. If we assume the avalanches are drawn from the distribution predicted by MFT [50]

$$P(S) = \frac{\sqrt{S_m}}{2S^{3/2}} e^{-k^2 S/2} \tag{7.5}$$

where $S_m \ll k^{-2}$ is the *minimum* avalanche size, then we will start to notice significant changes in the shape of the size distribution once $S^* \gtrsim S_m$. The probability that an avalanche is missed is given by

$$P(S < S^*) = \int_{S_m}^{S^*} P(S) dS = \frac{k\sqrt{S_m}}{2} \int_{k^2 S_m}^{k^2 S^*} x^{-3/2} e^{-x/2} dx \tag{7.6}$$

If the data acquisition rate is sufficiently high that the largest avalanches are detected, i.e. if $S^* \ll k^{-2}$, this works out to

$$P(S < S^*) \approx \frac{k\sqrt{S_m}}{2} \int_{k^2 S_m}^{k^2 S^*} x^{-3/2} dx = 1 - \sqrt{\frac{S_m}{S^*}}. \tag{7.7}$$

Similarly, for a more general size distribution $P(S) \sim \frac{1}{S^\tau} \mathcal{F}(S/S_a)$, where S_a is an upper size cutoff and $\mathcal{F}(x)$ is a scaling function that is regular near the origin and decays exponentially at large values, the probability an avalanche will be too small to observe is

$$P(S < S^*) \approx 1 - \left(\frac{S_m}{S^*}\right)^{\tau - 1} \tag{7.8}$$

for the case that the largest avalanches are detected, i.e. for $S^* \ll S_a$. This means that as the resolution is lowered, the number of avalanches detected N_{detected} will go down. The proportion detected $N_{\text{detected}}/N_{\text{total}}$ will be approximately $P(S > S^*) = (S_m/S^*)^{\tau-1}$. Since $S^* \sim t_s$, it follows that

$$N_{\text{detected}} \sim (t_s)^{-(\tau-1)}. \tag{7.9}$$

Interestingly, Eq. (7.9) gives us a way to estimate the correct size exponent τ without ever measuring the size of an avalanche. One can simply downsample the data to lower resolutions (that are still high enough so that large avalanches are detected), and then count the number of avalanches measured at each resolution (See Figs. 7.4 and 7.11). Eq. (7.9) also gives a potential way to diagnose whether avalanches are being lost due to low resolution or high strain rate. If one downsamples the stress-time curve and finds the number of avalanches decays initially like $t_s^{\tau-1}$, then avalanches are already being lost due to resolution. If the number of avalanches is constant at first, and then begins to decay, then the resolution is high enough that this effect is not important.

Provided that $S^* \ll S_a$, the avalanches that are above the detection threshold will come from the truncated distribution $P^*(S) = A\frac{(S^*)^{\tau-1}}{S^\tau}F(S/S_a)$ for $S > S^*$, where A is a numerical constant approximately equal to $\tau - 1$ by normalization. Additionally, the observed size of the avalanche is less than its original size by S^*. So the observed distribution will be shifted:

$$P_{obs}(S) = P^*(S + S^*) = A\frac{(S^*)^{\tau-1}}{(S + S^*)^\tau}F((S + S^*)/S_a) \tag{7.10}$$

for $S > 0$. For $S \gg S^*$ this looks like the usual power law decay with cutoff, but the distribution flattens near the origin. For moderate values of S^* the distribution appears rounded and the power law is difficult to identify by eye. (See the red curve in the bottom panel of Fig. 7.5.)

7.6.2 Recovering small avalanches for $t_s \ll T_i$ and $T_a \ll T_s$

If the rate of elastic stress increase (i.e. in the absence of avalanches) is known, then deviations from this trend will be approximately the sum of the avalanche sizes during the sampling interval. There are two potential methods for estimating the rate of elastic stress increase. If the stress signal has an elastic portion, its slope can serve as an estimate. Alternatively, as long as the sampling rate is not too low compared to the avalanche nucleation rate, there will be some time intervals where very little plastic deformation occurs that can be used for an estimate.

In the model, the stress increase rate is given by $r = KNv_d$. If we estimate r, we can tilt the stress signal $F(t)$ to

$$F(t) \to F(t) - rt, \tag{7.11}$$

and then perform the analysis (shown in Fig. 7.1) on the tilted signal (see Fig. 7.5). Then the complication of small avalanches being covered up by the stress increase during elastic loading will be removed.

For the model signal, we can nearly recover the exact avalanche distribution for $t_s \approx T_i/10 \approx T_a$. This

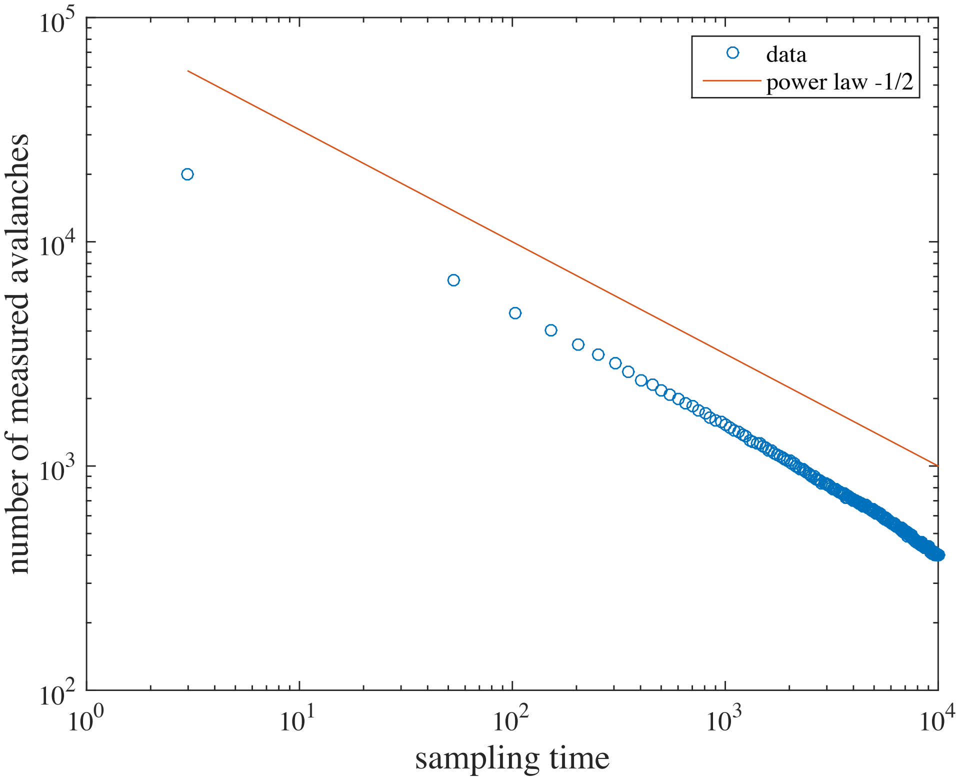

Figure 7.4: Number of avalanches collected werever sampling time (in units of the simulation time step $\delta t = 1$) from a simulation of the mean field model (from Ref. [20]). The simulation parameters used were number of cells $N = 10^4$, coupling between cells $J = 1$, loading spring stiffness $K = 10^{-2}$, and displacement rate $v_d = 10^{-5}$. The line shows the predicted power law $1 - \tau = -1/2$ from Eq. (7.9).

is possible because we are at a high enough resolution that usually, at most one avalanche happens per sampling interval and no information is lost. Whether the condition $t_s \ll T_i$ is achieved experimentally depends both on the strain rate and the time resolution. If time resolution is too low, this regime can still be reached by lowering the strain rate.

In the next section, we will discuss the situation where $t_s \approx T_i$ and there can be several avalanches per sampling interval.

7.6.3 Multiple avalanches per timestep ($t_s \gtrsim T_i$ and $T_i \gg T_a$)

When the avalanche nucleation rate is on the order of the sampling rate, we must account for the possibility of many avalanches occurring during a time sample. If we attempt to analyze the signal with the method of Fig. (7.1), two effects become important. First, the stress drop during a sampling time may be from multiple avalanches, and there is no way to know the sizes of the individual avalanches, only their sum. Second, if there are stress drops in consecutive time intervals, they will be all merged into a single avalanche (see Fig. 7.6). Therefore, the apparent avalanche will only stop once there is a time interval without any stress drop.

If the avalanches are nucleated in a Poisson process, the probability that there are no avalanches during a sampling time interval t_s is $p_0 = e^{-t_s/T_i}$ where T_i is the mean interevent time between avalanches. The measured avalanche durations will be quantized in terms of the sample time, i.e. $T = mt_s$ where m is the number of consecutive sample times during which the stress drops. Since the measured avalanche continues until there is a sampling time with no physical avalanches, the duration distribution follows the geometric distribution [67]

$$P(T = mt_s) = (1 - p_0)^{m-2} p_0 \tag{7.12}$$

where $p_0 = e^{-t_s/T_i}$ is the probability the stress does not decrease during the time step, ending the measured avalanche. (The reason $m - 2$ occurs on the right hand side rather than $m - 1$ is because the minimum avalanche duration is one rather than zero.) From the distribution defined in Eq. (7.12), we can compute the average measured duration to be

$$\langle T \rangle = \frac{t_s}{p_0} + t_s = t_s(1 + e^{t_s/T_i}). \tag{7.13}$$

Likewise the average size of an apparent avalanche will increase exponentially with sampling time. Since the physical avalanches are nucleated in a Poisson process with rate $1/T_i$, the number of physical avalanches during a sample will be Poisson distributed with average t_s/T_i. If we let n be the number of physical

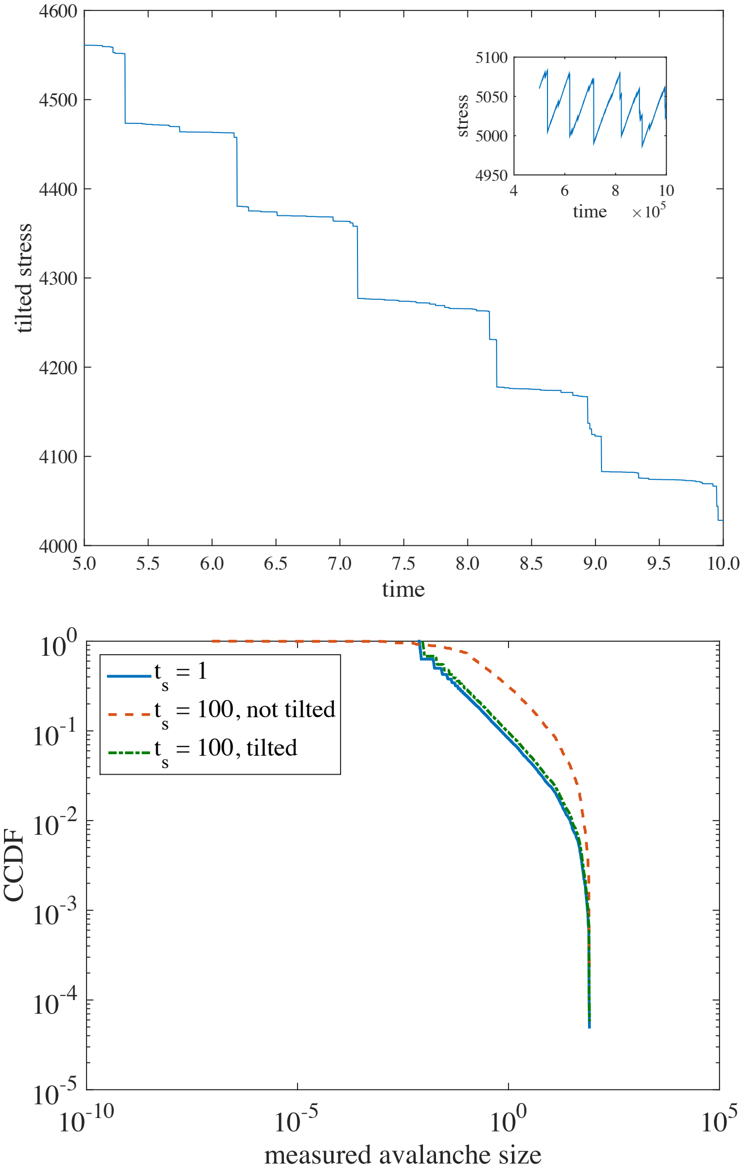

Figure 7.5: (top) A section of the tilted stress-time curve froma simulation of the mean field model (from Ref. [20]), downsampled to sampling time $t_s = 500$ in units of the simulation time step $\delta t = 1$. More small and medium-sized stress drops can be seen on the tilted signal. The inset shows the stress-time curve before tilting. (bottom) Measured avalanche size CCDFs at full resolution ($t_s = 1$) and at $t_s = 100$ (about one tenth of average interevent time T_i) for both the original and tilted stress-time series. The tilted data gives a CCDF that is very close to the one obtained at full resolution, whereas the original signal gives a distribution that appears rounded and the power law is difficult to identify by eye. The simulation parameters used were number of cells $N = 10^4$, coupling between cells $J = 1$, loading spring stiffness $K = 10^{-2}$, and displacement rate $v_d = 10^{-5}$.

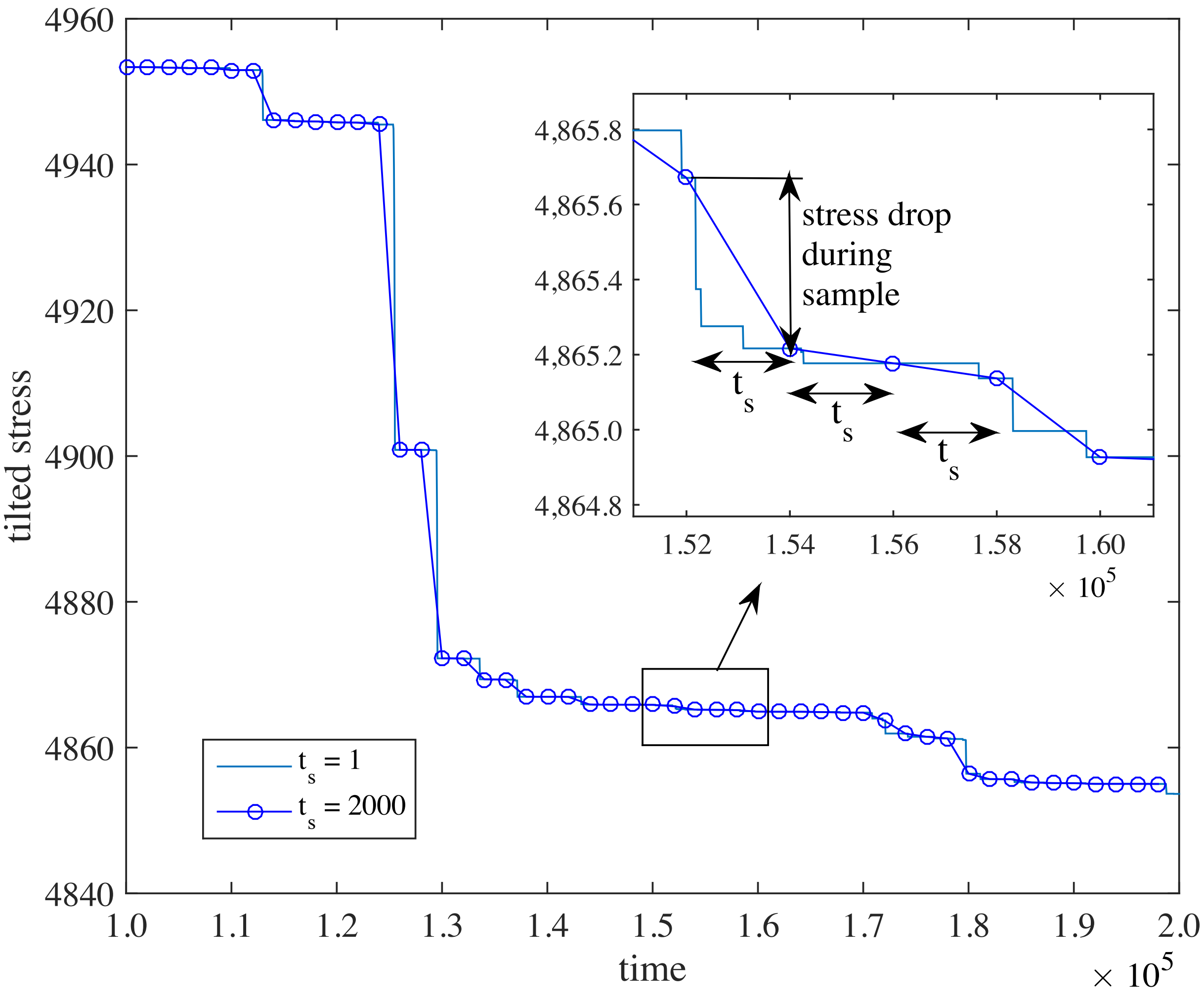

Figure 7.6: A piece of a stress-time series from a simulation of the mean field model (from Ref. [20]), tilted as described in Eq. (7.11). The circles mark every two-thousandth data point and thus corresponds to a very low resolution signal with sampling time $t_s = 2000$. This sampling time is about twice the inverse avalanche nucleation rate, so most increments contain at least one avalanche. As a result, measuring avalanches as successive drops in the tilted stress will give stress drops of very long duration, corresponding to many successive underlying avalanches. However, the stress drops measured between successive sample points will be close in size to the underlying avalanches, although sometimes several avalanches may be merged, as is the case for the first and last time step of size t_s of the inset plot. The simulation parameters used were number of cells $N = 10^4$, coupling between cells $J = 1$, loading spring stiffness $K = 10^{-2}$, and displacement rate $v_d = 10^{-5}$.

avalanches that occur during a sample time, n will have the distribution

$$P(n) = \frac{1}{e^{t_s/T_i} - 1} \frac{(t_s/T_i)^n}{n!} \tag{7.14}$$

for $n \geq 1$. We modified the Poisson distribution so to not include $n = 0$ because sampling times in which

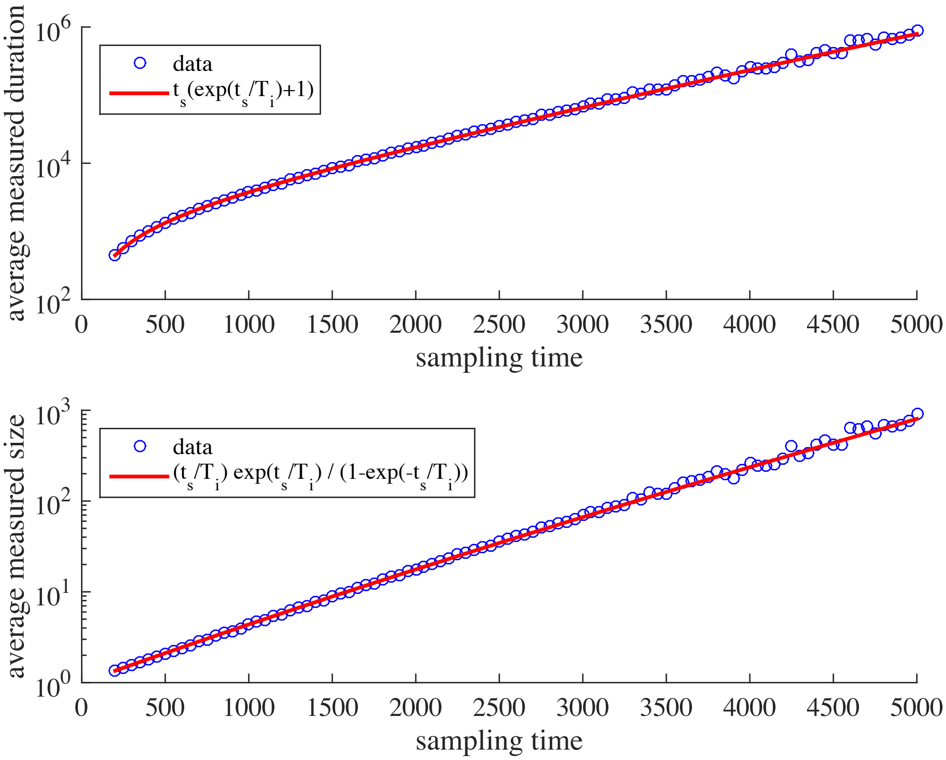

Figure 7.7: Mean values of the measured size and duration vs sampling time from the analysis (shown in Fig. 7.1) of the *tilted* signal. The curves are the predicted values from Eqs. (7.13) (top) and (7.16) (bottom).

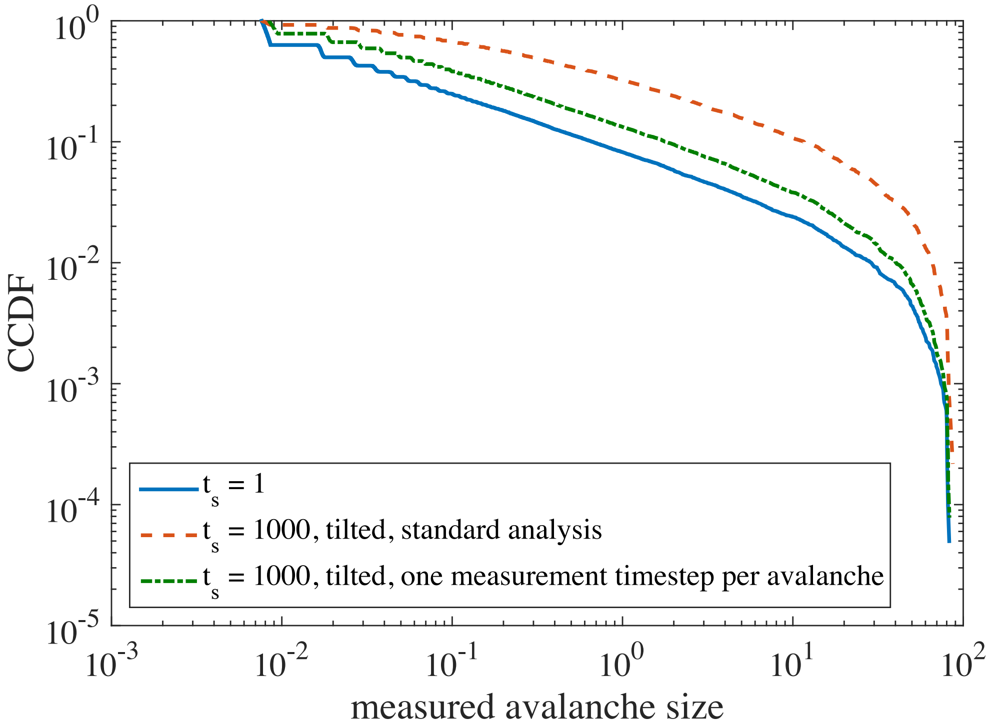

Figure 7.8: Avalanche size CCDFs from simulations of the mean field model (from Ref. [20]) at full resolution and from tilted stress-time curves at low resolution $t_s = 1000$ (roughly two times the average interevent time T_i.) using the analysis described in Fig. 7.1 and the improved method for very low resolution data described in Section 7.6.3 that defines the sample stress drops defined in Eq. (7.17) (after tilting) as avalanche sizes. The distribution from the improved method is much closer to the full resolution distribution and the same rough power law behavior can be seen, but it is still somewhat distorted due to avalanche merging. The simulation parameters used were number of cells $N = 10^4$, coupling between cells $J = 1$, loading spring stiffness $K = 10^{-2}$, and displacement rate $v_d = 10^{-5}$.

no physical avalanches happen will not show any stress decrease. Taking the average of the distribution, we get.

$$\langle n \rangle = \sum_{n=1}^{\infty} nP(n) = \frac{t_s/T_i}{1 - e^{-t_s/T_i}}. \tag{7.15}$$

The average measured avalanche size will be the average number of sample times per avalanche $\langle T \rangle / t_s$, multiplied by the average number of physical avalanches per sample time $\langle n \rangle$, times the average size of an avalanche. Putting this together:

$$\langle S \rangle = \frac{\langle T \rangle}{t_s} \langle n \rangle \langle S \rangle_0 = \frac{t_s}{T_i} \frac{(1 + e^{t_s/T_i})}{(1 - e^{-t_s/T_i})} \langle S \rangle_0 \tag{7.16}$$

where $\langle S \rangle_0$ is the average size of the underlying physical avalanches. In Fig. 7.7 we show that Eqs. (7.13) and (7.16) agree with the simulation of the MFT model.

So we see that in this very low resolution regime, the analysis (shown in Fig. 7.1) gives something com-

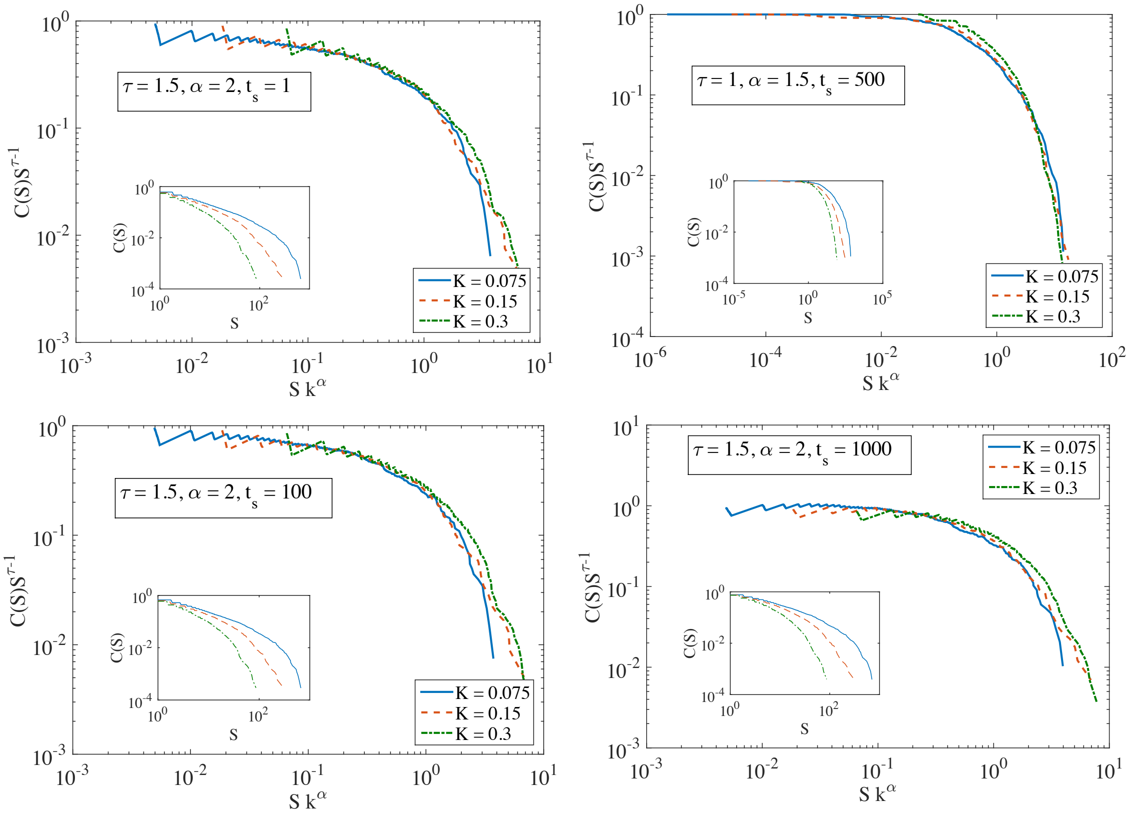

Figure 7.9: (top left) Data collapse of the size CCDF (Eq.(7.5)) for different K values from a simulation of the mean field model (from Ref. [20]) at full resolution. The collapse uses MFT exponents $\tau = 3/2$ and $\alpha = 2$ [20]. (top right) An apparent collapse for $t_s = 500$ using the analysis (shown in Fig. 7.1). Here the collapses yields incorrect exponents $\tau = 1$ and $\alpha = 1.5$. (bottom left) A collapse with MFT exponents $\tau = 3/2$ and $\alpha = 2$ for $t_s = 100 \ll T_i$, using the the tilted signal described in Section 7.6.2. (bottom right) A successful collapse with MFT exponents $\tau = 3/2$ and $\alpha = 2$ for $t_s = 1000 \approx T_i$, using the sample stress drops defined in Eq. (7.17). Insets are the original distribution before the rescaling.

pletely different from the underlying avalanche distributions. The principal complication is that consecutive intervals are likely to have stress drops. Therefore, it is more representative to measure the avalanche as the stress drop during a single sampling time. This means that if the stress changes by an amount δF during a sampling time, one should record an avalanche of size

$$S = \begin{cases} -\delta F, & \delta F < 0 \\ \text{no avalanche}, & \delta F \geq 0 \end{cases} \tag{7.17}$$

(see the inset of Fig. 7.6). We will call these the *sample stress drops* to distinguish them from the stress drop avalanches that extend over multiple time steps that are measured in the analysis.

One complication with this method is that sometimes there are several avalanches during a time step. We cannot recover the sizes of the individual avalanches, but if we know the nucleation rate, we can predict the distribution of apparent avalanche sizes as follows.

Let $P_n(S)$ be the distribution of the sum of n independent avalanches. The distribution of apparent avalanche sizes will be

$$P(S) = \sum_{n=1}^{\infty} P(n) P_n(S) \tag{7.18}$$

where $P(n)$ is the distribution of the number of avalanches in a sampling time from Eq. (7.14) and $P_n(S)$ is the distribution of the sum of n independent avalanche sizes. We will show in Section 7.7

$$P_n(S) = \frac{n v_0}{\sqrt{2\pi S^3}} e^{-\frac{1}{2S}(kS - n v_0)^2}, \tag{7.19}$$

where $v_0 = S_m/\delta t$, the ratio of the minimum physical avalanche size to the minimum physical avalanche duration. As long as $\langle n \rangle$, the average number of avalanches per sampling time, is not too big, the distribution of Eq. (7.18) looks roughly like the distribution $P(S)$ of physical avalanche sizes with a larger short-distance cutoff since the $n = 1$ term of Eq. (7.18) dominates. Provided that $\langle n \rangle \langle S \rangle_0 \ll S_a$, where $\langle S \rangle_0$ is the average physical avalanche size and S_a is the maximum physical avalanche size, the tail of the distribution is not affected by merging, so a collapse may still look reasonable. See Figs. 7.8 and 7.9.

7.7 Derivation of the merged avalanche distribution

As we showed in Section 4.5 the distribution of avalanche sizes is given by

$$P(S) = \frac{v_0}{\sqrt{2\pi S^3}} e^{-\frac{1}{2S}(kS - v_0)^2} \tag{7.20}$$

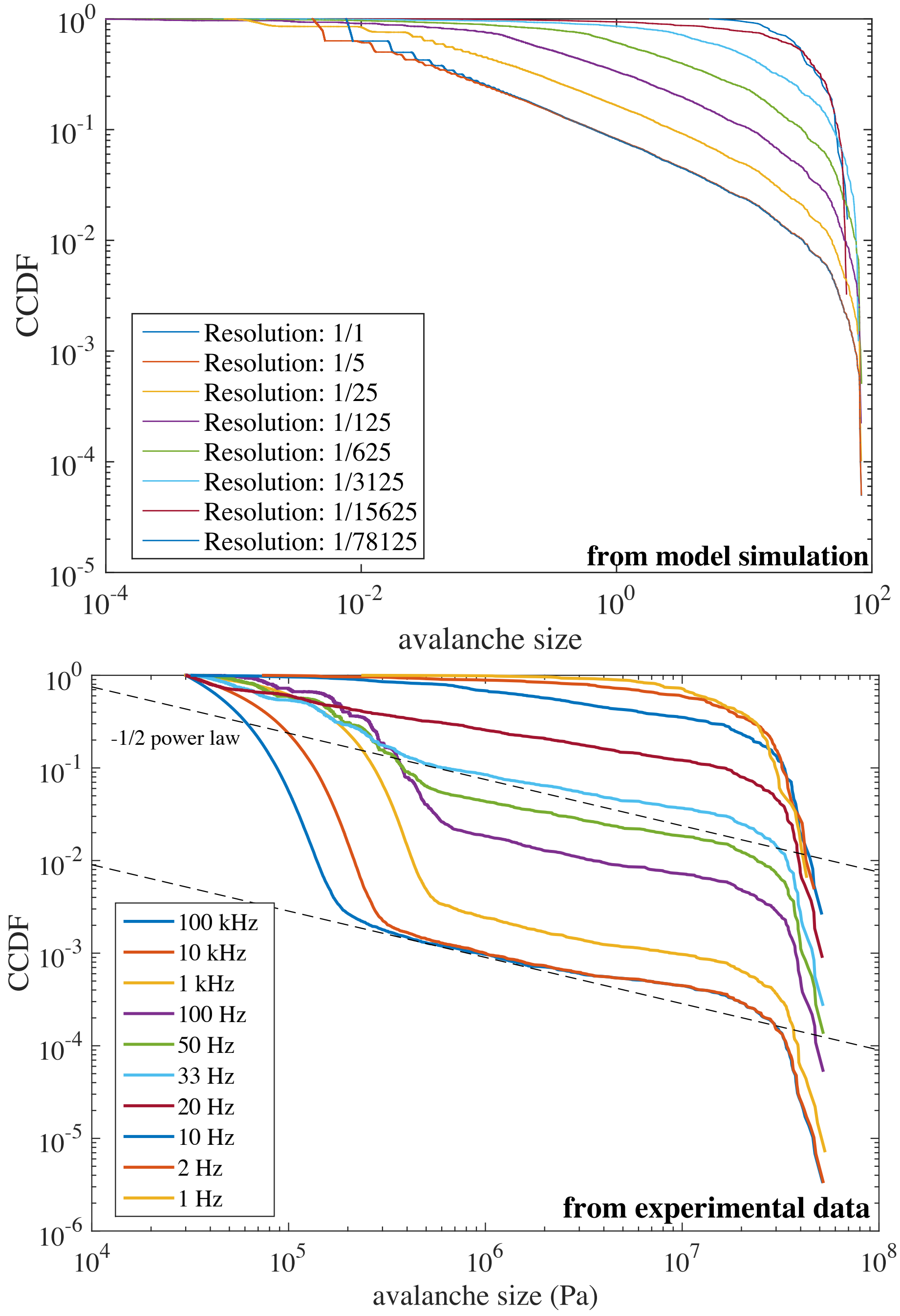

Figure 7.10: (top) Avalanche size distributions measured at different resolutions from simulations of the mean field model (from Ref. [20]) and (bottom) from BMG experiment (from Ref. [14]). The trend lines are power laws with exponent $1 - \tau = -1/2$ predicted by MFT. In both cases, the analysis described in Fig. 7.1 gives avalanche size distributions that become increasingly narrow at low resolution. Thus, low resolution can obscure power-law distributed jumps in the underlying signal. In the experimental data, a pronounced noise regime is visible for the higher resolutions, but is averaged out at lower resolutions.

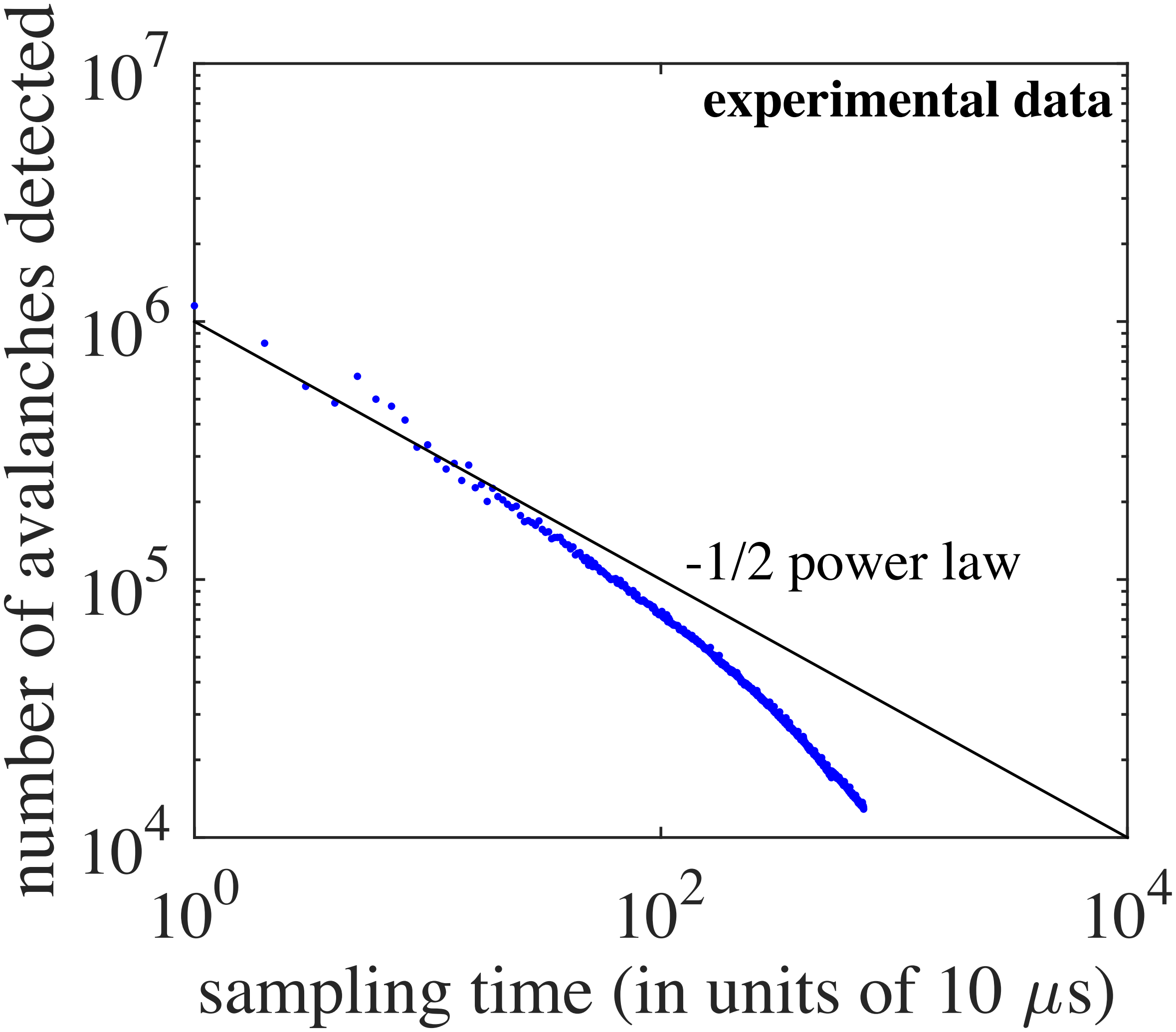

Figure 7.11: Number of avalanches collected versus sampling time t_s from the experimental data. The line is a power law with exponent $1 - \tau = -1/2$ from Eq. (7.9).

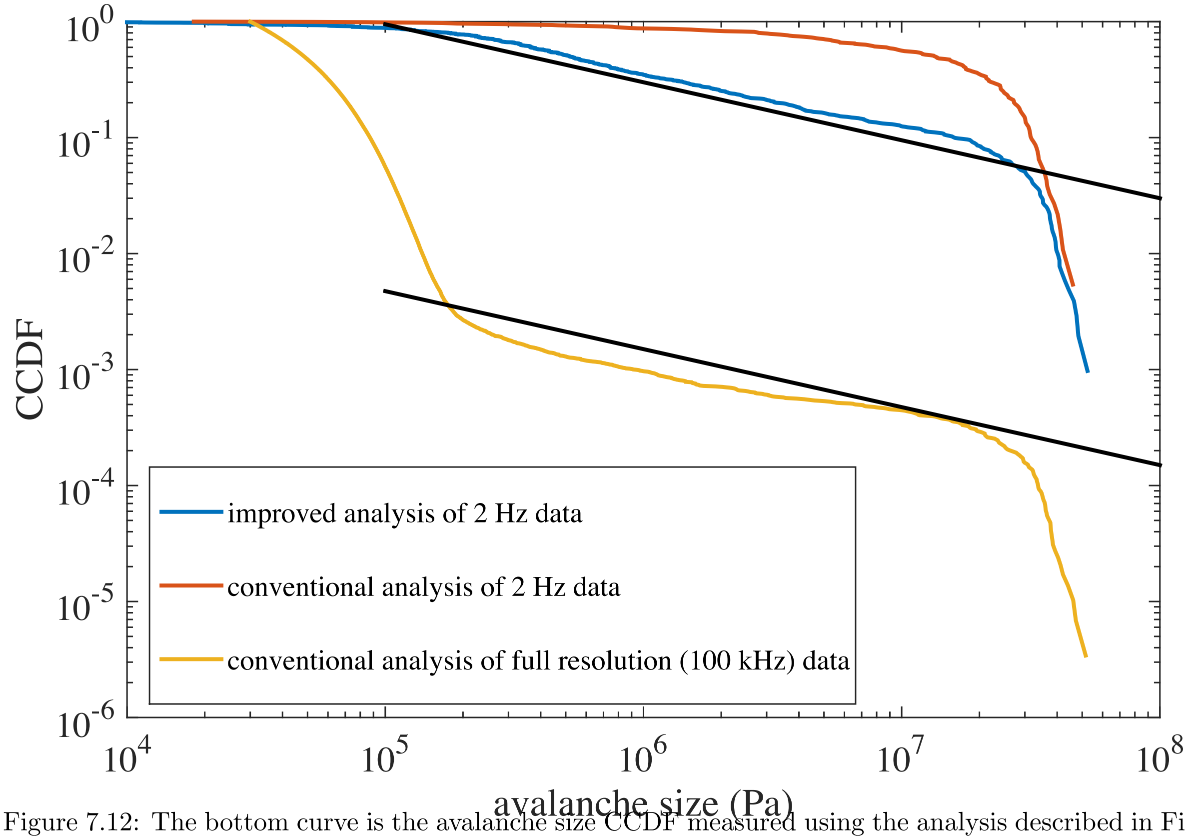

Figure 7.12: The bottom curve is the avalanche size CCDF measured using the analysis described in Fig. 7.1 on the full-resolution (100 kHz) experimental data. The scaling regime follows a power law with exponent $1 - \tau = -1/2$ in agreement with MFT. The top curve is the CCDF measured with the analysis when the same data is drastically downsampled to 2 Hz. The power law is no longer apparent. The middle curve is the CCDF measured using the improved method outlined in section 7.6.1 where the sample stress drops are analyzed from a tilted signal (see Eq. (7.17)). The $-1/2$ power law apparent in the 100 kHz data is recovered from the downsampled data.

where $v_0 \sim S_m/\delta t$, with S_m the minimum avalanche size and δt the minimum avalanche duration. v_0 may be thought of as the size of the initial "kick" starting an avalanche.

We can then compute the distribution of the sum of two independent avalanche sizes from this distribution. We first Laplace transform, giving

$$\tilde{P}(\lambda) = \int_0^\infty dS e^{-\lambda S} P(S) = \frac{v_0 e^{kv_0}}{\sqrt{2\pi}} \int_0^\infty \frac{dS}{S^{3/2}} e^{-(\lambda+k^2/2)S - v_0^2/2S} = e^{kv_0} e^{-\sqrt{2v_0^2(\lambda+k^2/2)}} \tag{7.21}$$

By the convolution theorem, the Laplace transform of the distribution of the sum $\Sigma_n = \sum_{j=1}^n S_j$ of n independent draws from $P(S)$ is just $\tilde{P}(\lambda)^n$. We can then inverse Laplace transform to get

$$P(\Sigma_n) = \int_{a+-i\infty}^{a+i\infty} \frac{d\lambda}{2\pi i} e^{\lambda \Sigma_n} \tilde{P}(\lambda)^n \tag{7.22}$$

where $a > -k^2/2$ to avoid the branch cut. The integral can be done by deforming the contour around the branch cut and shifting $\lambda \to \lambda - k^2/2$, giving

$$P(\Sigma_n) = \frac{e^{kv_0}}{\pi} e^{-k^2 \Sigma_n/2} \int_0^\infty d\lambda \sin\left(\sqrt{2v_0^2 \lambda}\right) e^{-\lambda \Sigma_n} = \frac{nv_0}{\sqrt{2\pi \Sigma_n^3}} e^{-\frac{1}{2\Sigma_n}(k\Sigma_n - nv_0)^2}. \tag{7.23}$$

The sum of n avalanches has the same distribution as a single avalanche with n times as large an initial kick [85].

7.7.1 Data collapse at low resolution

The physical scaling form predicted by the model, $P(S) \sim S^{-\tau} \mathcal{F}(k^\alpha S)$ can be tested by performing a scaling collapse for different K values. This scaling form implies a scaling form

$$C(S) = \int_S^\infty P(S') dS' \sim S^{1-\tau} \bar{\mathcal{F}}(k^\alpha S) \tag{7.24}$$

for the CCDF, where $\bar{\mathcal{F}}(x) = \int_1^\infty z^{-\tau} \mathcal{F}(zx) dz$ [8].

We use the loading spring constant K as a tuning parameter for our collapses. There are two complications that we correct for. First, since the definition of the stress drops scale with K, the avalanche sizes we use in the collapse are rescaled $S \to S/K$ before collapsing. We also tune the displacement rate v_d so that the interevent time $T_i \sim (Kv_d)^{-1}$ remains constant.

In the upper left panel of Fig. 7.9 we plot $C(S)S^{\tau-1}$ versus Sk^α, which according to Eq. (7.24) should give the plot of the scaling function $\bar{\mathcal{F}}$. We do this for three values of k and confirm that they all lie on the same curve. As we lower the resolution, the distributions become distorted and the scaling form ceases to hold. However, due to regularities in the behavior of the measured size distribution at different resolutions, an apparent data collapse can still be possible. In the upper right panel of Fig. 7.9 we show an apparent collapse we obtained for $t_s = 500$, after performing the naive avalanche analysis of Fig. 7.1 without tilting the stress-time curve. However, the exponents $\tau = 1$ and $\alpha = 1.5$ that collapse the data strongly deviate from the MFT values $\tau = 1.5$ and $\alpha = 2$ that yield a collapse for the full resolution data.

In the lower panels, we show that we can obtain decent collapses with the MFT exponents for $t_s = 100$ and $t_s = 1000$ when we use the improved analysis methods outlined in Sections 7.6.2 and 7.6.3.

7.8 Comparison with experiment

We compare our theoretical results with experimental data on bulk metallic glasses originally presented in [14]. The data is collected at a very high data acquisition rate of 100 kHz and the avalanche size distribution and average avalanche shapes show good agreement with mean field theory. See ref. [14] for details on the experiment and data analysis.

One complication in applying the above analysis to data is the presence of noise. We use Wiener filtering to reduce the noise amplitude (see ref. [14] for details). However, since the analysis uses a numerical derivative to detect stress drops (shown in Fig. 7.1), even a small amount of noise can have a large effect and there are still many small events that are a result of noise rather than material response. These “noise avalanches” can be seen as a sharp decrease on the left part of the 100 kHz CCDF in the bottom panel of Fig. 7.10. After the sharp decrease, a scaling regime emerges where the size distribution follows the predicted power law $C(S) \sim S^{-1/2}$. Avalanches from this region and larger are not polluted by noise.

In Fig. 7.10 we plot the avalanche size CCDFs obtained using the analysis (without tilting, see Fig. 7.1) at different resolutions from a model simulation and experiment. In both cases, we see that the distribution becomes narrower at lower resolution. In the CCDFs for the experimental data (bottom panel), a pronounced noise regime is visible for the higher resolutions, but disappears at lower resolutions since the noise averages out over long sampling times.

In the bottom panel of Fig. 7.10 we see that when the resolution is lowered to around 100 Hz, the power law begins to become shallower and below 50 Hz the power law begins to disappear entirely. This gives a rough lower bound for resolution at which we expect resolution effects to be important for stress drop distributions in this particular system. Since the key timescale is the avalanche nucleation rate (which is proportional to $1/NKv$), resolution effects can be avoided by decreasing the system size or decreasing the displacement rate rather than increasing the resolution.

In Fig. 7.11 we plot the number of avalanches collected versus the sampling time. We see rough agreement with the power law of $1-\tau=-1/2$ predicted by Eq. (7.9) for high resolutions but with a more pronounced deviation for larger sampling times (also see Fig. 7.4). This is due to the shorter scaling regime in the experimental data and deviations from scaling for large avalanches [14].

Finally, in Fig. 7.12, we use the method from section 7.6.1 to recover the correct power law exponent from the experimental data downsampled to 2 Hz, a resolution at which the traditional analysis yields a distribution with no power law regime. First the data was cut into increasing pieces and an appropriate stress increase rate r was determined by a linear fit for each section (see Eq. (7.11)). The measured value of r was about 6.5 ± 0.3 MPa/s throughout the sample. Then we tilted the lowered-resolution data according to the local values of r and took the distribution of sample stress drops for each sample in which the stress change was negative. The expected power law of $-1/2$ is recovered in the resulting CCDF.

7.9 Conclusion

Lowered resolution affects the measured avalanche distributions in several ways. Avalanche duration distributions are distorted significantly unless the sampling time is well below the average avalanche duration. For larger sampling times (lower resolutions), the apparent power law is steeper than the theoretical power law (see Fig. 7.2). Avalanche size distributions are much more robust and can be measured even when the sampling time is longer than the duration of the largest avalanches, but there can still be significant rounding of the shape of the size distribution.

For moderately low resolution where the sampling time is still much less than the average time between avalanches, tilting the data before measuring the stress drops makes it possible to recover the underlying avalanche size distribution to a good approximation. For very low resolutions with sampling times on the order of the interevent time, tilting the signal and using the sample stress drops described in Section 7.6.3 allows the recovery of a size distribution similar to the one that would be obtained at high acquisition rates, as well as the predicted model distribution.

Appendix A

(Appendix to Chapter 3)

A.1 Multiplicative noise: Itô and Stratonovich interpretations

When the noise term in a stochastic differential equation is multiplied by some function of the dependent variable, it is called "multiplicative noise". Unfortunately, the notation that physicists typically use to write down stochastic differential equations glosses over a dangerous ambiguity in equations with multiplicative noise [80]. To see the ambiguity, consider a discrete version of Eq. 3.9

$$v_{t+\delta t} - v_t = (c - kv_t + \sqrt{v_t}\eta_t)\,\delta t \tag{A.1}$$

with time step δt. In order for the noise η_t to have the correct properties in the continuum limit[1], it should consist of independent Gaussians, with mean zero and variance $2D/\delta t$, i.e.

$$\langle \eta_t \eta_{t'} \rangle = \frac{2D}{\delta t}\delta_{t,t'}. \tag{A.2}$$

We made a choice discretizing the term $\sqrt{v(t)}\eta(t)$ as $\sqrt{v_t}\eta_t$. For instance, we could have discretized it as $\sqrt{v_{t+\delta t}}\eta_t$ instead. It turns out that these choices lead to different continuum limits.

This contrasts with the case of non-stochastic equations. For instance, if we change the kv_t term in Eq. A.1 to $kv_{t+\delta t}$, the difference is of order δt^2 and can be ignored in the continuum limit. The stochastic term is different, however, since the noise is singular. The choice of $\sqrt{v_{t+\delta t}}\eta_t$ instead of $\sqrt{v_t}\eta_t$ in Eq. A.1 leads to a difference in the right hand side whose leading order term is $\frac{1}{2}\eta_t^2\delta t^2$, as can be seen by iterating under the square root and expanding. The random variable η_t^2 is positive with mean value $2D/\delta t$, so we expect the difference of $\frac{1}{2}\eta_t^2\delta t^2$ to make a contribution of order δt that cannot be neglected. Thus a stochastic equation written as

$$\frac{dv}{dt} = f(v) + g(v)\eta(t) \tag{A.3}$$

---

[1] For instance, the Brownian motion $B(t) = \int_0^t \eta(t')dt'$ should have variance $2Dt$.

can refer to as many different processes as there are discretizations of $g(v)$.

The two most common "interpretations" of Eq. A.3 are called the *Itô* and *Stratonovich* interpretations. The Itô interpretation corresponds to the interpretation we picked in Eq. A.1, where the $v(t)$ in the multiplicative noise is evaluated at the previous time step, i.e.

$$v_{t+\delta t} - v_t = \left(f(v_t) + g(v_t)\eta_t\right)\delta t. \tag{A.4}$$

Instead of using previous value of v, the Stratonovich interpretation uses the average value of v at the previous and current time step:

$$v_{t+\delta t} - v_t = \left(f(v_t) + g\left(\frac{v_{t+\delta t} + v_t}{2}\right)\eta_t\right)\delta t. \tag{A.5}$$

The fact that the noise is singular is also important when changing variables [80].For the change of variables $v \to x(v)$, we can Taylor expand the difference

$$x_{t+\delta t} - x_t \equiv \delta x = x'(v)\delta x + \frac{1}{2}x''(v)\delta x^2 + \ldots \tag{A.6}$$

The second term isn't truly second-order because δx^2 contains the term $g(x)^2\eta_t^2\delta t^2$, which is of order δt since $\eta_t^2 \sim 2D/\delta t$. The law of large numbers combined with the fact that we can discretize the noise as finely as we wish allows us to replace η_t^2 by its expected value[2]. Then we can write

$$\delta x = x'(v)f(v)\delta t + x'(v)\eta_t\delta t + Dx''(v)g(v)^2\delta t. \tag{A.7}$$

Note that if we had performed a naive change of variables using the rules of ordinary calculus we would have missed the last term. In Chapter 4 we will use the change of variables $x = 2\sqrt{v}$ to analyze Eq. 3.9 in the Itô interpretation. Plugging in $x(v) = 2\sqrt{v}$, $f(v) = (c - kv)$ and $g(v) = \sqrt{v}$ we get

$$\frac{dx}{dt} = \frac{2c}{x} - \frac{k}{2}x - \frac{D}{x} + \eta(t). \tag{A.8}$$

The Itô interpretation is the most straightforward to numerically integrate, since the Stratanovich is an implicit equation in $v_{t+\delta t}$. However, the Stratonovich interpretation can be more convenient since the usual rules of calculus apply for changing variables. Fortunately, the Stratonovich interpretation of a process is always equivalent to a process in the Itô interpretation with an additional drift term. For instance, the

---

[2] This is a rigorous result called Itô's Lemma [81]

Stratonovich interpretation of the ABBM equation (Eq. 3.9) is the same process as the ABBM model, but with $c \to c + D/2$.

What's more important is to understand physically which interpretation is the correct one to use for a given multiplicative noise equation. If the white noise $\eta(t)$ is an approximation to weakly correlated noise, the Stratonovich interpretation is correct. This is because if the noise is actually a continuous function, the usual rules for changing variables rules will be correct. Since physical noise is generally continuous, the Stratonovich interpretation is usually correct for physical systems. The Itô interpretation is appropriate when the noise is an approximation for a discrete sequence of shocks, as is typical in financial models. In the case of the ABBM equation, the noise models the random changes in the pinning force due to the changes in the interface configuration. The reason it is multiplied by $\sqrt{v}$ is because a more rapidly moving interface has a larger change in configuration. However, this implies that the relevant velocity is the one from the instantaneous past, and thus the Itô interpretation is correct.

Appendix B

(Appendix to Chapter 4)

B.1 Numerics

In numerical simulations, we use an Euler - Maruyama method to integrate the ABBM equation (Eq. (3.9)) with $D = 1/2$. This scheme, however, does not preserve the positivity constraint of the solution. Nonetheless, since we are interested in avalanches, i.e. the evolution in between zero crossings, we discard the times when the velocities become negative. An avalanche is started from $v = 1$ and evolved until $v \leq 0$ at which time it is declared over and recorded. Then a new avalanche is restarted from $v = 1$. Since the noise is uncorrelated, this closely resembles the reflecting boundary condition at $v = 0$ in the steady state evolution of the model. This method is simple and fast, but the disadvantage is that the crude integration rule and boundary conditions introduce inaccuracies for small avalanches ($T \ll 10^3$, $S \ll 10^6$). Another method tried was directly implementing the discrete time equation Eq. (2.21) which obtained results consistent with the first method for $k = c = 0$, with a somewhat faster convergence to the continuum limit in the scaling functions.

B.2 Derivation of exact propagator for arbitrary c and k

To compute the exact propagator it is convenient to work in the untransformed variable as in Ref. [77].The Fokker-Planck equation for the ABBM model is

$$\partial_t P(v,t) = \partial_v((kv - c)P(v,t)) + \frac{1}{2}\partial_v^2(vP(v,t)). \tag{B.1}$$

We will be interested in the absorbing boundary condition solution. However, the norm-preserving, reflecting solution is easier to find. It is characterized by a zero flux condition at the $v = 0$ boundary:

$$\lim_{v \to 0^+} \frac{\partial}{\partial t} \int_v^\infty P(u,t)du = -\lim_{v \to 0^+} \left((kv - c)P(v,t) + \frac{1}{2}\partial_v(vP(v,t)) \right) = 0 \tag{B.2}$$

We will work with the Laplace transform of $P(v,t)$ in v,

$$\tilde{P}(s,t) = \int_0^\infty e^{-sv} P(v,t) dv. \tag{B.3}$$

Laplace transforming Eq. (B.1), the LHS becomes $\partial_t \tilde{P}(s,t)$. Integrating the RHS by parts,

$$\begin{aligned} s\int_0^\infty \left((kv-c)P(v,t) + \frac{1}{2}\partial_v(vP(v,t))\right) e^{-sv} dv &= s\int_0^\infty \left((kv-c) + \frac{1}{2}svP(v,t)dv\right) \\ &= s\int_0^\infty \left((-k\partial_s - c)(P(v,t)e^{-sv}) - \frac{1}{2}s\partial_s(P(v,t)e^{-sv})\right) dv \\ &= -s\left(\frac{s}{2}+k\right)\partial_s \tilde{P}(s,t) - sc\tilde{P}(s,t), \end{aligned} \tag{B.4}$$

where the zero flux condition eliminated the boundary term in the first integration by parts. The Laplace-transformed version of Eq. (B.1) is then

$$\partial_t \tilde{P}(s,t) + s\left(\frac{s}{2}+k\right)\partial_s \tilde{P}(s,t) = -sc\tilde{P}(s,t). \tag{B.5}$$

This can be solved with the initial condition $\tilde{P}(s,0) = e^{-sv_0}$ by the method of characteristics, giving

$$\tilde{P}(s,t) = \frac{1}{\left(1+\frac{s}{2k}\left(1-e^{-kt}\right)\right)^{2c}} \exp\left(-\frac{sv_0 e^{-kt}}{1+\frac{s}{2k}\left(1-e^{-kt}\right)}\right). \tag{B.6}$$

Let $a \equiv (1-e^{-kt})/2k$ and $b \equiv v_0 e^{-kt}$. Then we have

$$\begin{aligned} \tilde{P}(s,t) &= \frac{e^{-bs/(1+as)}}{(1+as)^{2c}} \\ &= \frac{1}{(1+as)^{2c}} e^{-b/a} \exp\left(\frac{b}{a(1+as)}\right) \\ &= e^{-b/a} \sum_{n=0}^{\infty} \frac{(b/a)^n}{n!\,(1+as)^{n+2c}} \end{aligned} \tag{B.7}$$

The Laplace transform identities

$$\mathcal{L}^{-1}\left(\tilde{f}(as+1)\right) = \frac{1}{a} e^{-x/a} f(x/a) \tag{B.8}$$

and

$$\mathcal{L}^{-1}\left(\frac{1}{s^n}\right) = \frac{x^{n-1}}{\Gamma(n)} \tag{B.9}$$

can then be used to perform the inverse term by term, giving

$$\begin{aligned} P(v,t) &= \frac{1}{a} e^{-(v+b)/a} \sum_{n=0}^{\infty} \frac{(b/a)^n (v/a)^{n+2c-1}}{n!\Gamma(n+2c)} \\ &= \frac{1}{a}\left(\frac{v}{b}\right)^{c-1/2} e^{-(v+b)/a} \sum_{n=0}^{\infty} \frac{\left(\sqrt{bv}/a\right)^{2n+2c-1}}{n!\Gamma(n+2c)} \end{aligned} \tag{B.10}$$

where the second equality is a rearrangement in order to make use of the Bessel function formula

$$I_\alpha(z) = \sum_{n=0}^{\infty} \frac{(z/2)^{2n+\alpha}}{n!\Gamma(n+\alpha+1)}. \tag{B.11}$$

Finally, plugging in for a and b, we get

$$P(v,t) = \frac{2k}{1-e^{-kt}} \left(\frac{v_0 e^{-kt}}{v}\right)^{1/2-c} \exp\left(-2k\frac{v+v_0e^{-kt}}{1-e^{-kt}}\right) I_{2c-1}\left(\frac{4k\sqrt{vv_0e^{-kt}}}{1-e^{-kt}}\right). \tag{B.12}$$

Employing $I_\alpha(z) \approx (z/2)^\alpha/\Gamma(\alpha+1)$ (as $z \to 0$) we can take the limit as $t \to 0$ and get

$$P(v, t\to\infty) = \frac{(2k)^{2c}}{\Gamma(2c)} v^{-1+2c} e^{-2kv} \tag{B.13}$$

which we recognize as the steady state distribution obtained from the Boltzmann approach earlier.

The all-important absorbing boundary condition propagator is simply the same expression as the reflecting boundary with the opposite order Bessel function.

In order to derive it we need to allow probability to flow into $v = 0$ so that the solution is norm-decreasing. Therefore, we pick up a surface term from the Laplace transform, and we have

$$\partial_t \tilde{P}(s,t) + s\left(\frac{s}{2}+k\right)\partial_s \tilde{P}(s,t) = -sc\tilde{P}(s,t) + f(t) \tag{B.14}$$

where

$$f(t) = \lim_{v\to 0^+}\left((kv-c)P(v,t) + \frac{1}{2}\partial_v(vP(v,t))\right). \tag{B.15}$$

We will determine the flux $f(t)$ from boundary conditions below. This can likewise be solved with initial conditions $\tilde{P}(s,0) = e^{-v_0 s}$ by the method of characteristics, giving

$$\tilde{P}(s,t) = \left(\frac{1}{1+\frac{s}{2k}(1-e^{-kt})}\right)^{2c} \exp\left(-\frac{sv_0e^{-kt}}{1+\frac{s}{2k}(1-e^{-kt})}\right) + \int_0^t f(\tau)\left(\frac{1}{1+\frac{s}{2k}(1-e^{-k(t-\tau)})}\right)^{2c} d\tau. \tag{B.16}$$

We will demand that $\lim_{v\to 0} P(v,t) < \infty$ which means, roughly that $P(v,t) \sim v^\epsilon$ where $\epsilon \geq 0$. This translates to $\tilde{P}(s,t) \sim s^{-1-\epsilon}$ or $s\tilde{P}(s,t) \sim s^{-\epsilon}$ as $s \to \infty$. Therefore, we have $\lim_{s\to\infty} s^{\alpha}\tilde{P}(s,t) = 0$ for $\alpha < 1$. We know from the reflecting propagator solution that $v = 0$ is inaccessible when $2c > 1$, so at rates beyond this, the motion never comes to a stop and there is one infinite avalanche. Therefore, we can assume $2c < 1$. Then we have

$$\begin{aligned} 0 &= \lim_{s\to 0}\left(1+\frac{s}{2k}(1-e^{-kt})\right)^{2c}\tilde{P}(s,t) \\ &= \exp\left(\frac{-2kv_0e^{-kt}}{1-e^{-kt}}\right)+\int_0^t f(\tau)\left(\frac{1-e^{-kt}}{1-e^{-k(t-\tau)}}\right)^{2c}d\tau \end{aligned} \tag{B.17}$$

Substituting $z^{-1} = e^{kt} - 1$ and $\zeta^{-1} = e^{k\tau} - 1$ gives

$$\int_z^{\infty} g(\zeta)(\zeta - z)^{-2c} d\zeta = -e^{-2zkv_0} \tag{B.18}$$

where

$$g(\zeta) = \frac{1}{k} f(\ln(1-\zeta^{-1})/k)\frac{\zeta^{2c}}{\zeta(\zeta-1)}. \tag{B.19}$$

This can be turned to

$$\int_0^{\infty} g(z+\zeta)\zeta^{-2c}d\zeta = -e^{-2kv_0z} \tag{B.20}$$

which can be easily solved by inspection, giving

$$g(z) = -\frac{1}{\Gamma(1-2c)}(2v_0k)^{1-2c}e^{-2v_0kz} \tag{B.21}$$

Plugging back in τ,

$$f(\tau) = \frac{-k}{\Gamma(1-2c)}\frac{1}{1-e^{-k\tau}}\left(\frac{2kv_0e^{-k\tau}}{1-e^{-k\tau}}\right)^{1-2c}\exp\left(-\frac{2kv_0e^{-k\tau}}{1-e^{-k\tau}}\right) \tag{B.22}$$

Using the same variables ζ and z as before, we have

$$\begin{aligned} \int_0^t d\tau f(\tau)\left(\frac{1}{1+\frac{s}{2k}(1-e^{-k(t-\tau)})}\right)^{2c} &= -\frac{(2v_0k)^{1-2c}}{\Gamma(1-2c)}\int_z^{\infty} d\zeta e^{-2kv_0\zeta}\left(\frac{1+z}{\zeta(1+z)+\frac{s}{2k}(\zeta-z)}\right)^{2c} \\ &= -\frac{(2v_0k)^{1-2c}e^{-2kv_0z}}{\Gamma(1-2c)}\int_0^{\infty} d\zeta e^{-2kv_0\zeta}\left(\frac{1}{z+\zeta\left(1+\frac{s}{2k(1+z)}\right)}\right)^{2c} \end{aligned} \tag{B.23}$$

This term can be inverse Laplace transformed and cranked to give

$$\begin{aligned}
- & \quad \frac{(2v_0k)^{1-2c}}{\Gamma(1-2c)}e^{-2kv_0z}\int_0^\infty e^{-2kv_0\zeta}2^{2c}e^{-2kv(1+z)-2kvz(1+z)/\zeta}k(1+z)\left(\frac{\zeta}{kv(1+z)}\right)^{1-2c}\frac{1}{\zeta\Gamma(2c)}d\zeta \\
= & \quad -\frac{2\sin(2c\pi)k}{\pi}\left(\frac{v_0}{v}\right)^{1-2c}(1+z)^{2c}e^{-2k(v_0z+v(1+z))}\int_0^\infty \zeta^{-2c}e^{-2kv_0(\zeta+(v/v_0)z(1+z)/\zeta)}d\zeta \\
= & \quad -\frac{2\sin(2c\pi)k}{\pi}\left(\frac{1}{2kv}\right)^{1-2c}(1+z)^{2c}e^{-2k(v_0z+v(1+z))}\int_0^\infty \zeta^{-2c}e^{-(\zeta+4k^2vv_0z(1+z)\zeta)}d\zeta \\
= & \quad -\frac{2\sin(2c\pi)(2k)^{2c}}{\pi}v^{-1+2c}(1+z)^{2c}e^{-2k(v_0z+v(1+z))}(4k^2vv_0z(z+1))^{1/2-c}K_{2c-1}\left(4k\sqrt{vv_0z(1+z)}\right) \\
= & \quad -\frac{4\sin(2c\pi)k}{\pi}(1+z)\left(\frac{v_0z}{v(z+1)}\right)^{1/2-c}e^{-2k(v_0z+v(1+z))}K_{2c-1}\left(4k\sqrt{vv_0z(1+z)}\right) \\
= & \quad -\frac{4\sin(2c\pi)k}{\pi}\frac{1}{1-e^{-kt}}\left(\frac{v_0e^{-kt}}{v}\right)^{1/2-c}\exp\left(-\frac{2k\left(v+v_0e^{-kt}\right)}{1-e^{-kt}}\right)K_{2c-1}\left(\frac{4k\sqrt{vv_0e^{-kt}}}{1-e^{-kt}}\right) \\
= & \quad \frac{2k}{1-e^{-kt}}\left(\frac{v_0e^{-kt}}{v}\right)^{1/2-c}\exp\left(-\frac{2k\left(v+v_0e^{-kt}\right)}{1-e^{-kt}}\right)\left(I_{1-2c}\left(\frac{4k\sqrt{vv_0e^{-kt}}}{1-e^{-kt}}\right)-I_{2c-1}\left(\frac{4k\sqrt{vv_0e^{-kt}}}{1-e^{-kt}}\right)\right)
\end{aligned}$$

We eventually plugged back in $z^{-1}=1-e^{kt}$. Some standard identities used include

$$\mathcal{L}^{-1}\left\{\left(z+\zeta\left(1+\frac{s}{2k(1+z)}\right)\right)^{-2c}\right\}(v)=\frac{2^{2c}e^{-2kv((1+z)+z(1+z)/\zeta)}k(1+z)\left(\frac{\zeta}{kv(1+z)}\right)^{1-2c}}{\zeta\Gamma(2c)}$$

$$\Gamma(z)\Gamma(1-z)=\frac{\pi}{\sin(\pi z)},$$

$$\int_0^\infty t^{-2c}\exp\left(-t-a/t\right)dt=2a^{1/2-c}K_{2c-1}(2\sqrt{a}),$$

$$K_\alpha(z)=\frac{\pi}{2\sin(\pi z)}\left(I_\alpha(z)-I_{-\alpha}(z)\right)$$

This must be added to the Laplace transform of the first term, which is just the reflecting propagator derived previously. The result for the absorbing propagator is then

$$P(v,t)=\frac{2k}{1-e^{-kt}}\left(\frac{v_0e^{-kt}}{v}\right)^{1/2-c}\exp\left(-\frac{2k\left(v+v_0e^{-kt}\right)}{1-e^{-kt}}\right)I_{1-2c}\left(\frac{4k\sqrt{vv_0e^{-kt}}}{1-e^{-kt}}\right). \tag{B.24}$$

Appendix C

(Appendix to Chapter 5)

C.1 Classical extreme value theory

Classical extreme value statistics applies to independent, identically distributed (IID) random variables $\{X_i\}_{i=1}^{N}$ with the same parent cumulative distribution function (CDF) $F(x) \equiv P(X \leq x)$. The CDF for the maximum M_n of n IID variables is given by

$$F_{M_n}(x) = P(M_n \leq x) = \prod_{i=1}^{n} P(X_i \leq x) = F_X(x)^n. \tag{C.1}$$

In many cases, the statistics of the maximum $M_n \max(X_i)_{i=1}^{n}$ follows a universal scaling law as $n \to \infty$, analogous to the central limit theorem. The central limit theorem is a universal scaling law for the sum $S_n \equiv \sum_{i=1}^{n} X_i$. It says that

$$\lim_{n\to\infty} P\left(\frac{S_n - b_n}{a_n} \leq x\right) = \Phi(x) \tag{C.2}$$

where $\Phi(x)$ is the CDF for the standard normal distribution, $b_n = n\mathrm{E}(X_i)$ and $a_n = \mathrm{Var}(X_i)\sqrt{n}$. This holds for IID variables whenever the parent distribution has finite variance.

The maximum M_n may follow a similar scaling form to the sum:

$$\lim_{n\to\infty} P\left(\frac{M_n - b_n}{a_n} \leq x\right) = G(x) \tag{C.3}$$

where $G(x)$ is a universal limit distribution. Fisher and Tippett [90] showed that if a nontrivial limit distribution $G(x)$ exists for some rescaling sequences a_n and b_n, it will satisfy the functional equation

$$G(x)^n = G\left(\frac{x - \beta_n}{\alpha_n}\right) \tag{C.4}$$

for some sequences α_n and β_n. Their argument has the flavor of a renormalization group argument: Imagine we have n groups of $m \gg 1$ IID variables. If Eq. (C.3) holds, the maximum $M_m^{(i)}$ of any of the n groups will have the CDF

$$F_{M_m}(x) = P(M_m \leq x) \approx G\left(\frac{x - b_m}{a_m}\right) \tag{C.5}$$

since m is large. The group maxima $M_m^{(i)}$ for $i = 1 \ldots n$ are n IID variables from this distribution, so by Eq. (C.1), the maximum of the n maxima has the CDF $F_{M_m}(x)^n \approx G\left(\frac{x-b_m}{a_m}\right)^n$. However, the maximum of the set of group maxima is just the maximum M_{mn} of the whole sample, which by Eq. (C.3) has the CDF

$$F_{M_{mn}}(x) \approx G\left(\frac{x - b_{mn}}{a_{mn}}\right) \tag{C.6}$$

since mn is large. Equating these two expressions gives

$$G\left(\frac{x - b_m}{a_m}\right)^n = G\left(\frac{x - b_{mn}}{a_{mn}}\right). \tag{C.7}$$

Shifting and rescaling x gives Eq. (C.4) where $\alpha_n = \lim_{m\to\infty} a_{mn}/a_m$ and $\beta_n = \lim_{m\to\infty}(b_{mn} - b_n)/a_m$.

Eq. (C.4) has an renormalization group interpretation in that the limit distribution G is a fixed point of a coarse-graining (taking the maximum of the blocks of variables) and rescaling procedure. By solving the functional equation Eq. (C.4), Fisher and Tippett showed that if a nontrivial $G(x)$ exists, it can be put into one of the following three forms by shifting and rescaling x:

1. The reverse Gumbel distribution

   $$G_1(x) = e^{-e^{-x}}, \tag{C.8}$$

   which satisfies Eq. (C.4) for $\alpha_n = 1$ and $\beta_n = \log(n)$. This is typically the limit distribution when the right tail of the parent distribution PDF decays faster than any power law. For instance, when the X_i are from the standard exponential distribution $F_X(x) = 1 - \exp(-x)$ for $x > 0$, we have

   $$P(M_n - \log(n) \leq x) = F_X(x + \log(n))^n = \left(1 - \frac{1}{n}e^{-x}\right)^n \to e^{-e^{-x}}. \tag{C.9}$$

2. The Fréchet distribution with parameter $\alpha > 0$

   $$G_2(x) = \begin{cases} 0 & x \leq 0 \\ e^{-x^{-\alpha}} & x > 0, \end{cases}, \tag{C.10}$$

   which satisfies Eq. (C.4) for $\alpha_n = n^{1/\alpha}$ and $\beta_n = 0$. This is the limit distribution when the right tail of the parent distribution PDF decays as a power law $f(x) \sim x^{-(\alpha+1)}$. For instance if the X_i are power-law distributed $F_X(x) = 1 - x^{-\alpha}$, for $x > 0$, we have

$$P(M_n n^{-1/\alpha} \leq x) = F_X(x n^{1/\alpha})^n = \left(1 - \frac{1}{n} x^{-\alpha}\right)^n \to e^{-x^{-\alpha}} \tag{C.11}$$

3. The reverse Weibull distribution with parameter $\alpha > 0$

$$G_3(x) = \begin{cases} e^{-(-x)^\alpha} & x \leq 0 \\ 1 & x > 0, \end{cases} \tag{C.12}$$

which satisfies Eq. (C.4) for $\alpha_n = n^{-1/\alpha}$ and $\beta_n = 0$. This is the limit distribution when the right tail of the parent PDF is bounded and has the form $f(x) \sim (x_m - x)^{\alpha-1}$ near the upper bound x_m. For instance if the X_i have the distribution $F_X(x) = 1 - (1 - x)^\alpha$ for $x \in (0, 1)$ (the uniform distribution is a special case with $\alpha = 1$), then we have

$$P((M_n - 1)n^{1/\alpha} \leq x) = F_X(x n^{-1/\alpha} + 1)^n = \left(1 - \frac{1}{n}(-x)^\alpha\right)^n \to e^{-(-x)^\alpha} \tag{C.13}$$

If the distribution is bounded but decays to zero slower than any power law near the upper bound, e.g. $p(x) \sim \exp(1/(x_m - x))$, then the limit distribution is Gumbel.

C.2 Relationship of classical EVT to avalanche maxima

While an avalanche can be thought of as a sequence of random variables, they are not independent, so classical extreme value theory does not apply. Although there is no general theory of extreme values for variables with arbitrary joint distributions, substantial progress has been made in several cases. For instance, Berman's theorem says that the EVS of a weakly-correlated Gaussian process is also governed by the Fisher-Tippett distributions [91, 92]. This corresponds to a power spectrum density that decays with the frequency as $S_f \sim f^{-a}$, with an exponent $0 \leq a \leq 1$. Also, the EVS of time records with long-term persistence of Gaussian distributed fluctuations with $a < 1$ converges to the Fisher-Tippett distribution [93]. The same asymptotic law also determines the distribution of maximum heights of periodic, Gaussian $1/f$-noise [94, 95], where the maximum is measured relative to the mean.

On the other hand, the extreme value statistics of a correlated Gaussian process with $a > 1$ typically has a simple scaling form with the duration, as in our Eq. (5.12). The precise scaling function is depends on the boundary conditions, the value from which the extremum is measured, as well as other ordering constraints on the time evolution [82, 95]. For example, different scaling functions are obtained for the maximum heights of periodic Gaussian interfaces: if the maximum is measured relative to the spatially averaged height, the corresponding EVS is determined by the so-called Airy distribution function [96, 82, 95, 97], whereas measuring the maximum relative to the boundary value leads to the Rayleigh distribution [98, 99].

Although we have derived the exact functional form of $P(v_m)$, it is important to note that the $\mu = -2$ exponent follows essentially from two facts. The first is that the scaling forms given by Eqs. (5.12) and (5.31) have the exponents one would assume from dimensional analysis, and the second is that the integral leading to Eq. (5.40) converges when its bounds are taken to 0 and ∞. Under these conditions, the fluctuations in v_m are distributed narrowly about the average value $\langle v_m|T\rangle \sim T$, and so we expect the maximum velocity to have the same scaling exponent as the duration. However, there is no guarantee that these conditions hold in all cases.

In fact, this simple scaling by dimensional analysis runs contrary to what one might normally expect for an extreme value distribution. For example, if one wanted to make a simple argument, one could ignore correlations and boundary conditions and crudely approximate the avalanche as a sequence of $N = T/\delta t$ independent, exponentially distributed variables with average value $\langle v|T\rangle = AT$ where δt is the duration of a time step and A is a proportionality constant with the same dimensions as D. Then, the probability distribution function of the maximum value is given by

$$P(v_m|T) = \frac{N}{AT} e^{-v_m/AT} \left(1 - e^{-v_m/AT}\right)^{N-1}. \tag{C.14}$$

The expectation value of v_m can be determined by using the binomial expansion

$$P(v_m|T) = \frac{N}{AT} \sum_{k=0}^{N-1} \frac{(N-1)!(-1)^k}{k!(N-1-k)!} e^{-(k+1)v_m/AT}. \tag{C.15}$$

The integration corresponding to the first moment can be performed term by term, and the average maximum takes the form

$$\langle v_m|T\rangle = \frac{N}{AT} \sum_{k=0}^{N-1} \frac{(N-1)!(-1)^k}{k!(N-1-k)!} \frac{(AT)^2}{(k+1)^2}. \tag{C.16}$$

This is equivalent to

$$\langle v_m|T\rangle = AT\left(\Psi(N+1) + \gamma\right) \tag{C.17}$$

where $\Psi(x) = \frac{d \log \Gamma(x)}{dx}$ and γ is Euler's constant. As $T \to \infty$, this expression scales asymptotically as $AT \log(T/\delta t)$. The logarithmic enhancement is due to the fact that the random variable has $T/\delta t$ independent tries to achieve a value well above its average. Integrating this against the duration distribution $P(T) \sim T^{-2}$

gives a maximum value distribution with leading order behavior $P(v_m) \sim \log(v_m) v_m^{-2}$, a slower decay than the exact answer $P(v_m) \sim v_m^{-2}$. However, temporal correlations change the picture considerably, preventing the average maximum value from scaling faster than the average, so the actual scaling law is $\langle v_m | T \rangle \sim \langle v | T \rangle \sim T$ which corresponds to $P(v_m) \sim v_m^{-2}$.

C.3 Stress-integrated distributions

In Table 5.1 we report exponents for stress-integrated distributions (see also Table 6.1 in Chapter 6). These quantities apply to plasticity experiments where the stress is increased from some small value to its critical value without reaching a steady state, and avalanches are measured throughout the experiment (see, e.g. [11]). Similarly, field-integrated exponents are relevant to experiments on magnets where the avalanches occur throughout the hysteresis loop [100]. The integrated exponent predictions for these types of experiments are different from experiments where the system reaches a steady state in which the stress fluctuates near its critical value (e.g. [14]).

The calculations in this chapter were done assuming fixed k, where k is the "loading spring stiffness" (or a locally-coupled demagnetizing field strength in the case of Barkhausen noise). Relaxation of the loading spring allows stress to "leak" out of the system during an avalanche. The stiffness controls the distance to criticality so that $f \equiv \frac{|\Sigma - \Sigma_c|}{\Sigma_c} \sim k$ [2].

Thus, for a plasticity experiment for which avalanches are measured at a fixed external stress Σ, we expect a scaling form for the avalanche size distribution of

$$P(S; f) \sim S^{-\tau} \mathcal{F}(A S f^{1/\sigma}) \tag{C.18}$$

where $f \equiv \frac{\Sigma_c - \Sigma}{\Sigma_c}$ and A is a non-universal constant with units of $1/S$. In MFT, $\tau = 3/2$ and $\sigma = 1/2$, in accordance with Eq. (4.52) and the correspondence $k \sim f$. The scaling function $\mathcal{F}(x)$ decays exponentially for $x \gg 1$.

In an experiment where the stress is ramped up to its critical value without reaching the steady state, avalanches occur at many values of f and thus are drawn from different distributions of the form of Eq. (C.18). Since avalanches occur at larger distances to criticality, we expect that the distribution of avalanche sizes would decay faster than if the stress were fixed at a value close to Σ_c.

Naively, we can integrate over the values of stress to arrive at the distribution:

$$\begin{aligned} P_{\text{int}}(S) &= \int P(S,f)df \\ &\sim \int S^{-\tau}\mathcal{F}(ASf^{1/\sigma})df \\ &= A^{-\sigma}S^{-(\tau+\sigma)}\int \mathcal{F}(z^{1/\sigma})dz \end{aligned} \tag{C.19}$$

where we substituted $z = f(AS)^{\sigma}$. Therefore, the stress-integrated distribution scales as a power law $P_{\text{int}}(S) \sim S^{-(\tau+\sigma)}$ where $\tau+\sigma = 2$ in MFT.

A reasonable objection to this procedure is that it implicitly assumes that we uniformly sample over all values of f, i.e. each value of f is assumed to have (on average) equal likelihood of nucleating an avalanche as we increase the stress. This is not true, but nonetheless we will show that the naive integration generally gives the correct exponent when there is no singular dependence of nucleation probability on stress.

Say instead that there is a distribution $P(f)$ that gives a weight at each value of f corresponding to the probability of an avalanche occurring at stress Σ where $f = \frac{\Sigma_c-\Sigma}{\Sigma_c}$. The integrated distribution is then given by

$$P_{\text{int}}(S) = \int_0^1 P(S;f)P(f)df \sim A^{-\sigma}S^{-(\tau+\sigma)}\int_0^{(AS)^{\sigma}} \mathcal{F}(z^{1/\sigma})P\left(\frac{z}{(AS)^{\sigma}}\right)dz. \tag{C.20}$$

The scaling function $\mathcal{F}(x)$ decays for $x \gg 1$, thus if $AS \gg 1$, we can take the upper limit of the integral to infinity. This just means that we are looking at large avalanches and is a safe assumption as long as enough avalanches have been nucleated near the critical stress $f = 0$. If, in addition, the function $P(f)$ is approximately constant over a range from zero up to a value on the order of $\sim (AS)^{-\sigma}$, then we can approximate $P(z(AS)^{-\sigma}) \approx P(0)$ and pull it out of the integral, giving

$$P_{\text{int}}(S) \sim A^{-\sigma}S^{-(\tau+\sigma)}P(0)\int_0^{\infty} \mathcal{F}(z^{1/\sigma})dz \tag{C.21}$$

which has the same form as the naive integration.

Obviously, in the case that the stress distribution is concentrated at the critical stress, i.e. $P(f) = \delta(f)$, the stress-integrated exponent (and thus the above derivation) cannot be correct because we must get $P(S) \sim S^{-\tau}$. To see where it goes wrong, let's assume $P(f) = \frac{1}{f^*}e^{-f/f^*}$, so that we recover the distribution $\delta(f)$ when $f^* \to 0$ and we expect $P(S) \sim S^{-\tau+\sigma}$ when f^* is large. Plugging this in, we get

$$P_{\text{int}}(S) \sim A^{-\sigma}S^{-(\tau+\sigma)}\frac{1}{f^*}\int_0^{\infty} \exp\left(-\frac{z}{(AS)^{\sigma}f^*}\right)\mathcal{F}(z^{1/\sigma})dz. \tag{C.22}$$

When $(AS)^\sigma f^* \gg 1$, the $\mathcal{F}(z^{1/\sigma})$ factor decays out long before the other factor and the integral is $\approx \int_0^\infty \mathcal{F}(z^{1/\sigma})dz$, so we have

$$P_{\text{int}}(S) \approx A^{-\sigma} S^{-(\tau+\sigma)} \frac{1}{f^*} \int_0^\infty \mathcal{F}(z^{1/\sigma})dz \sim S^{-(\tau+\sigma)} \tag{C.23}$$

This give $P_{\text{int}}(S) \sim S^{-(\tau+\sigma)}$. When $(AS)^\sigma f^* \ll 1$, The $\exp(-z/((AS)^\sigma f^*))$ term decays out first and the integral is $\approx \int_0^\infty exp(-z/((AS)^\sigma f^*))dz$, so we have

$$P_{\text{int}}(S) \approx A^{-\sigma} S^{-(\tau+\sigma)} \frac{1}{f^*} \int_0^\infty \exp\left(-\frac{z}{(AS)^\sigma f^*}\right) dz = S^{-\tau}. \tag{C.24}$$

Therefore, we have a crossover scaling form:

$$P_{\text{int}}(S) \sim \begin{cases} S^{-\tau} & S \ll \frac{1}{(f^*)^{1/\sigma} A} \\ S^{-(\tau+\sigma)} & S \gg \frac{1}{(f^*)^{1/\sigma} A} \end{cases} \tag{C.25}$$

Therefore, as long as the distribution $P(f)$ has a width f^* large enough that the size of the largest avalanches measured $S_{\max} \gg \frac{1}{(f^*)^{1/\sigma} A}$, the tail of the distribution of avalanche sizes will scale with the stress-integrated distribution $P(S) \sim S^{-(\tau+\sigma)}$. The exponent derived by naive integration thus has a well-defined domain of validity.

For completeness, we derive the other stress-integrated exponents in Table 5.1:

$$P_{\text{int}}(T) \sim \int df T^{-\alpha} \mathcal{G}(f^{\nu z} T) = T^{-(\alpha + \frac{1}{\nu z})} \int dz z^{-\alpha} \mathcal{G}(z^{\nu z}) \sim T^{-(\alpha + \frac{1}{\nu z})} \tag{C.26}$$

$$P_{\text{int}}(v_m) \sim \int df v_m^{-\mu} \mathcal{H}(f^\rho v_m) = v_m^{-(\mu + \frac{1}{\rho})} \int dz z^{-\mu} \mathcal{H}(z^\rho) \sim v_m^{-(\mu + \frac{1}{\rho})} \tag{C.27}$$

$$P_{\text{int}}(E_m) \sim \int df E_m^{-(\mu+1)/2} \mathcal{H}(f^\rho E_m^{1/2}) = E_m^{-(\mu+1+\frac{1}{\rho})/2} \int dz z^{-(1+\mu)/2} \mathcal{H}(z^\rho) \sim E_m^{-(\mu+1+\frac{1}{\rho})/2} \tag{C.28}$$

C.4 Exponent relations for the maximum velocity

Our exact solutions seem to give evidence that the exponents μ and ρ describing the maximum velocity distribution (see Table 5.1) are not independent of the others. If the velocity remains a continuous function of time outside mean field theory, we expect that the maximum velocity scales like its average. Therefore, in terms of scaling dimensions, $v_m \sim \langle v \rangle \sim S/T$. In particular, we expect that the upper cutoff of the velocity distribution scales like

$$v_{mc} \sim \frac{S_c}{T_c} \sim \frac{k^{-1/\sigma}}{-k^{\nu z}} = k^{-(\frac{1}{\sigma} - \nu z)}. \tag{C.29}$$

The definition of ρ is that $v_{mc} \sim k^{-\rho}$, so we have

$$\rho = \frac{1}{\sigma} - \nu z = \frac{1 - \sigma \nu z}{\sigma}. \tag{C.30}$$

In MFT, we get $\rho = 1$, as expected.

Likewise, for the exponent μ, we can begin by writing down an ansatz for $P(v_m|S)$. In MFT, this took the scaling form of Eq. (5.31). This form could have been arrived at by dimensional analysis, knowing that the overall dimension of $P(v_m|S)$ was v_m^{-1}.[1] If we assume that this use of dimensional analysis continues to be valid for conditional distributions outside mean field theory, we expect a scaling form

$$P(v_m|S) \sim v_m^{-1} \mathcal{F}\left(\frac{v_m^{\frac{1}{\rho\sigma}}}{S}\right) \tag{C.31}$$

for the conditional distribution. Then we can compute $P(v_m)$ by integrating $P(v_m|S)$ over the avalanche sizes, which are distributed like $P(S) \sim S^{-\tau}$ at criticality. We get

$$P(v_m) \sim \int_0^\infty P(v_m|S)P(S)dS \sim \int_0^\infty v_m^{-1} \mathcal{F}\left(\frac{v_m^{\frac{1}{\rho\sigma}}}{S}\right) S^{-\tau} dS = v_m^{-\left(1 + \frac{\tau - 1}{\rho\sigma}\right)} \int_0^\infty z^{-\tau} \mathcal{F}\left(\frac{1}{z}\right) dz, \tag{C.32}$$

so we have $P(v_m) \sim v_m^{-\mu}$ where

$$\mu = 1 + \frac{\tau - 1}{\rho\sigma} = 1 + \frac{\tau - 1}{1 - \sigma\nu z}. \tag{C.33}$$

In MFT, this reduces to $\mu = -2$, as expected.

---

[1] However, note that this reasoning would fail for the *overall* velocity distribution $P(v_m)$, which has an anomalous dimension and thus its full expression requires a microscopic scale (See Eq. (5.40)).

Appendix D

Simulation results for dynamical weakening

In Section 2.1.1, we defined the dynamical weakening parameter of the model and mentioned a few of the qualitative differences that systems with weakening have from ones without. The principal difference is that while interevent times in systems without weakening are exponentially distributed (i.e. events arrive as a Poisson process) when there's weakening, large events are nearly periodic. There is also a marked delay between a large event and when the next small event comes. This nontrivial nucleation dynamics is of experimental interest.

In this chapter, we will give some model predictions from simulation for experimentally measurable quantities. All simulations were performed on a system with $N = 10000$ cells and a stress conservation parameter of $c = 0.999$.

In Fig. D.1, we show the size distributions at various values of the weakening parameter. We plot them as CCDFs, so the large vertical piece on the right-hand size of the distributions represent a cluster of large events (it would appear as a "bump" in the PDF). These are the quasi-periodic large events. Notice that as the weakening increases, the cluster of large events moves to a larger avalanche size and the regime of power law-distributed small events becomes smaller.

In Fig. D.2, we show the size versus duration scatter plot at two different values of the weakening. The small events have the scaling of $S \sim T^2$ in accordance with the analysis of Chapter 4. The large events scale like $S \sim T$, as is also predicted by the model and has been confirmed in BMG experiments [20, 40]. The difference between the distributions at higher and lower weakening is that at higher weakening (the right-hand plot), there is a noticeable gap, reflecting the fact that the small avalanches have a narrower distribution for higher weakening.

Finally, in Fig D.3, we show the interevent time following an avalanche versus the avalanche size. We see that for the large events, there is a much larger interevent time, and that the interevent time increases with the weakening. This is because the large events relax the system significantly, leading to a quiet period. When the weakening is higher, the large events get even bigger and cause even more relaxation.

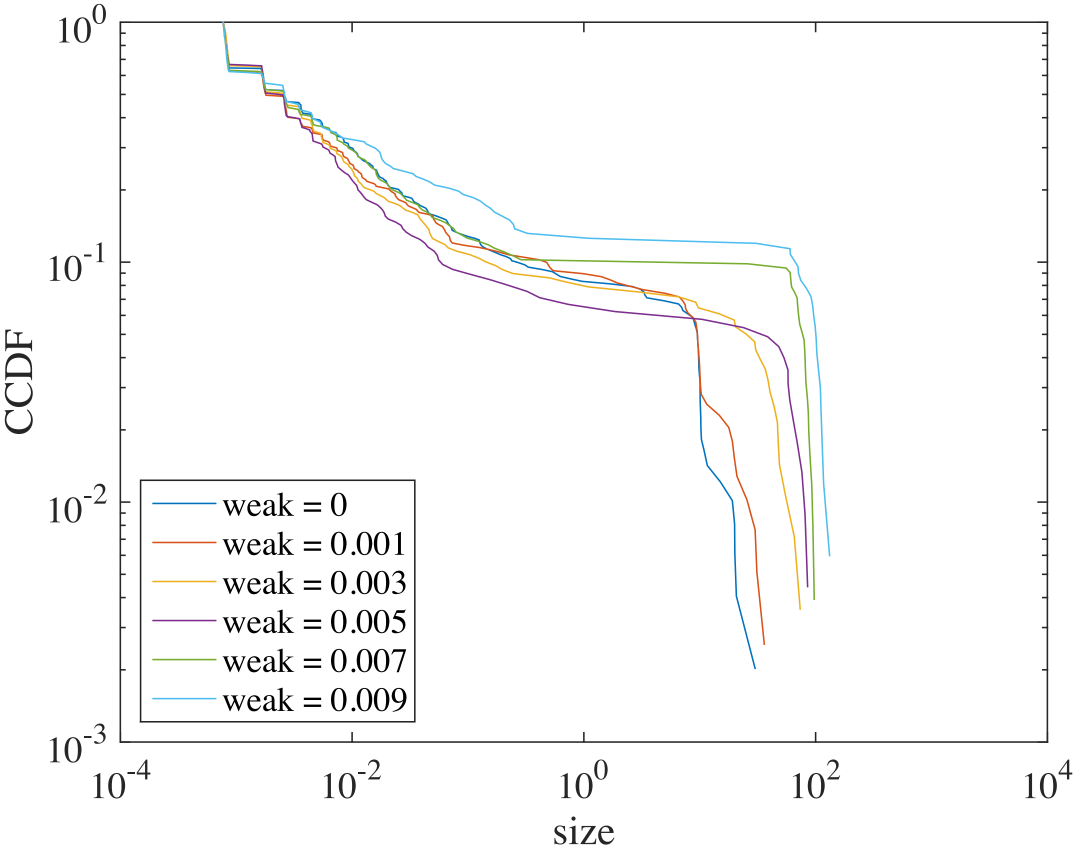

Figure D.1: CCDFs of avalanche sizes for various values of the weakening parameter ϵ.

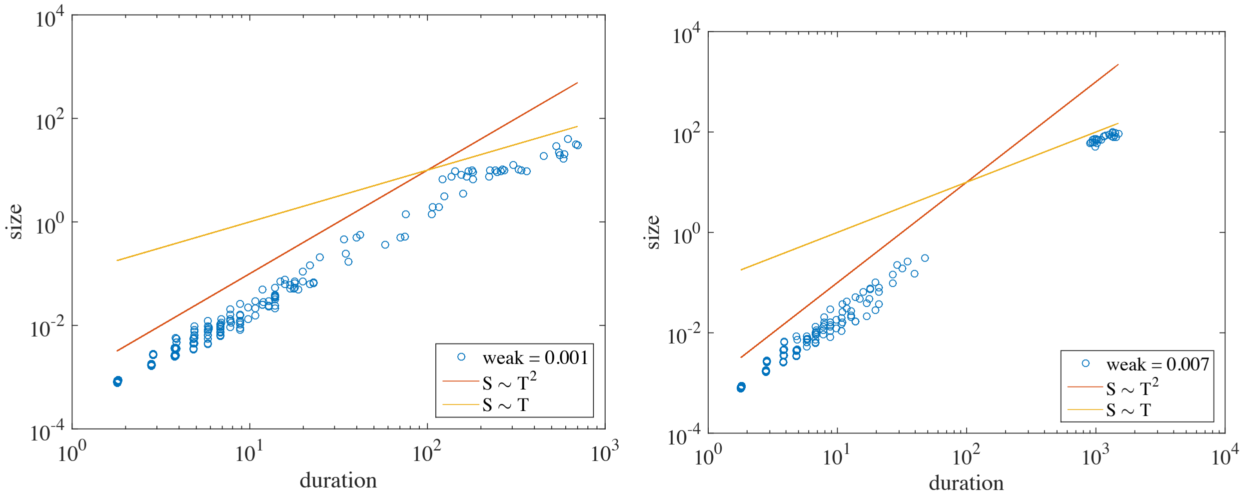

Figure D.2: Scatter plots of avalanche size versus duration for two different values of the weakening parameter ϵ. (left) $\epsilon = 0.001$ (right) $\epsilon = 0.007$.

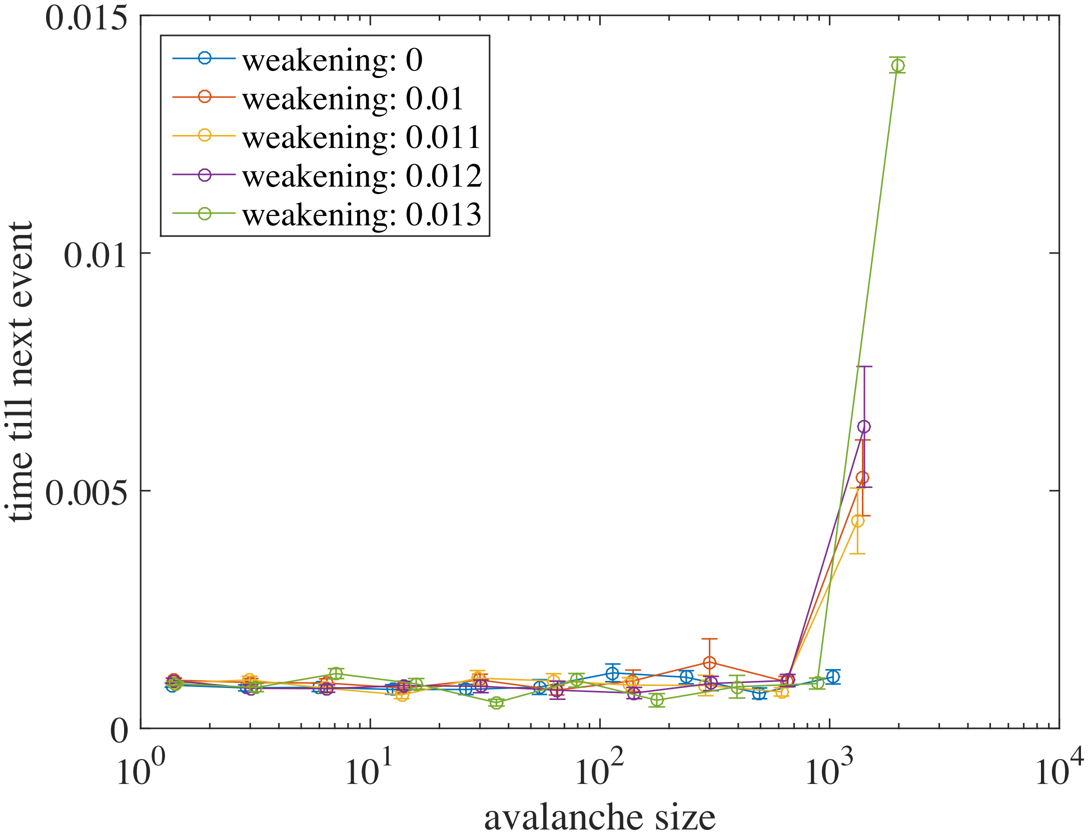

Figure D.3: Average interevent time after avalanche versus avalanche size. The quiet time following an avalanche increases for the large avalanches.

Appendix E

Finite driving effects in the ABBM model

E.1 ABBM avalanches at nonzero driving

Generally, studies of avalanches assume the slow-driving limit $v_d \to 0$. In this case, the ABBM model can be derived from the mean-field interface depinning model [74], so their predictions for avalanches are identical. The ABBM model can be solved at finite driving rate, but it's unknown whether its predictions should agree with interface depinning. We recall from Chapter 3 the ABBM equation of motion

$$\frac{dv}{dt} = k(v_d - v) + \sqrt{v}\xi(t) \tag{E.1}$$

where $\xi(t)$ is white noise with $\langle \xi(t)\xi(t')\rangle = A\delta(t-t')$.

One new issue at finite driving rate is the definition of an avalanche. At zero driving rate, an avalanche is defined as what happens during the interval of time between two zero-crossings of the velocity $v(t)$. The duration T of the avalanche is the length of the time interval, while the size is defined by the integral $S = \int v(t)dt$ over the interval. At finite driving rate, there is another option. Instead of using zero crossings, one can define an avalanches in terms of fluctuations of the velocity about its mean, which coincides the driving rate v_d. Then avalanches can be described the time intervals between mean-crossings, where the velocity is above v_d. The two definitions coincide when $v_d = 0$.

Using an avalanche definition in terms of fluctuation from the mean is motivated by the fact that the velocity v is the order parameter of the depinning transition. In the moving phase where $v > 0$, it is appropriate to consider fluctuations about $\langle v\rangle = v_d$ just as it is appropriate to consider fluctuations about the spontaneous magnetization when considering correlations in the magnetized phase of the Ising model. The definition in terms of fluctuations has another important advantage. At large driving rates, specifically when $c \equiv \frac{kv_d}{A} > 1/2$, the interface is constantly in motion and $v(t)$ does not have zero crossings at all. In this regime, only the second definition makes sense. The results about the avalanche distributions of the ABBM model that we derived in Chapter 4–for instance, that the exponents decrease linearly with c–are with respect to the first definition, and their breakdown when $c = 1/2$ is a reflection of the fact that avalanches become ill-defined there. By contrast, the second definition makes sense for any driving rate, although it disagrees with the first for $0 < c < 1/2$.

To study the fluctuations about the mean, we write Eq. (E.1) in terms of the relative fluctuations $w = (v - v_d)/v_d$. The resulting equation is

$$\frac{dw}{dt} = -kw + \sqrt{\frac{1+w}{v_d}}\xi(t). \tag{E.2}$$

Our avalanches will then be the times between zero-crossings of w. We will choose units where $k = 1$ and the noise constant $A = 1$, so that the equation is

$$\frac{dw}{dt} = -w + \sqrt{\frac{1+w}{c}}\xi(t) \tag{E.3}$$

with $\langle \xi(t)\xi(t') \rangle = \delta(t - t')$. Since w is the *relative* fluctuation, the avalanche sizes in w will be smaller by a factor of v_d than the fluctuations in $v - v_d$ that define our avalanches. For this reason, I will refer to the sizes of avalanches in w by S_w, reserving $S \equiv v_d S_w$ for "real" avalanche sizes.

E.1.1 Fast driving $c \gg 1$

For fast driving, the fluctuation term becomes very small compared to the mean-regression and $w \ll 1$ throughout. We can then use the approximation

$$\frac{dw}{dt} = -w + \sqrt{\frac{1}{c}}\xi(t), \tag{E.4}$$

which is an Ornstein-Uhlenbeck process with weak fluctuations. The avalanche durations will look like the duration distribution for Brownian excursions ($P(T) \sim 1/T^{3/2}$) with a cutoff due to the mean regression (See Eq. (2.16)). So we expect an asymptotic form like

$$P(T) \underset{T\to\infty}{\sim} \frac{e^{-AT}}{T^{3/2}} \tag{E.5}$$

where A is some dimensionless constant (this distribution has actually been calculated exactly and has $A = 1$).

The avalanche sizes are the areas under the excursions. Since from Eq. (E.4), the scale of the fluctuations is $1/\sqrt{c}$ and their characteristic return time is 1 due to the mean reversion, we expect an avalanche size

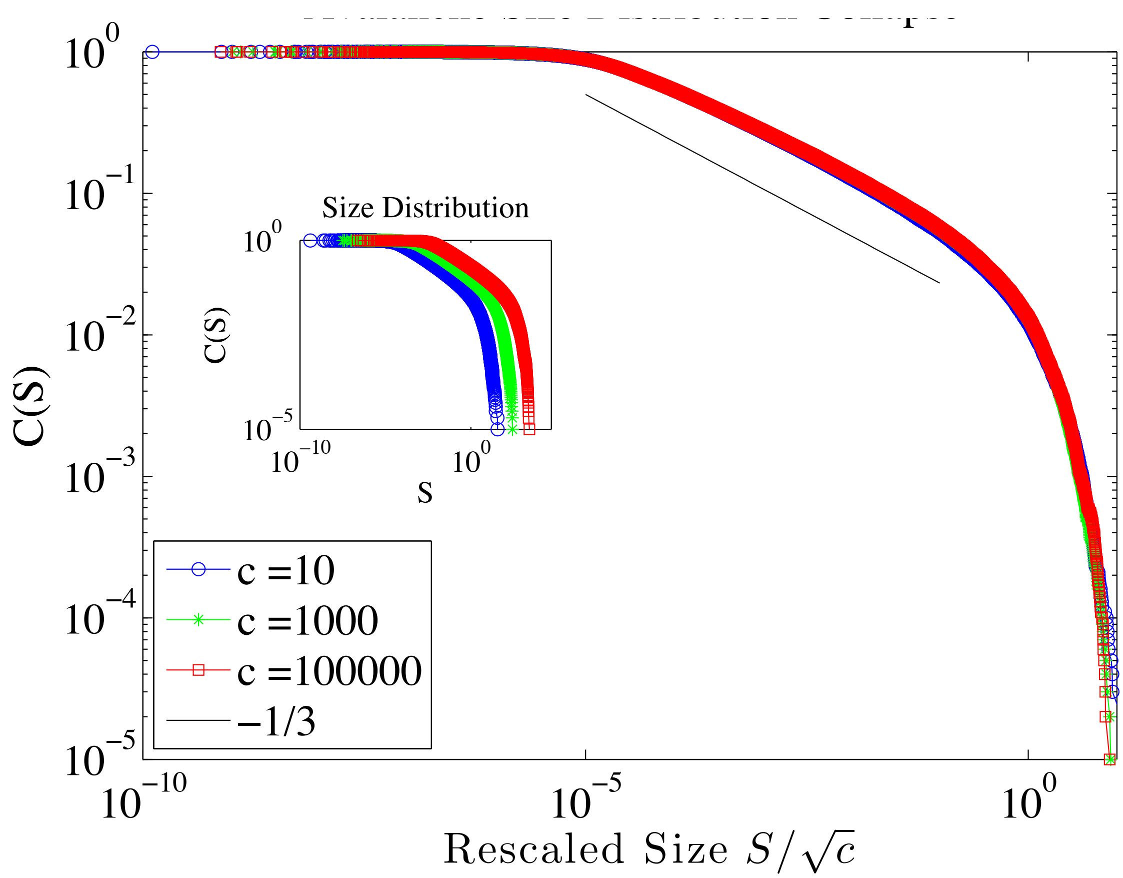

Figure E.1: Complementary cumulative distribution function $C(S)$ for the avalanche sizes, simulated from Eq. (E.3) for several large values of c. The size disributions with sizes rescaled by $1/\sqrt{c}$ all collapse onto the same scaling function. The guideline is the power law $-1/3$ predicted for $C(S)$ (The exponent of the CCDF is one less than that of the PDF.) The inset shows the size distributions before rescaling.

cutoff of $S_{wc} \sim 1/\sqrt{c}$. The distribution of avalanches much smaller than this will scale like the areas under Brownian excursions, which follow a power law of 4/3 [1]. Putting these together, we get

$$P(S_w) \underset{S_w \to \infty}{\sim} \frac{e^{-B\sqrt{c}S_w}}{(S_w)^{4/3}} \tag{E.6}$$

where B is some dimensionless constant. We computed this size distribution using the *relative* velocity $w \equiv (v - v_d)/v_d$. The real avalanche size, as measured by the area under the curve $v(t) - v_d$, is $S = v_d S_w$. Recalling that $v_d = c/k$ (and that we have set $k = 1$), the size distribution is

$$P(S) \sim \frac{e^{-\frac{BS}{\sqrt{c}}}}{S^{4/3}} \tag{E.7}$$

---

[1] The 4/3 power law can be understood as follows: The excursion's height scales like $\sqrt{T}$ since it's a diffusion, and thus the area should scale like $T^{3/2}$. We know the duration has PDF $P(T) \sim T^{-3/2}$. Changing variables to $A = T^{3/2}$ gives $P(A) \sim A^{-4/3}$.

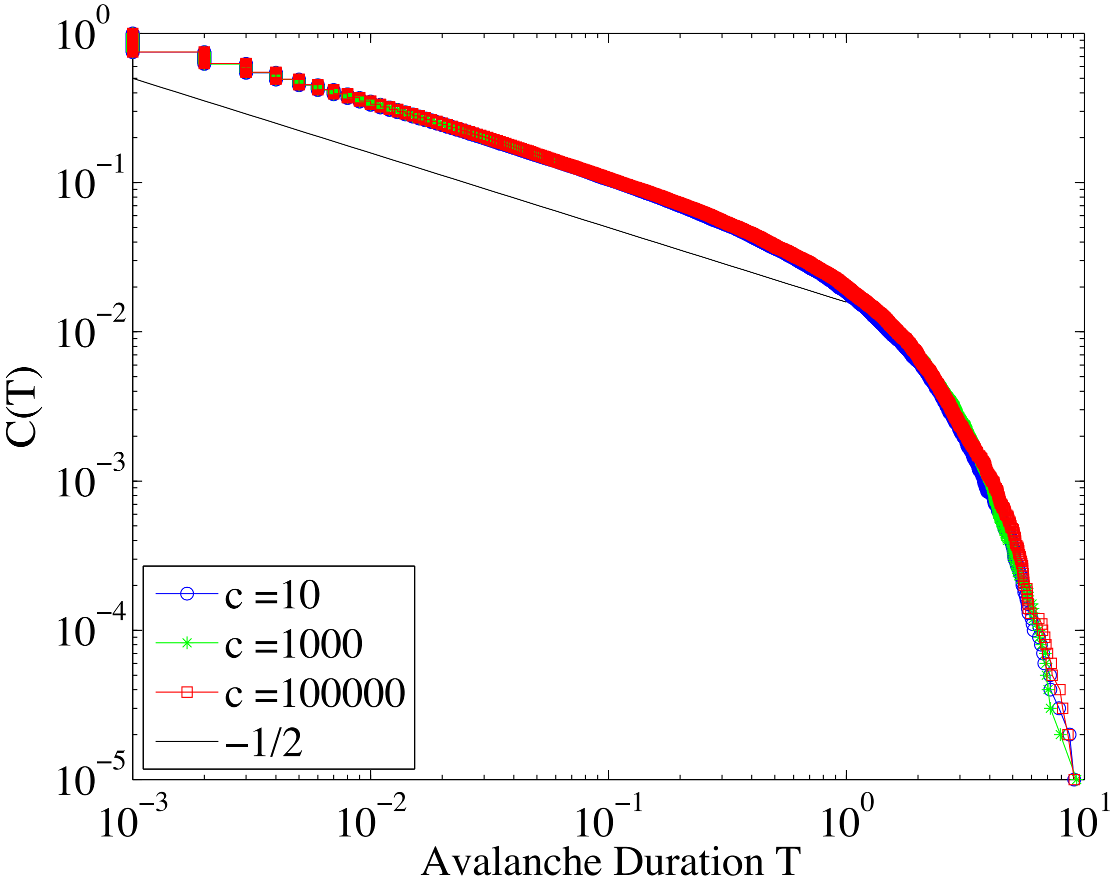

Figure E.2: Complementary cumulative distribution functions $C(T)$ for the avalanche durations, simulated from Eq. (E.3) for several large values of c. The conditions are the same as for Fig. E.1. The duration distributions are independent of c. The line is the predicted power law of $-1/2$. (The exponent of the CCDF is one less than that of the PDF.)

Therefore we expect that the avalanche size cutoff value $S_c = v_d S_{wc} \sim \sqrt{c}$. From Eq. (E.5), we see that the duration cutoff T_c is independent of c. The cutoff dependences and the values of the exponents are confirmed in Figs. E.1 and E.2.

E.1.2 Slow Driving $c \ll 1$

For sufficiently slow driving, we obviously expect the usual adiabatic predictions $P(S) \sim S^{-3/2}e^{-k^2 S/2A}$ and $P(T) \sim T^{-2}e^{-kT}$ to obtain. In the case where the avalanches are measured with respect to zero velocity, increasing the driving rate flattens the exponents and increases the cutoffs of the size and duration distributions. Eventually, as $c \to 1/2$, the cutoffs diverge. We know that the behavior must be different under our new avalanche definition, since the duration cutoff remains $T_c \sim 1/k$, even as the driving rate becomes very large. However, the exponents do eventually become smaller.

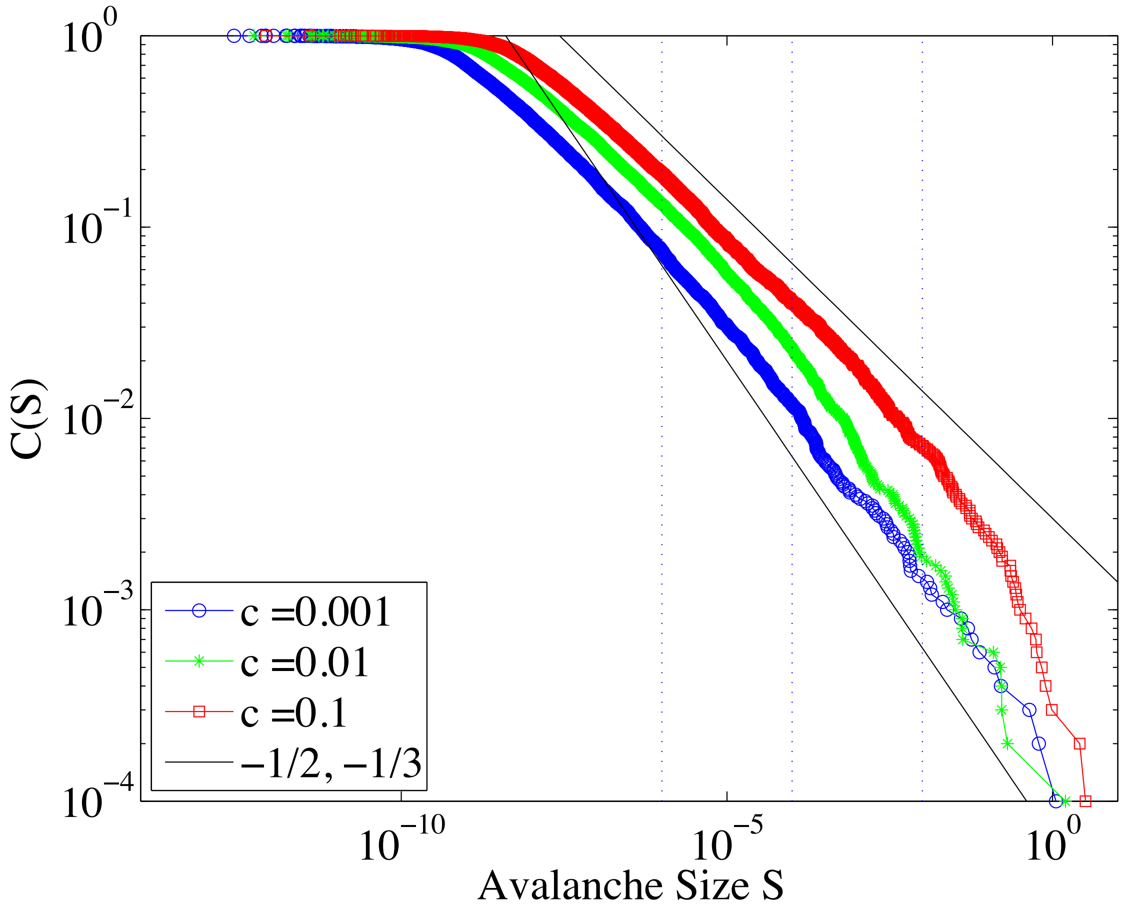

Figure E.3: Complementary cumulative distribution function $C(S)$ for the avalanche sizes, simulated from Eq. (E.3) for several small values of c. The size distributions along with lines with slope $-1/3$ and $-1/2$ from the random walk and MFT, respectively. (The exponent of the CCDF is one less than that of the PDF.) The vertical lines are drawn at $S = c^2$ for the three different c's to indicate the approximate crossover points. The right-most crossover on the red curve is indistinguishable from the cutoff. Note the cutoffs don't depend strongly on c. This feature persists when c is taken over a much larger range.

Transforming the the steady state equation Eq. (4.3), one can see that the size of the largest relative velocity fluctuations is $w_c \sim (1-c)/c$. When $c \ll 1$, the velocity will travel far from the mean ($w \gg 1$) during the large avalanches. While the avalanche is large, the equation of motion is approximately

$$\frac{dw}{dt} = -w + \sqrt{\frac{w}{c}}\xi(t). \tag{E.8}$$

This is just the ABBM equation (Eq. (E.1)) with no driving. Thus, the durations go like $P(T) \sim T^{-2}e^{-T}$. There is an effective noise constant of $1/c$, so (referring to the noise dependence of Eq.(4.52)) $P(S_w) \sim (S_w)^{-3/2}e^{-cS_w}$ and $S_{wc} \sim 1/c$. Since these are the avalanches in the relative velocity w, the size of avalanches in $v - v_d = wv_d$ have $S_c \sim 1$, independent of c.

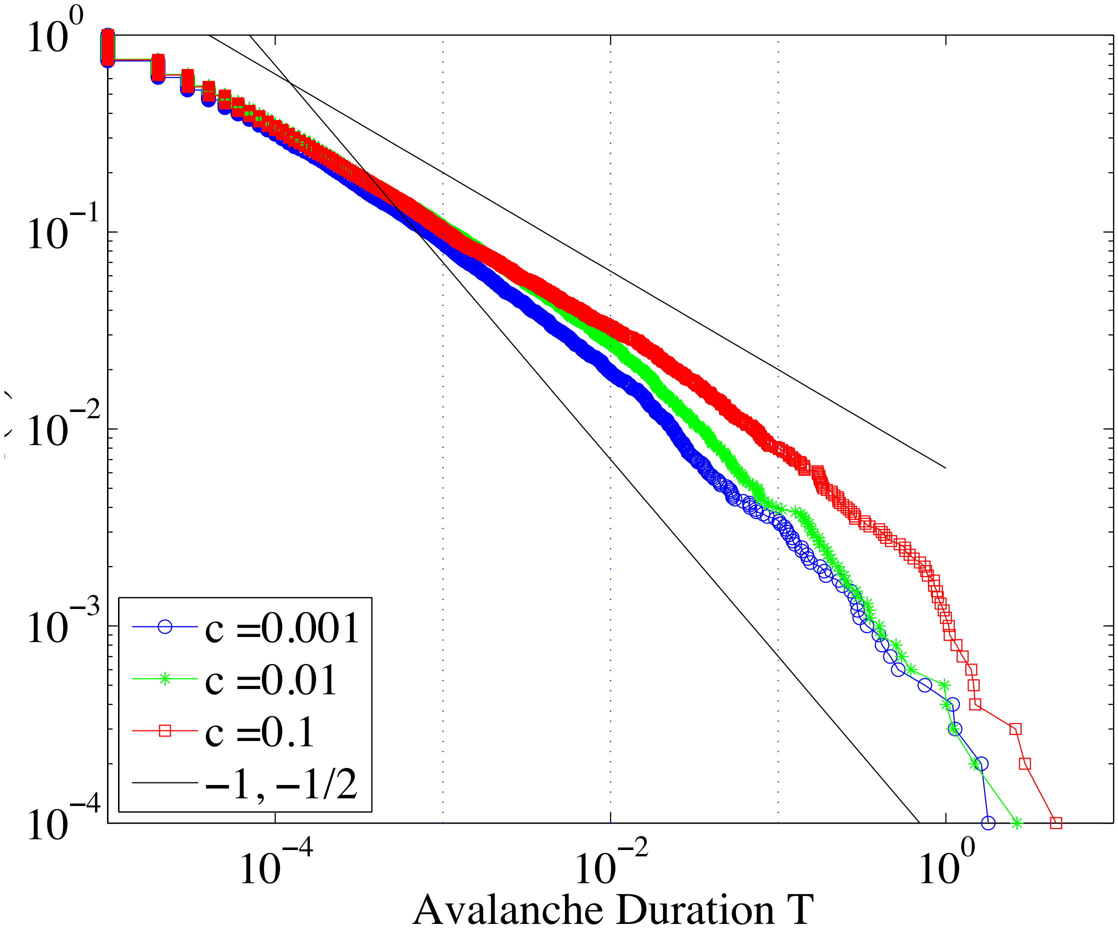

Figure E.4: Complementary cumulative distribution function $C(T)$ for the avalanche durations, simulated from Eq. (E.3) for several small values of c. The lines are power laws of $-1/2$ and -1 from the random walk and ABBM model, respectively. (The exponent of the CCDF is one less than that of the PDF.) The vertical lines are drawn at $T = c$ for the three different c's to indicate the approximate crossover points. Note the cutoffs don't depend strongly on c. This feature persists when c is taken over a much larger range.

Every avalanche spends some time with $w \leq 1$, so Eq. (E.8) is not ever a good approximation over the course of an entire avalanche. However, we expect it will govern the scaling of large avalanches since $w \gg 1$ will hold for most of the duration of the avalanche.

On the other hand, avalanches much smaller than this will have $w \ll 1$ and will be governed by Eq. (E.4) and the random walk scaling. This means that we will see a crossover between the two sets of power laws. However, the cutoff behavior will always be as dictated by Eq. (E.8) since it pertains to the largest avalanches (and we are assuming that the largest avalanches have $w \gg 1$.) Therefore the behavior for $c \ll 1$ is a crossover between two power-laws, with cutoffs in the size and duration that do not depend strongly on c.

To find the crossover point, we estimate that $\langle w \rangle = S_w/T > 1$ for the avalanche to be large enough that it has the ABBM dynamics. This means that the crossover happens when $T \approx S_w$. We know that in the scaling regime $S_w \sim \frac{T^{3/2}}{\sqrt{c}}$. Equating these two expressions, we get that $T_{\text{crossover}} \sim c$. Similarly, $S_{w,\text{crossover}} \sim c$, and after rescaling by v_d, $S_{\text{crossover}} \sim c^2$. We plot the distributions in Figs. E.3 and E.4.

E.2 Summary

Through a direct analysis of Eq. (E.1) at both very large and very small values of the parameter c, we have shown that, when the avalanche sizes are defined as the area under the curve $v(t) - v_d$ for excursions $v(t)$ goes above v_d and then drops below it:

1. For $c \gg 1$, the avalanche sizes increase with c, with maximum avalanche sizes scaling as $S_c \sim \sqrt{c}$. The power law exponent is $-4/3$, the same areas under random walks.

2. For $c \gg 1$ the duration distributions are roughly independent of c. They have a power law regime with exponent $-1/2$, the same as random walk return times.

3. For $c \ll 1$, the avalanche size distribution has a more complicated crossover form. For avalanches with size smaller than the crossover size $S_{\text{crossover}} \sim c^2$, the size distribution follows the ABBM scaling exponent $P(S) \sim S^{-3/2}$ and above the crossover size it follows the Brownian excursion area scaling $P(S) \sim S^{-4/3}$. The cutoff does not depend strongly on c for fixed k.

4. For $c \ll 1$, the avalanche duration distribution has a similar crossover form to the size distribution. For avalanches with duration smaller than $T_{\text{crossover}} \sim c$, the duration distribution follows the ABBM power law $P(T) \sim T^{-2}$ and avalanche larger than that follow a random walk power law of $P(T) \sim T^{-3/2}$. The cutoff of the duration distribution also does not depend strongly on c for fixed k.

E.3 Conclusion

To summarize, in the ABBM model, there's no clean scaling in terms of v_d (at fixed k), except for $c \gg 1$. At that point, the avalanche sizes scale as $S \sim v_d^{1/2}$, the duration distributions are fixed, and the exponents are random walk. Far below that regime, there is a crossover to the MFT exponents and the cutoffs of both distributions depend very weakly on v_d.

This behavior is very different from basic scaling theory prediction. One would expect that as the driving rate increases, we move further from the transition and the correlation length decreases. Since $v \sim |F - F_c|$, the correlation length $\xi \sim |F = F_c|^{-1}$, and $S_c \sim \xi^{-2}$ in mean field theory, we expect a scaling form like $P(S) \sim S^{-3/2} F(S v_d^2)$ in which the power law remains constant and S_c decreases with v_d.

Appendix F

Strong disorder and heavy-tailed walks

In the cellular model of Chapter 2, we assumed that the cells all have similar failure thresholds and arrest stresses, so that the amount of stress released and redistributed when a cell fails is roughly constant. In this appendix we will relax that assumption and consider the situation where for each cell, $\tau_f - \tau_a$ is drawn from a broad distribution.

We can immediately adapt the random walk argument that lead to Eq. 2.17. However, this time, both the stress gap to the next most unstable cell ΔX_n and the amount of stress redistributed by the failure of the next most unstable cell ΔY_n will be broadly distributed. Thus we might guess that we can consider the avalanche sizes to be first passage times to the origin of heavy-tailed walks Z_n.

In the case where the distribution of $\tau_f - \tau_a$ has finite variance, we expect the increments of Z_n to also be finite variance and thus by the Central Limit Theorem, the properties of the random walk will be the same as a Gaussian random walk on large scales and there will be essentially no change to the results of Chapter 2.

Therefore, the only unsolved case is when the distribution of $\tau_f - \tau_a$ has infinite variance. There is a remarkable theorem due to Sparre Anderson that says that, regardless of the distribution of step widths, any *driftless* random walk has the same first-passage time distribution: the one that scales like $f(t) \sim t^{-3/2}$ [104]. This means that exactly at criticality (i.e., no drift toward the origin) we have an exponent

$$P(S) \sim S^{-3/2} \tag{F.1}$$

like always.

However, when there is drift, the results are different from those of Chapter 2. In the Gaussian case, the effect of drift toward the origin is to make the first passage distribution develop an exponential cutoff and a characteristic scale for the largest possible first passage times. For avalanches, this corresponds to characteristic maximum avalanche size. However, for heavy tailed walks, this isn't the general behavior.

For instance, the first passage time for a walk with increments distributed according to a biased Cauchy distribution

$$P(\Delta Z) \sim \frac{1}{1+(\Delta Z-\mu)^2} \tag{F.2}$$

have been computed exactly [105]. The result is that, rather than forming an exponential cutoff, the *power law exponent* increases with μ. Thus, in the infinite variance case, we would generically expect a form like

$$P(S) \sim S^{-(3/2+f(k))} \tag{F.3}$$

where k is the parameter that tunes away from criticality and f is some increasing function.

These ideas have recently been applied to avalanches in crystalline systems with complex pinning mechanisms [106]. Heavy-tailed walks have also been used to model large fluctuations in local stress in a mean field theory of amorphous plasticity [37].

References

[1] J. P. Sethna, K. A. Dahmen, and C. R. Myers, "Crackling noise," *Nature*, vol. 410, no. 6825, pp. 242–250, 2001.

[2] S. Zapperi, P. Cizeau, G. Durin, and H. E. Stanley, "Dynamics of a ferromagnetic domain wall: Avalanches, depinning transition, and the Barkhausen effect," *Physical Review B*, vol. 58, no. 10, pp. 6353–6366, 1998.

[3] P. A. Lee and T. M. Rice, "Electric field depinning of charge density waves," *Physical Review B*, vol. 19, no. 8, p. 3970, 1979.

[4] S. Brazovskii and T. Nattermann, "Pinning and sliding of driven elastic systems: from domain walls to charge density waves," *Advances in Physics*, vol. 53, no. 2, pp. 177–252, 2004.

[5] S. Field, J. Witt, F. Nori, and X. Ling, "Superconducting vortex avalanches," *Physical Review Letters*, vol. 74, no. 7, pp. 1206–1209, 1995.

[6] S. Zapperi, P. Ray, H. E. Stanley, and A. Vespignani, "Avalanches in breakdown and fracture processes," *Physical Review E*, vol. 59, no. 5, p. 5049, 1999.

[7] D. S. Fisher, "Collective transport in random media: from superconductors to earthquakes," *Physics Reports*, vol. 301, no. 1-3, pp. 113–150, 1998.

[8] J. T. Uhl, S. Pathak, D. Schorlemmer, X. Liu, R. Swindeman, B. A. W. Brinkman, M. LeBlanc, G. Tsekenis, N. Friedman, R. Behringer, D. Denisov, P. Schall, X. Gu, W. J. Wright, T. Hufnagel, A. Jennings, J. R. Greer, P. K. Liaw, T. Becker, G. Dresen, and K. A. Dahmen, "Universal quake statistics: From compressed nanocrystals to earthquakes," *Sci. Rep.*, vol. 5, p. 16493, nov 2015.

[9] M. C. Miguel, A. Vespignani, S. Zapperi, J. Weiss, and J. R. Grasso, "Intermittent dislocation flow in viscoplastic deformation," *Nature*, vol. 410, no. 6829, pp. 667–671, 2001.

[10] D. Dimiduk, C. Woodward, R. LeSar, and M. D. Uchic, "Scale-free intermittent flow in crystal plasticity," *Science*, vol. 312, no. 5777, pp. 1188–1190, 2006.

[11] N. Friedman, A. T. Jennings, G. Tsekenis, J. Y. Kim, M. Tao, J. T. Uhl, J. R. Greer, and K. A. Dahmen, "Statistics of dislocation slip avalanches in nanosized single crystals show tuned critical behavior predicted by a simple mean field model," *Physical Review Letters*, vol. 109, no. 9, p. 095507, 2012.

[12] M. C. Miguel, A. Vespignani, M. Zaiser, and S. Zapperi, "Dislocation jamming and andrade creep," *Physical review letters*, vol. 89, no. 16, p. 165501, 2002.

[13] J. Antonaglia, X. Xie, G. Schwarz, M. Wraith, J. Qiao, Y. Zhang, P. K. Liaw, J. T. Uhl, and K. A. Dahmen, "Tuned critical avalanche scaling in bulk metallic glasses," *Sci. Rep.*, vol. 4, mar 2014.

[14] J. Antonaglia, W. J. Wright, X. Gu, R. R. Byer, T. C. Hufnagel, M. LeBlanc, J. T. Uhl, and K. A. Dahmen, "Bulk metallic glasses deform via slip avalanches," *Phys. Rev. Lett.*, vol. 112, apr 2014.

[15] P. Moretti, M. C. Miguel, M. Zaiser, and S. Zapperi, "Depinning transition of dislocation assemblies: Pileups and low-angle grain boundaries," *Physical Review B*, vol. 69, no. 21, p. 214103, 2004.

[16] M. C. Miguel, L. Laurson, and M. J. Alava, "Material yielding and irreversible deformation mediated by dislocation motion," *Eur. Phys. J. B.*, vol. 64, no. 3-4, pp. 443–450, 2008.

[17] P.Y.Chan, G. Tsekenis, J. Dantzig, K. A. Dahmen, and N. Goldenfeld, "Plasticity and dislocation dynamics in a phase field crystal model," *Physical Review Letters*, vol. 105, no. 1, p. 15502, 2010.

[18] G. Tsekenis, N. Goldenfeld, and K. A. Dahmen, "Dislocations jam at any density," *Physical Review Letters*, vol. 106, no. 10, p. 105501, 2011.

[19] P. Le Doussal and K. J. Wiese, "Driven particle in a random landscape: Disorder correlator, avalanche distribution, and extreme value statistics of records," *Physical Review E*, vol. 79, no. 5, p. 051105, 2009.

[20] K. A. Dahmen, Y. Ben-Zion, and J. T. Uhl, "Micromechanical model for deformation in solids with universal predictions for stress-strain curves and slip avalanches," *Physical Review Letters*, vol. 102, no. 17, p. 175501, 2009.

[21] F. F. Csikor, C. Motz, D. Weygand, M. Zaiser, and S. Zapperi, "Dislocation avalanches, strain bursts, and the problem of plastic forming at the micrometer scale," *Science*, vol. 318, no. 5848, p. 251, 2007.

[22] G. Tsekenis, *Plasticity as a Depinning Phase Transition.* PhD thesis, University of Illinois Urbana Champaign, 2012.

[23] G. Tsekenis, J. T. Uhl, N. Goldenfeld, and K. A. Dahmen, "Determination of the universality class of crystal plasticity," *EPL (Europhysics Letters)*, vol. 101, no. 3, p. 36003, 2013.

[24] M. Zaiser, "Scale invariance in plastic flow of crystalline solids," *Advances in physics*, vol. 55, no. 1-2, pp. 185–245, 2006.

[25] T. Richeton, J. Weiss, and F. Louchet, "Dislocation avalanches: Role of temperature, grain size and strain hardening," *Acta Materialia*, vol. 53, no. 16, pp. 4463–4471, 2005.

[26] J. Weiss, T. Richeton, F. Louchet, F. Chmelik, P. Dobron, D. Entemeyer, M. Lebyodkin, T. Lebedkina, C. Fressengeas, and R. J. McDonald, "Evidence for universal intermittent crystal plasticity from acoustic emission and high-resolution extensometry experiments," *Physical Review B*, vol. 76, no. 22, p. 224110, 2007.

[27] S. Papanikolaou, D. M. Dimiduk, W. Choi, J. P. Sethna, M. D. Uchic, C. F. Woodward, and S. Zapperi, "Quasi-periodic events in crystal plasticity and the self-organized avalanche oscillator," *Nature*, vol. 490, no. 7421, pp. 517–521, 2012.

[28] R. Carroll, C. Lee, C.-W. Tsai, J.-W. Yeh, J. Antonaglia, B. A. Brinkman, M. LeBlanc, X. Xie, S. Chen, P. K. Liaw, *et al.*, "Experiments and model for serration statistics in low-entropy, medium-entropy, and high-entropy alloys," *Scientific reports*, vol. 5, 2015.

[29] P. D. Ispánovity, L. Laurson, M. Zaiser, I. Groma, S. Zapperi, and M. J. Alava, "Avalanches in 2d dislocation systems: Plastic yielding is not depinning," *Physical review letters*, vol. 112, no. 23, p. 235501, 2014.

[30] A. Argon and L. T. Shi, "Development of visco-plastic deformation in metallic glasses," *Acta Metallurgica*, vol. 31, no. 4, pp. 499–507, 1983.

[31] M. Falk and J. Langer, "Dynamics of viscoplastic deformation in amorphous solids," *Physical Review E*, vol. 57, no. 6, p. 7192, 1998.

[32] M. Falk and J. S. Langer, "Deformation and Failure of Amorphous Solidlike Materials," *Annu. Rev. Condens. Matter Phys.*, vol. 2, pp. 353–373, 2011.

[33] M. Talamali, V. Petäjä, D. Vandembroucq, and S. Roux, "Strain localization and anisotropic correlations in a mesoscopic model of amorphous plasticity," *Comptes Rendus Mécanique*, vol. 340, no. 4, pp. 275–288, 2012.

[34] K. M. Salerno, C. E. Maloney, and M. O. Robbins, "Avalanches in strained amorphous solids: does inertia destroy critical behavior?," *Physical review letters*, vol. 109, no. 10, p. 105703, 2012.

[35] K. M. Salerno and M. O. Robbins, "Effect of inertia on sheared disordered solids: Critical scaling of avalanches in two and three dimensions," *Physical Review E*, vol. 88, no. 6, p. 062206, 2013.

[36] J. Lin, A. Saade, E. Lerner, A. Rosso, and M. Wyart, "On the density of shear transformations in amorphous solids," *EPL (Europhysics Letters)*, vol. 105, no. 2, p. 26003, 2014.

[37] J. Lin and M. Wyart, "Mean-field description of plastic flow in amorphous solids," *Physical Review X*, vol. 6, no. 1, p. 011005, 2016.

[38] J. Lin, E. Lerner, A. Rosso, and M. Wyart, "Scaling description of the yielding transition in soft amorphous solids at zero temperature," *Proceedings of the National Academy of Sciences*, vol. 111, no. 40, pp. 14382–14387, 2014.

[39] J. Lin, T. Gueudré, A. Rosso, and M. Wyart, "Criticality in the approach to failure in amorphous solids," *Physical review letters*, vol. 115, no. 16, p. 168001, 2015.

[40] W. J. Wright, Y. Liu, X. Gu, K. D. V. Ness, S. L. Robare, X. Liu, J. Antonaglia, M. LeBlanc, J. T. Uhl, T. C. Hufnagel, and K. A. Dahmen, "Experimental evidence for both progressive and simultaneous shear during quasistatic compression of a bulk metallic glass," *J. Appl. Phys.*, vol. 119, p. 084908, feb 2016.

[41] B. Gutenberg and C. F. Richter, "Magnitude and energy of earthquakes," *Annals of Geophysics*, vol. 9, no. 1, pp. 1–15, 1956.

[42] B. Gutenberg and C. F. Richter, "Earthquake magnitude, intensity, energy, and acceleration (second paper)," *Bulletin of the seismological society of America*, vol. 46, no. 2, pp. 105–145, 1956.

[43] D. S. Fisher, K. Dahmen, S. Ramanathan, and Y. Ben-Zion, "Statistics of earthquakes in simple models of heterogeneous faults," *Physical review letters*, vol. 78, no. 25, p. 4885, 1997.

[44] D. P. Schwartz and K. J. Coppersmith, "Fault behavior and characteristic earthquakes: Examples from the wasatch and san andreas fault zones," *Journal of Geophysical Research: Solid Earth*, vol. 89, no. B7, pp. 5681–5698, 1984.

[45] K. Dahmen, D. Ertaş, and Y. Ben-Zion, "Gutenberg-richter and characteristic earthquake behavior in simple mean-field models of heterogeneous faults," *Physical Review E*, vol. 58, no. 2, p. 1494, 1998.

[46] A. Mehta, K. A. Dahmen, and Y. Ben-Zion, "Universal pulse shape scaling function and exponents: Critical test for avalanche models applied to barkhausen noise," *Physical Review E*, vol. 73, no. 5, p. 056104, 2006.

[47] B. A. Brinkman, M. LeBlanc, Y. Ben-Zion, J. T. Uhl, and K. A. Dahmen, "Probing failure susceptibilities of earthquake faults using small-quake tidal correlations," *Nature communications*, vol. 6, 2015.

[48] B. A. Brinkman, M. P. LeBlanc, J. T. Uhl, Y. Ben-Zion, and K. A. Dahmen, "Probabilistic model of waiting times between large failures in sheared media," *Physical Review E*, vol. 93, no. 1, p. 013003, 2016.

[49] M. LeBlanc, L. Angheluta, K. A. Dahmen, and N. Goldenfeld, "Distribution of maximum velocities in avalanches near the depinning transition," *Physical Review Letters*, vol. 87, no. 2, p. 022126, 2012.

[50] M. LeBlanc, L. Angheluta, K. Dahmen, and N. Goldenfeld, "Universal fluctuations and extreme statistics of avalanches near the depinning transition," *Phys. Rev. E*, vol. 87, p. 022126, Feb 2013.

[51] J. Weiss and J. R. Grasso, "Acoustic emission in single crystals of ice," *The Journal of Physical Chemistry B*, vol. 101, no. 32, pp. 6113–6117, 1997.

[52] J. Weiss, F. Lahaie, and J. R. Grasso, "Statistical analysis of dislocation dynamics during viscoplastic deformation from acoustic emission," *Journal of Geophysical Research*, vol. 105, no. B1, pp. 433–442, 2000.

[53] C. Fressengeas, A. J. Beaudoin, D. Entemeyer, T. Lebedkina, M. Lebyodkin, and V. Taupin, "Dislocation transport and intermittency in the plasticity of crystalline solids," *Physical Review B*, vol. 79, no. 1, p. 014108, 2009.

[54] J.-O. Krisponeit, S. Pitikaris, K. E. Avila, S. Küchemann, A. Krüger, and K. Samwer, "Crossover from random three-dimensional avalanches to correlated nano shear bands in metallic glasses," *Nature communications*, vol. 5, 2014.

[55] Y. Ben-Zion and J. R. Rice, "Earthquake failure sequences along a cellular fault zone in a three-dimensional elastic solid containing asperity and nonasperity regions," *Journal of Geophysical Research: Solid Earth*, vol. 98, no. B8, pp. 14109–14131, 1993.

[56] Y. Ben-Zion and J. R. Rice, "Slip patterns and earthquake populations along different classes of faults in elastic solids," *Journal of Geophysical Research: Solid Earth*, vol. 100, no. B7, pp. 12959–12983, 1995.

[57] Y. Ben-Zion, "Stress, slip, and earthquakes in models of complex single-fault systems incorporating brittle and creep deformations," *Journal of Geophysical Research: Solid Earth*, vol. 101, no. B3, pp. 5677–5706, 1996.

[58] O. Narayan and D. S. Fisher, "Threshold critical dynamics of driven interfaces in random media," *Phys. Rev. B*, vol. 48, pp. 7030–7042, Sep 1993.

[59] M. Kardar, "Nonequilibrium dynamics of interfaces and lines," *Physics reports*, vol. 301, no. 1, pp. 85–112, 1998.

[60] D. Dhar and S. Majumdar, "Abelian sandpile model on the bethe lattice," *Journal of Physics A: Mathematical and General*, vol. 23, no. 19, p. 4333, 1990.

[61] S. Zapperi, K. B. Lauritsen, and H. E. Stanley, "Self-organized branching processes: mean-field theory for avalanches," *Physical review letters*, vol. 75, no. 22, p. 4071, 1995.

[62] P. Bak, C. Tang, and K. Wiesenfeld, "Self-organized criticality: An explanation of the 1/f noise," *Physical review letters*, vol. 59, no. 4, p. 381, 1987.

[63] P. Bak, C. Tang, and K. Wiesenfeld, "Self-organized criticality," *Physical review A*, vol. 38, no. 1, p. 364, 1988.

[64] J. A. Bonachela and M. A. Muñoz, "Self-organization without conservation: true or just apparent scale-invariance?," *Journal of Statistical Mechanics: Theory and Experiment*, vol. 2009, no. 09, p. P09009, 2009.

[65] M. Alava, "Scaling in self-organized criticality from interface depinning?," *Journal of Physics: Condensed Matter*, vol. 14, no. 9, p. 2353, 2002.

[66] P. Le Doussal and K. J. Wiese, "Exact mapping of the stochastic field theory for manna sandpiles to interfaces in random media," *Physical review letters*, vol. 114, no. 11, p. 110601, 2015.

[67] S. Ross, *A First Course in Probability.* Pearson Prentice Hall, 7 ed., 2006.

[68] I. Karatzas and S. E. Shreve, *Brownian Motion and Stochastic Calculus.* Springer-Verlag, New York, 2 ed., 1991. p. 197.

[69] J. P. Sethna, K. Dahmen, S. Kartha, J. A. Krumhansl, B. W. Roberts, and J. D. Shore, "Hysteresis and Hierarchies: dynamics of disorder-driven first-order phase transitions," *Physical Review Letters*, vol. 70, no. 21, pp. 3347–3350, 1993.

[70] S. Papanikolaou, F. Bohn, R. Sommer, G. Durin, S. Zapperi, and J. P. Sethna, "Universality beyond power laws and the average avalanche shape," *Nature Physics*, vol. 7, no. 4, pp. 316–320, 2011.

[71] B. Alessandro, C. Beatrice, G. Bertotti, and A. Montorsi, "Domain-wall dynamics and barkhausen effect in metallic ferromagnetic materials. i. theory," *Journal of Applied Physics*, vol. 68, no. 6, pp. 2901–2907, 1990.

[72] F. Colaiori, "Exactly solvable model of avalanches dynamics for barkhausen crackling noise," *Advances in Physics*, vol. 57, no. 4, pp. 287–359, 2008.

[73] A. A. Middleton, "Asymptotic uniqueness of the sliding state for charge-density waves," *Phys. Rev. Lett.*, vol. 68, pp. 670–673, Feb 1992.

[74] P. Le Doussal and K. J. Wiese, "Avalanche dynamics of elastic interfaces," *Physical Review E*, vol. 88, no. 2, p. 022106, 2013.

[75] J. C. Cox, J. E. Ingersoll, Jr., and S. A. Ross, "A theory of the term structure of interest rates," *Econometrica: Journal of the Econometric Society*, pp. 385–407, 1985.

[76] E. Moro, "Numerical schemes for continuum models of reaction-diffusion systems subject to internal noise," *Physical Review E*, vol. 70, no. 4, p. 045102, 2004.

[77] W. Feller, "Two singular diffusion problems," *Annals of Mathematics*, vol. 54, no. 1, pp. 173–182, 1951.

[78] J. Masoliver and J. Perelló, "First-passage and escape problems in the feller process," *Physical Review E*, vol. 86, no. 4, p. 041116, 2012.

[79] B. Kaulakys and M. Alaburda, "Modeling scaled processes and 1/fβ noise using nonlinear stochastic differential equations," *Journal of Statistical Mechanics: Theory and Experiment*, vol. 2009, p. P02051, 2009.

[80] N. G. V. Kampen, *Stochastic Processes in Physics and Chemistry.* Elsevier Science, 2 ed., 1992.

[81] K. Itô, "Stochastic integral," *Proc. Imp. Acad.*, vol. 20, no. 8, pp. 519–524, 1944.

[82] S. N. Majumdar and A. Comtet, "Airy distribution function: from the area under a brownian excursion to the maximal height of fluctuating interfaces," *Journal of Statistical Physics*, vol. 119, no. 3, pp. 777–826, 2005.

[83] M. Abramowitz and I. Stegun, eds., *Handbook of mathematical functions.* Dover, 1965.

[84] P. Le Doussal and K. J. Wiese, "Distribution of velocities in an avalanche," *EPL (Europhysics Letters)*, vol. 97, no. 4, p. 46004, 2012.

[85] A. Dobrinevski, P. Le Doussal, and K. J. Wiese, "Nonstationary dynamics of the alessandro-beatrice-bertotti-montorsi model," *Phys. Rev. E*, vol. 85, p. 031105, Mar 2012.

[86] A. Dobrinevski, P. Le Doussal, and K. J. Wiese, "Statistics of avalanches with relaxation and barkhausen noise: A solvable model," *Physical Review E*, vol. 88, no. 3, p. 032106, 2013.

[87] M. J. Lighthill, *An Introduction to Fourier Analysis and Generalised Functions.* Cambridge University Press, Cambridge, UK, 1958.

[88] G. Durin and S. Zapperi, "Scaling Exponents for Barkhausen Avalanches in Polycrystalline and Amorphous Ferromagnets," *Physical Review Letters*, vol. 84, no. 20, pp. 4705–4708, 2000.

[89] M. C. Kuntz and J. P. Sethna, "Noise in disordered systems: The power spectrum and dynamic exponents in avalanche models," *Physical Review B*, vol. 62, no. 17, p. 11699, 2000.

[90] R. A. Fisher and L. H. C. Tippett, "Limiting forms of the frequency distribution of the largest or smallest member of a sample," *Math. Proc. Camb. Phil. Soc.*, vol. 24, p. 180, apr 1928.

[91] S. M. Berman, "Limit theorems for the maximum term in stationary sequences," *The Annals of Mathematical Statistics*, pp. 502–516, 1964.

[92] J. Pickands, "Asymptotic properties of the maximum in a stationary gaussian process," *Transactions of the American Mathematical Society*, vol. 145, pp. 75–86, 1969.

[93] J. F. Eichner, J. W. Kantelhardt, A. Bunde, and S. Havlin, "Extreme value statistics in records with long-term persistence," *Physical Review E*, vol. 73, no. 1, p. 016130, 2006.

[94] T. Antal, M. Droz, G. Györgyi, and Z. Rácz, "1/f noise and extreme value statistics," *Physical Review Letters*, vol. 87, no. 24, p. 240601, 2001.

[95] G. Györgyi, N. R. Moloney, K. Ozogány, and Z. Rácz, "Maximal height statistics for 1/ f^{α} signals," *Physical Review E*, vol. 75, no. 2, p. 021123, 2007.

[96] S. N. Majumdar and A. Comtet, "Exact maximal height distribution of fluctuating interfaces," *Physical Review Letters*, vol. 92, no. 22, p. 225501, 2004.

[97] J. Rambeau, S. Bustingorry, A. B. Kolton, and G. Schehr, "Maximum relative height of elastic interfaces in random media," *Physical Review E*, vol. 84, no. 4, p. 041131, 2011.

[98] J. Rambeau and G. Schehr, "Maximum relative height of one-dimensional interfaces: from rayleigh to airy distribution," *Journal of Statistical Mechanics: Theory and Experiment*, vol. 2009, p. P09004, 2009.

[99] T. Burkhardt, G. Györgyi, N. R. Moloney, and Z. Rácz, "Extreme statistics for time series: Distribution of the maximum relative to the initial value," *Physical Review E*, vol. 76, no. 4, p. 041119, 2007.

[100] K. A. Dahmen and J. P. Sethna, "Hysteresis, avalanches, and disorder-induced critical scaling: A renormalization-group approach," *Physical Review B*, vol. 53, no. 2, p. 1487214905, 1996.

[101] B. Drossel and M. Kardar, "Scaling of energy barriers for flux lines and other random systems," *Physical Review E*, vol. 52, no. 5, p. 4841, 1995.

[102] P. Chauve, T. Giamarchi, and P. Le Doussal, "Creep via dynamical functional renormalization group," *EPL (Europhysics Letters)*, vol. 44, no. 1, p. 110, 1998.

[103] A. A. Middleton, "Thermal rounding of the charge-density-wave depinning transition," *Phys. Rev. B*, vol. 45, pp. 9465–9468, Apr 1992.

[104] E. S. Andersen, "On the fluctuations of sums of random variables ii," *Mathematica Scandinavica*, vol. 2, pp. 194–222, 1954.

[105] S. N. Majumdar, "Universal first-passage properties of discrete-time random walks and lévy flights on a line: statistics of the global maximum and records," *Physica A: Statistical Mechanics and its Applications*, vol. 389, no. 20, pp. 4299–4316, 2010.

[106] S. Pathak, M. LeBlanc, and K. A. Dahmen Unpublished.